UNIVERSIDADE FEDERAL DE SANTA CATARINA
CENTRO TECNOLÓGICO DE JOINVILLE
PROGRAMA DE PÓS-GRADUAÇÃO EM ENGENHARIA E CIÊNCIAS MECÂNICAS

Jéssica Florinda Zeitoune

Synthesis and characterization of a trimetallic Ni-Cu-Pt/Al_2O_3 catalytic monolith for hydrogen generation through autothermal ethanol reforming

Joinville
2024

Jéssica Florinda Zeitoune

Synthesis and characterization of a trimetallic Ni-Cu-Pt/Al_2O_3 catalytic monolith for hydrogen generation through autothermal ethanol reforming

Dissertação submetida ao Programa de Pós-Graduação em Engenharia e Ciências Mecânicas da Universidade Federal de Santa Catarina para a obtenção do título de Mestre em Engenharia e Ciências Mecânicas.
Orientador: Prof. Rafael de Camargo Catapan, Dr.
Co-orientadora: Profª. Camilla Daniela Moura Nickel, Dra.

Joinville
2024

Ficha de identificação da obra elaborada pelo autor,
através do Programa de Geração Automática da Biblioteca Universitária da UFSC.

Zeitoune, Jéssica Florinda
Synthesis and characterization of a trimetallic Ni-Cu Pt/Al2O3 catalytic monolith for hydrogen generation through autothermal ethanol reforming Joinville 2024 / Jéssica Florinda Zeitoune ; orientador, Rafael de Camargo Catapan, coorientadora, Camilla Daniela Moura Nickel, 2024.
97 p.

Dissertação (mestrado) - Universidade Federal de Santa Catarina, Campus Joinville, Programa de Pós-Graduação em Engenharia e Ciências Mecânicas, Joinville, 2024.

Inclui referências.

1. Engenharia e Ciências Mecânicas. 2. Reforma de etanol. 3. Hidrogênio. 4. Monólito catalítico. I. Catapan, Rafael de Camargo. II. Nickel, Camilla Daniela Moura. III. Universidade Federal de Santa Catarina. Programa de Pós Graduação em Engenharia e Ciências Mecânicas. IV. Título.

Jéssica Florinda Zeitoune

Synthesis and characterization of a trimetallic Ni-Cu-Pt/Al_2O_3 catalytic monolith for hydrogen generation through autothermal ethanol reforming

O presente trabalho em nível de mestrado foi avaliado e aprovado por banca examinadora composta pelos seguintes membros:

Prof. Gabriel Benedet Dutra, Dr.
Universidade Federal de Santa Catarina

Prof. Agenor de Noni Junior, Dr.
Universidade Federal de Santa Catarina

Prof. Dachamir Hotza, Dr.
Universidade Federal de Santa Catarina

Certificamos que esta é a **versão original e final** do trabalho de conclusão que foi julgado adequado para obtenção do título de Mestre em Engenharia e Ciências Mecânicas.

ICP-Edu
Documento assinado digitalmente
Wagner Mauricio Pachekoski
Data: 09/05/2024 21:29:01-0300
CPF: ***.494.569-**
Verifique as assinaturas em https://v.ufsc.br

Prof. Wagner Maurício Pachekoski, Dr.
Coordenador do Programa de
Pós-Graduação

ICP-Edu
Documento assinado digitalmente
Rafael de Camargo Catapan
Data: 09/05/2024 16:50:39-0300
CPF: ***.036.159-**
Verifique as assinaturas em https://v.ufsc.br

Prof. Rafael de Camargo Catapan, Dr.
Orientador

Joinville, 2024.

ACKNOWLEDGEMENTS

To Mateus, who was always helping me to overcome all the barriers of science.

To my family, who gave me all the support, and without them I would not have been able to enjoy this opportunity for a master's degree.

To my coordinator and supervisor Prof. Dr. Rafael de Camargo Catapan for all the moments when he believed in my potential and invested in me.

To my co-supervisor Profª. Dra. Camilla Nickel for being patient, always kind, and helpful to get me through this journey.

To my colleagues at LAC and the Rota 2030 project, for all the laughs, essential to make the days lighter and less stressful. I would like to give special recognition to Prof. Dr. Diego Alexandre Duarte and Vitor Lenz who helped me with some difficulties along the project.

To the new friends I made in Joinville, and also to my most lasting friendships, who were always willing to welcome and listen to me on difficult days.

To the Federal University of Santa Catarina (UFSC) and the Postgraduation Program in Engineering and Mechanical Sciences, for allowing me another opportunity for development and maturation.

The authors acknowledge the support of Rota2030/Linha V/FUNDEP, grant number 27192.01.01/2020.01-00. Also, I would like to thank the Multi-User Facility infrastructure of Santa Catarina State University's (UDESC) Technological Sciences Center, the Central Laboratory of Electron Microscopy (LCME) of UFSC, the Department of Physics, Plasma and Processes Laboratory (LPP) at the Aeronautics Institute of Technology (ITA) and the Laboratory of Applied Physics (LFA) at the Nuclear Technology Development Center (CDTN) of the Federal University of Minas Gerais (UFMG).

Finally, I thank everyone who was with me, who is part of my story, and who somehow contributed to the conclusion of one more engineering course.

Jéssica Florinda Zeitoune (Flor)

”Every path is the right path. Everything could’ve been anything else. And it would have just as much meaning.” (WILLIAMS, Tennessee)

ABSTRACT

The Earth's climate underwent substantial changes due to centuries of excessive Greenhouse Gas (GHG) emissions. The transport sector, a major contributor to these emissions, heavily relies on internal combustion engine vehicles. One approach to mitigate GHG emissions is transitioning to electric engines powered by H_2 derived from ethanol reforming, both considered renewable and environmentally friendly. Enhancing the process efficiency requires a catalyst with high conversion rates and selectivity for ethanol to H_2. This study aimed at manufacturing Ni/Al_2O_3 and $Ni\text{-}Cu\text{-}Pt/Al_2O_3$ catalytic monoliths for Autothermal Reforming (ATR) of ethanol. Characterization methods included X-Ray Diffraction (XRD), Scanning Electron Microscopy (SEM), Energy Dispersive Spectroscopy (EDS), X-Ray Photoelectron Spectroscopy (XPS) and Temperature Programmed Reduction (TPR). Catalytic behavior in ATR (400-700 °C) was assessed. The monoliths had an average washcoat content (C(%)) of 19.0%, nickel impregnation mass content (M_{Ni}(%)) of 9.62%, and copper impregnation mass content (M_{Cu}(%)) of 0.52%. Limited or no mass gain in platinum impregnation mass content (M_{Pt}(%)) was justified due to the corrosive nature of nitric acid. XRD indicated alumina and nickel in the nickel sample, while copper and platinum peaks in the trimetallic catalyst were relatively small. SEM images showed successful washcoat and impregnation processes without pore blocking. Unexpectedly, a *flower-like* structure in the trimetallic sample prompted further investigation. EDS confirmed alumina, nickel, and copper, with no platinum detected. XPS confirmed copper and platinum in the trimetallic monolith. TPR analyses highlighted homogeneity, with metal oxide reduction at different temperature ranges indicating distinctive peaks of nickel, copper, and platinum. Conversion and selectivity results showed higher ethanol conversion and H_2 production for the nickel catalyst at higher temperatures. The trimetallic catalyst effectively reduced the required temperature for initiating the ATR. In conclusion, this research contributes significantly in the use of mono and trimetallic catalysts for ATR, providing a foundation for future studies and applications. Unique findings open avenues for exploration, sustainability advancements, design optimization, and efficient ATR of ethanol processes.

Keywords: Ethanol. Reforming. Hydrogen. Catalyst. Monolith. $Ni\text{-}Cu\text{-}Pt/Al_2O_3$.

RESUMO EXPANDIDO

RESUMO

O clima da Terra passou por mudanças substanciais devido a séculos de emissões excessivas de Gases de Efeito Estufa (GHG). O setor de transporte, um grande contribuinte para essas emissões, depende fortemente de veículos com motores de combustão interna. Uma abordagem para mitigar as emissões de GHG é a transição para motores elétricos alimentados por H_2 derivado da reforma de etanol, ambos considerados fontes de energia renovável e ecologicamente corretas. Aprimorar a eficiência do processo requer um catalisador com altas taxas de conversão e seletividade para a transformação do etanol em H_2. Este estudo teve como objetivo a fabricação de monólitos catalíticos de Ni/Al_2O_3 e $Ni\text{-}Cu\text{-}Pt/Al_2O_3$ para Reforma Autotérmica (ATR) de etanol. Os métodos de caracterização incluíram Difração de Raios-X (XRD), Microscopia Eletrônica de Varredura (SEM), Espectroscopia de Energia Dispersiva (EDS), Espectroscopia de Fotoelétrons Excitados por Raios-X (XPS) e Redução à Temperatura Programada (TPR). O comportamento catalítico na ATR (400-700 °C) foi avaliado. Os monólitos apresentaram teor médio de revestimento (C(%)) de 19,0%, teor de níquel na impregnação ($M_{Ni}(\%)$) de 9,62%, e teor de cobre na impregnação ($M_{Cu}(\%)$) de 0,52%. A ausência ou ganho limitado de massa no teor de platina na impregnação ($M_{Pt}(\%)$) foi justificada devido à natureza corrosiva do ácido nítrico. XRD indicou alumina e níquel na amostra de níquel, enquanto os picos de cobre e platina no catalisador trimetálico eram relativamente pequenos. As imagens de SEM mostraram processos bem-sucedidos de revestimento e impregnação sem bloqueio de poros. Inesperadamente, uma estrutura *tipo-flor* na amostra trimetálica levou a investigações adicionais. EDS confirmou a presença de alumina, níquel e cobre, com platina não detectada. XPS confirmou cobre e platina no monólito trimetálico. Análises de TPR destacaram a homogeneidade, com redução de óxidos metálicos em diferentes faixas de temperatura, indicando picos distintos de níquel, cobre e platina. Resultados de conversão e seletividade mostraram maior conversão de etanol e produção de H_2 para o catalisador de níquel em temperaturas mais altas. O catalisador trimetálico reduziu efetivamente a temperatura necessária para iniciar a ATR. Em conclusão, esta pesquisa contribui significativamente na utilização de catalisadores mono e trimetálicos para ATR, estabelecendo uma base para estudos e aplicações futuras. Descobertas únicas abrem caminhos para exploração, avanços em sustentabilidade, otimização de design e processos eficientes de ATR de etanol.

Palavras-chave: Etanol. Reforma. Hidrogênio. Catalisador. Monólito. $Ni\text{-}Cu\text{-}Pt/Al_2O_3$.

INTRODUÇÃO

As emissões de CO_2 provenientes da queima de combustíveis tiveram início na Revolução Industrial, no final do século XVIII, na Europa. Este período testemunhou avanços tecnológicos significativos, resultando no rápido crescimento da indústria de manufatura. No Brasil, as emissões per capita de CO_2 aumentaram significativamente desde 1950, mas a conscientização ambiental sobre essas emissões só ganhou destaque recentemente. O ano de 1972 foi crucial, com a primeira Conferência das Nações Unidas sobre o Meio Ambiente em Estocolmo, resultando na criação do Programa Ambiental das Nações Unidas (UNEP).

Em 2020, o setor de transporte contribuiu com 7,2 bilhões de toneladas de emissões de gases de efeito estufa (GHG). Na tentativa de mitigar as emissões desses gases, a eletrificação de veículos, surge como uma oportunidade. Veículos elétricos, alimentados por SOFC, apresentam maior eficiência energética que os veículos movidos a combustão interna. O uso inovador de SOFC na reforma de etanol destaca-se pela eficiência de conversão de energia. Os catalisadores desempenham um papel crucial na eficácia da produção de H_2.

Este trabalho visou desenvolver um catalisador para a reforma de etanol em H_2, alinhado com a demanda crescente por alternativas sustentáveis e economizamente viáveis nos setores industrial e de transporte.

OBJETIVO

Este estudo teve como objetivo investigar e comparar a síntese de monólitos de Ni/Al_2O_3 e $Ni\text{-}Cu\text{-}Pt/Al_2O_3$ em escala comercial e empregar esses monólitos na reforma de etanol para produção de hidrogênio.

OBJETIVOS ESPECÍFICOS

- Adaptação da rota de síntese do monólito;
- Validação da rota de síntese do monólito;
- Caracterização física, química e estrutural morfologia do monólito catalítico;
- Determinação da conversão e seletividade do catalisador.

METODOLOGIA

A metodologia de produção do monólito foi adaptada de Palm (2018), Agrafiotis e Tsetsekou (2000) e Silva Júnior *et al.* (2023). As caracterizações realizadas foram: XRD, SEM, EDS, XPS e TPR. Testes catalíticos foram realizados para analisar a conversão e seletividade nas reações de reforma autotérmica do etanol.

PREPARAÇÃO DO CATALISADOR

Espumas comerciais compostas por α-Al_2O_3 (fornecidas por GoodFellow) com porosidade de 40 PPI, espessura de 12,7 mm e diâmetro de 80 mm serviram como substratos monolíticos. Primeiramente os monólitos foram secos e depois revestidos com uma pasta de alumina 40%, posteriormente o monólito foi seco e calcinado. Na etapa de impregnação para o monólito trimetálico, níquel, cobre e platina foram impregnados sequencialmente na espuma de alumina usando soluções aquosas de ($Ni(NO_3)_2{\cdot}6H_2O$), ($Cu(NO_3)_2{\cdot}3H_2O$) e ($H_2PtCl_6){\cdot}6H_2O$). Ácido nítrico foi usado como íon concorrente adicionado à solução de platina. Para o monólito de níquel, foi realizada somente a primeira etapa de impregnação utilizando a solução aquosa de ($Ni(NO_3)_2{\cdot}6H_2O$). Para mitigar problemas de capilaridade, os monólitos foram imersos na solução dentro de um dessecador a vácuo, seguido de secagem e calcinação.

CARACTERIZAÇÃO DO MONÓLITO

XRD foi utilizada para identificar fases cristalinas e estimar tamanhos de partículas. SEM foi aplicado para analisar a topografia da superfície, morfologia e irregularidades na amostra. Também foi empregado para observar a distribuição de partículas dentro das camadas de revestimento e impregnação. Além disso, o EDS, foi empregado para determinar a composição química das amostras. XPS foi utilizado para analisar os orbitais Ni2p, Cu2p e Pt4d. TPR foi realizado para determinar a temperatura de redução dos metais e comparar qualitativamente as concentrações de fase ativa e fases do promotor na parte externa e internas do monólito.

ENSAIOS CATALÍTICOS PARA REFORMA AUTOTÉRMICA DE ETANOL

As reações de Reforma Autotérmica (ATR) do etanol foram realizadas com razões molares água/etanol de 3:1 em uma bancada de testes com um cromatógrafo gasoso para analisar a composição dos gases reformados.

RESULTADOS E DISCUSSÃO

Os monólitos desenvolvidos neste estudo tiveram em média C(%) de 19,0%, M_{Ni}(%) de 9,62%, M_{Cu}(%) de 0,52%. Na impregnação da platina devido à natureza corrosiva do ácido nítrico, justificou-se o pouco ou nenhum ganho de massa.

No XRD, a alumina apresentou o pico mais intenso. Em amostras contendo níquel, estrutura cristalina cúbica do níquel foi evidente, exibindo picos em valores de 2θ de 37,1°, 43,1°, 62,6°, 75,1°, e 79,1°, sendo o pico mais intenso a 2θ de 43,1° com um dp de 36 nm. A estabilidade térmica e resistência mecânica do níquel cúbico aprimoram a durabilidade do catalisador, garantindo alto desempenho prolongado

em condições extremas (CARDENAS; SERBENA, 2021). Amostras Ni-Cu-Pt Int não apresentaram picos de cobre, enquanto na amostra Ext a Intensidade Relativa Máxima (RI) foi de 1,16% para Cu a 2θ de 43,1°. Os picos de platina nas amostras Int e Ext apresentaram uma RI máxima de 0,32% a 2θ de 28,0° e 0,84% a 2θ de 34,9°, respectivamente.

Imagens de SEM confirmaram a ausência de bloqueio dos poros do monolito após o revestimento e as sucessivas impregnações, as imagens também confirmaram a aplicação bem-sucedida do revestimento e dos processos de impregnação. Devido à necessidade de reduzir o diâmetro da amostra de 80 mm para a escala de análise de 5 mm, áreas previamente inacessíveis no momento do revestimento e da impregnação foram expostas, permitindo a identificação visual da espuma de alumina. A descoberta da estrutura em forma *tipo-flor* na amostra com platina representa um marco na compreensão das características do catalisador trimetálico, com implicações catalíticas ainda não exploradas. Estudos futuros são necessários para elucidar a síntese dessa estrutura e avaliar sua repetibilidade. A análise de EDS confirmou a presença predominante de alumina e a presença de niquel e de cobre, enquanto a platina não foi detectada, destacando a importância da mapeamento elemental para uma detecção mais abrangente.

XPS revelou uma considerável porcentagem de carbono (C1s), indicando a presença de compostos à base de carbono adsorvidos ou incorporados na superfície das amostras. XPS confirmou a incorporação bem-sucedida de Ni, Cu e Pt na superfície do catalisador, mesmo que essa presença possa não ter sido evidente em outras técnicas de caracterização destacando a importância de diferentes métodos analíticos para obter uma compreensão abrangente da composição e características dos materiais em investigação.

TPR indicou a homogeneidade das amostras na parte interna e externa. Pelas temperaturas de redução no resultado da análise foi identificado os picos de redução do óxido de niquel na amostra Ni/Al_2O_3, e a redução do óxido de níquel, cobre e platina na amostra $Ni\text{-}Cu\text{-}Pt/Al_2O_3$ apresentaram picos mais altos na faixa de 300-500 ℃, indicando a redução do óxido de níquel, mas também apontando para a redução de cobre. Além disso, a presença de platina foi indicada por um pico em torno de 250 ℃, alinhando-se com observações similares em catalisadores $Pt\text{-}Cu/Al_2O_3$.

Com base nos resultados de conversão e seletividade, foi possível aferir que, embora o catalisador trimetálico tenha apresentado uma melhor conversão de etanol a 400 ℃, ele ainda foi menos seletivo para o hidrogênio do que o catalisador de níquel. À medida que a temperatura aumentou além de 500 ℃, o catalisador de níquel consistentemente superou o catalisador trimetálico em termos de conversão de etanol e seletividade para o hidrogênio. Isso sugere que, em temperaturas elevadas, o catalisador de níquel se tornou mais eficaz na promoção da reação de reforma.

CONCLUSÃO

Nesta dissertação, a síntese e caracterização de um monólito de Ni/Al_2O_3 e $Ni\text{-}Cu\text{-}Pt/Al_2O_3$ com 80 mm de diâmetro foi conduzida para a reforma autotérmica de etanol em hidrogênio. O monólito passou por diversas caracterizações e testes de reações de reforma que forneceram uma base sólida para estudos futuros. Em conclusão, a exploração extensiva de catalisadores mono e trimetálicos para a reforma do etanol proporcionou insights sobre sua composição, morfologia e comportamento térmico. O teores de revestimento e de impregnação demonstram um processo bem-sucedido com distribuição uniforme e replicabilidade. Além disso, a incorporação bem-sucedida de Ni, Cu e Pt na matriz de Al_2O_3 foi evidenciada por uma mudança nas porcentagens elementares, destacando a introdução de átomos metálicos na superfície do catalisador. Por fim a descoberta da estrutura *tipo-flor* nos catalisadores trimetálicos é promissora e abre caminhos para otimizações no design do catalisador. Os testes de reforma demonstraram com sucesso a eficácia do catalisador trimetálico na redução da temperatura necessária para a reforma do etanol, entretanto, embora a conversão do etanol tenha ocorrido em baixas temperaturas, a seletividade ainda foi melhor no catalisador de níquel, embora não tenha convertido tanto. Os testes de reforma indicaram que o catalisador de níquel testado a uma temperatura de 700 °C alcançou uma conversão quase completa e quase 50% de seletividade ao hidrogênio. Para obter resultados mais precisos, mais testes de conversão com o monólito em cada temperatura devem ser realizados.

LIST OF FIGURES

LIST OF TABLES

LIST OF ABBREVIATIONS AND ACRONYMS

ASF	Atomic Sensitivity Factors
ATR	Autothermal Reforming
CCT	Center for Technological Sciences
CDTN	Nuclear Technology Development Center
DSC	Differential Scanning Calorimetry
EDS	Energy Dispersive Spectroscopy
FCEV	Fuel Cell Electric Vehicle
FE	Fermi energy
FID	Flame Ionization Detector
FWHM	full width at half maximum
GC	Gas Chromatograph
GHG	Greenhouse Gas
ICCT	International Council on Clean Transportation
IEA	International Energy Agency
ITA	Aeronautics Institute of Technology
LAC	Laboratory of Applyed Catalysis and Combustion
LCME	Central Laboratory of Electron Microscopy
LFA	Laboratory of Applied Physics
LPM	Liters Per Minute
LPP	Department of Physics, Plasma and Processes Laboratory
MCD	Multi Channeltron Detector
PA	Practical Grade
POX	Partial Oxidation
PPI	Pores Per Inch
PWM	Pulse Width Modulation
RI	Relative Intensity
SEM	Scanning Electron Microscopy
SOFC	Solid Oxide Fuel Cell
SR	Steam Reforming
TCD	Thermal Conductivity Detector
TGA	Thermogravimetric Analysis
TPO	Temperature Programmed Oxidation
TPR	Temperature Programmed Reduction
UDESC	State University of Santa Catarina
UFMG	Federal University of Minas Gerais
UFSC	Federal University of Santa Catarina
UHV	Ultra-High Vacuum

UNEP	United Nations Environment Programme
WGS	Water-gas Shift
WHSV	Weight Hour Space Velocity
XPS	X-Ray Photoelectron Spectroscopy
XRD	X-Ray Diffraction

LIST OF SYMBOLS

C(%)	Washcoat mass content
M_{Ni}(%)	Nickel impregnation mass content
M_{Cu}(%)	Copper impregnation mass content
M_{Pt}(%)	Platinum impregnation mass content
dp	particle diameter
ΔH	Enthalpy change
h	Thickness of the foam
D	Diameter of the foam
O_e	O_2 to C_2H_5OH molar ratio
T	Temperature
W_e	H_2O to C_2H_5OH molar ratio
t	Time
S(%)	Selectivity of the reformed gas
k	Scherrer constant
λ	wavelength
θ	diffraction angle
β	Full Width at Half Maximum
$\dot{m}_{total}$	Mass flow rate of the feed per unit of time
$\sum m_{i,cat}$	Sum of the weights of the catalysts used
X(%)	Calculated fuel conversion
F_{inlet}	Flow at fuel inlet
F_{outlet}	Flow at fuel outlet
P_{outlet}	Product outlet
RG_{outlet}	Reformed gases outlet
m_1	Uncoated dry mass
m_2	Alumina washcoated dry mass
m_3	Ni impregnated dry mass
m_4	Cu impregnated dry mass
m_5	Pt impregnated dry mass
$X_{C_2H_5OH}$	Conversion for C_2H_5OH
$S_{C_3H_6O}$	Selectivity for C_3H_6O
$S_{C_2H_4O}$	Selectivity for C_2H_4O
$S_{C_2H_4}$	Selectivity for C_2H_4
S_{CH_4}	Selectivity for CH_4
S_{CO_2}	Selectivity for CO_2
S_{CO}	Selectivity for CO
S_{H_2}	Selectivity for H_2

CONTENTS

1 INTRODUCTION

Carbon Dioxide (CO_2) emissions from the burning of fossil fuels for energy and cement production began in the late 18th century as can be seen in Figure 1. Not coincidentally, this was also the time when the industrial revolution began in Britain, characterized by significant technological advancements that led to the rapid growth of the manufacturing industry on a scale unlike any previous era. During that period, mechanized manufacturing became commonplace, replacing the human workforce and causing various social and environmental issues (OURWORLDINDATA.ORG, 2022; ENCYCLOPAEDIA BRITANNICA, 2021).

Figure 1 – CO_2 emissions per capita per year.

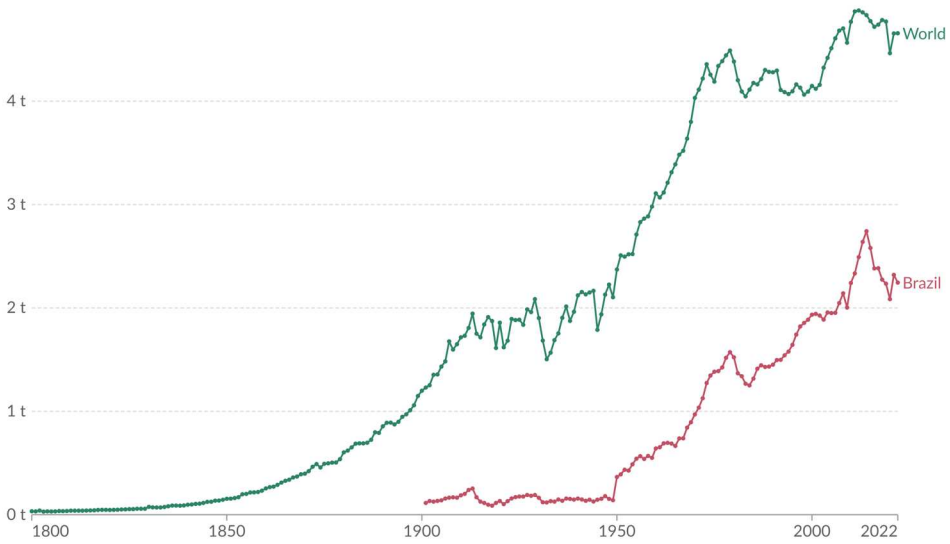

Source: ourworldindata.org (2022).

As seen in Figure 1, prior to 1950, Brazil's annual per capita emissions of CO_2 were very low, below 0.3 t, but by 1980, this value increased to 1.5 t. Over two centuries had passed since the Industrial Revolution, but environmental concerns only gained prominence recently. It began to be raised only in the late 1960s and early 1970s. Previously, some episodes showed the negative influence of uncontrolled growth on the population's life and the environment's health, often considered a necessary evil for progress (POTT; ESTRELA, 2017).

In 1972, a pivotal moment in global environmental initiatives unfolded as the United Nations Conference on the Environment took place in Stockholm. This landmark event attempted to organize a meaningful strategy for reshaping geopolitical conservation strategies. The participants at this conference reached a collective agreement on a series of resolutions, as articulated in the Stockholm Declaration and Action Plan for the Human Environment (VASSEUR, 1973; NATIONS, 2021). The event determined

26 relevant resolutions to place ”environmental issues at the forefront of international concerns”, serving as a decisive framework for nations committed to addressing environmental damage. These resolutions, were a turning point for tackling the issues of environmental damage and were directly responsible for the creation of the United Nations Environmental Programme (UNEP) (NATIONS, 2021).

Fast forward to 2020, the International Energy Agency (IEA) reported that the transport sector was responsible for a staggering 7.2 billion tons of GHG emissions worldwide (AGENCY, 2022). Addressing this environmental challenge, the electrification of cars emerges as a significant opportunity, particularly when powered by clean energy sources. This shift holds immense potential to substantially reduce greenhouse gas emissions associated with conventional fossil fuel-powered vehicles. In addition to environmental benefits, electric vehicles showcase superior efficiency in converting energy into motion, outperforming internal combustion engines and demanding less energy to cover equivalent distances.

Furthermore, the innovative use of Solid Oxide Fuel Cells (SOFC) presents a compelling option for powering electric vehicles. This electrochemical reactor, capable of converting chemical energy into electrical energy by directly oxidizing gaseous fuels like hydrogen gas, stands out for its high energy conversion efficiency (YAMAMOTO, 2000; SINGHAL; KENDALL, 2003).

According to the International Council on Clean Transportation (ICCT), Fuel Cell Electric Vehicle (FCEV) powered by hydrogen derived from renewable sources emit approximately 80% less GHG compared to combustion-powered vehicles (TRANSPORTATION, 2021). Since hydrogen gas is not naturally abundant, it must be obtained from natural gas, water through electrolysis, or ethanol, through a process known as reforming. There are three mains approaches to reform ethanol and obtain hydrogen: Partial Oxidation (POX); Steam Reforming (SR) and Autothermal Reforming (ATR) (BARUAH et al., 2015). In the POX process, ethanol is oxidized inside the reactor in the presence of a catalyst at elevated temperatures, resulting in the production of carbon monoxide and hydrogen. SR is a method in which the fuel reacts with water. Ethanol SR commonly occurs in the presence of catalysts, and is widely employed in industrial applications due to its ability to produce a substantial amount of H_2 at elevated temperatures (VITA et al., 2019; SOARES et al., 2017). ATR is a process that combines exothermic characteristics of POX and endothermic properties of SR, making it an almost thermodynamically neutral process (BARUAH et al., 2015).

In vehicle electrification, a method to convert ethanol and other reactants into a hydrogen-rich gas is through the gas generation unit, where the reforming process occurs. This unit plays a crucial role in ensuring the system operates with exceptional energy efficiency. The reformer (the central element of the unit) is a catalytic reactor formed by the catalytic monolith. The system converts the chemical energy in the

ethanol into electrical energy at the output of the SOFC. This electrical energy can then be used to drive the electric motor and stored in the battery for future use.

Catalysts play a crucial role in reducing the activation energy and enhancing the speed, energy and the conversion of ethanol and other reagents, such as water and oxygen, into a gas rich in hydrogen (SCIENCE, 2022). According to Chiu, Horng, and Chou (2013), the hierarchy of effectiveness in hydrogen production was as follows: Rhodium (Rh) > Ruthenium (Ru) > Palladium (Pd) > Platinum (Pt) > Nickel (Ni) > Cobalt (Co) > Iron (Fe). Noble metals tend to have higher costs but often exhibit better selectivity for hydrogen formation in reforming processes when compared to non-noble ones. Each metal possesses its own affinity, and specific characteristics that must be evaluated to obtain the desired results in the reaction (CHIU; HORNG; CHOU, 2013). On a large scale, nickel-based catalysts are among the most widely used due to to their cost-effectiveness. When coated with α-Al_2O_3 these catalysts exhibit an increased specific surface area, leading to higher metal dispersion (RODRIGUES; SCHMAL, 2011; MOHALLEM; VIANA; SILVA, 2011).

According to Palm (2018), nickel-based monoliths not only offer an economically viable alternative but also possess a catalytically active surface. Nickel reduces the binding energy of electrons in the valence band, by making the electrons participate more in the catalysis process. Nevertheless, one challenge associated with nickel-based monoliths is their tendency to form coke deposits, which can be mitigated by introducing a promoter: a substance or element that enhances the catalytic activity of a catalyst, into the composition (OGO; SEKINE, 2020). Additionally, capillarity poses another concern. Insufficient capillarity can result in the entrapment of impurities within the foam's pores, restraining the fluid's passage through these pores and potentially causing uneven impregnation of the monolith. To mitigate this issue, during the impregnation step, the catalysts will be placed inside a vacuum desiccator (LEKHAL; GLASSER; KHINAST, 2001).

In the investigation of bimetallic catalysts, the Ni-Rh combination was noted for its effectiveness in breaking C-C bonds but demonstrated limited activity in the Water-gas Shift (WGS) reaction. The Ni-Ru combination emerged as an economically viable alternative. However, its active role in ethanol dehydration led to the production of ethylene, identified as the primary source of coke formation (RASKÓ; HANCZ; ERDŐHELYI, 2004; GATES; RUSSELL; YATES, 1986).

On the other hand, copper has been established as the most efficient promoter for the production of hydrogen. It is the most commonly used promoter with nickel-based catalysts to overcome the inactivity of nickel in the WGS reaction, facilitating the production of hydrogen given that it promotes ethanol dehydrogenation while simultaneously preventing the unwanted growth of nickel particles. Insofar, nickel facilitates C-C bond scission and increases hydrogen selectivity. This multifaceted reactivity of

copper, coupled with the complementary actions of nickel, holds a significant impact on the development of a highly effective catalyst (BSHISH et al., 2011; YOUN et al., 2006).

Mozer (2005) suggests the incorporation of transition metals, such as Cu, into the Pt/Al2O3 catalyst. Cu demonstrated satisfactory results in the selective oxidation of CO. Therefore, the incorporation of the transition metal Cu into the Pt/Al2O3 catalyst is anticipated to further enhance reaction selectivity. Platinum, despite exhibiting intermediate activity in C-C bond breaking and WGS reaction, can be enhanced when combined with another catalyst. Additionally, platinum possesses the ability to suppress undesired reactions that could otherwise inhibit catalytic activity (DAVDA et al., 2004). Therefore, harnessing platinum as a promoter in synergy with another efficient metal can significantly contribute to the development of cleaner and more effective ethanol reforming and hydrogen production processes.

Rh and Pt bimetallic catalysts underwent testing in the ATR of ethanol. Pt-Rh combination was noted for their synergistic interaction and exhibited complete ethanol conversion, showcasing a remarkable selectivity for H_2 production while minimizing the generation of undesirable side products. Moreover, the potential for cost reduction was explored, revealing that substituting a portion of Rh with the more economical Pt did not significantly compromise the catalyst's properties, suggesting a feasible strategy for optimizing catalyst composition (GUTIERREZ et al., 2011).

1.1 MOTIVATION

Addressing the need for cleaner and more efficient hydrogen production processes, particularly for vehicle electrification, the focus is on developing a trimetallic catalyst that utilizes a combination of nickel, copper, and platinum to enhance the catalytic properties and lower activation temperature. Nickel is chosen for its efficiency in breaking C-C bonds and its low market cost. Copper enhances the catalytic activity of nickel in the WGS reaction, promotes ethanol dehydrogenation, and prevents the formation of carbon deposits. On the other hand, platinum, while not as effective as other metals in breaking C-C bonds, possesses properties that can suppress unwanted reactions and improve the catalyst selectivity for hydrogen production.

The combination of these metals can result in a more efficient catalyst capable of achieving high ethanol conversion rates and selectivity for hydrogen production, representing a significant advancement in the quest for cleaner and more efficient hydrogen production processes for vehicle electrification. This innovative approach aligns with the growing demand for eco-friendly alternatives and contributes to ongoing efforts to reduce the environmental impact of the industrial and transportation sectors.

1.2 MAIN OBJECTIVE

The main objective was to synthesize and investigate the use of commercial scale monoliths of Ni/Al_2O_3 and trimetallic $Ni\text{-}Cu\text{-}Pt/Al_2O_3$ in the ethanol reforming for hydrogen production.

1.2.1 Specific objectives

- Adaptation, development and validation of monolith synthesis route for the trimetallic catalytic monoliths;

An investigation of the manufacturing process, including washcoating and impregnation techniques, was conducted to enhance the synthesis route for catalytic monoliths. Through experimentation and parameter adjustments, enhancements were identified and implemented to optimize the efficiency, yield, and performance of the monolith synthesis process.

- Characterization of physical, chemical, and structural morphology of the trimetallic catalytic monoliths;

Characterization techniques such as X-Ray Diffraction (XRD), Scanning Electron Microscopy (SEM), Energy Dispersive Spectroscopy (EDS), X-Ray Photoelectron Spectroscopy (XPS) and Temperature Programmed Reduction (TPR) were utilized to provide a comprehensive assessment of the monolith's crystalline structure, surface topography, morphology, chemical composition and reduction temperature.

- Determination of the conversion and selectivity of the trimetallic catalytic monoliths;

The objective was to assess the catalytic performance of the synthesized monoliths. This involved conducting catalytic tests to determine their conversion efficiency and selectivity to hydrogen. The results provided critical insights into the catalytic capabilities of the monolithic catalyst.

- Validate existing synthesis routes for production of commercial scale monoliths.

Using established monolith manufacturing methodologies, a scale-up process was developed and validated for monolith synthesis, aiming to optimize production and ensure the quality of monoliths on a commercial scale.

2 LITERATURE REVIEW

This topic covered the catalyst production process, encompassing details on its composition, preparation methods, and the sequence of process steps involved. Furthermore, it reported some of the reforming reactions where catalysts played a pivotal role. Additionally, the discussion highlighted key research and work developments within this field.

2.1 SYNTHESIS ROUTE

A catalyst is a substance that plays a crucial role in facilitating chemical reactions by lowering the activation energy and increasing their rate. Furthermore, catalysts possess certain characteristics, including high chemical activity, selectivity, mechanical and thermal stability, and resistance to deactivation. Moreover, the monolithic structure also offers several advantages, such as a high specific surface area, scalability, and a requirement for economic viability during the entire production process (TOMAŠIC; JOVIC, 2006). The synthesis route section elucidates the composition of a catalyst, the materials necessary for its synthesis, some preparation methods, and the key steps involved in transforming the monolith into the final catalyst.

2.1.1 Monolith

The term ”monolith” originates from the Greek word *monólithos* and is formed by combining the roots -mono and -lith which means ”single” and ”stone” respectively. Catalytic monoliths can have various structures, with the most common and widely used being the honeycomb structure (Figure 2) due to its characteristic holes that provide a large surface area per volume and its mechanical stability, and the foam structure that offers high porosity and a large surface area, along with good mechanical strength. Foam monoliths are often used in vehicle emission control systems and industrial processes that require high catalytic efficiency and mechanical resistance (TOMAŠIC; JOVIC, 2006; MANFE; KULKARNI, K.; KULKARNI, A., 2011).

The catalytic monolith may also be referred to as monolithic reactors when filled with monoliths that are either made of porous catalytic material, either washcoated with a catalytic material, or both. In both configurations, the monolith structure acts as a catalyst and provides space for gas or liquid to flow. Currently, in the industry and research, ceramic and metal are the most commonly used materials for monolith supports (MANFE; KULKARNI, K.; KULKARNI, A., 2011).

Figure 2 – Representative scheme of a honeycomb structure.

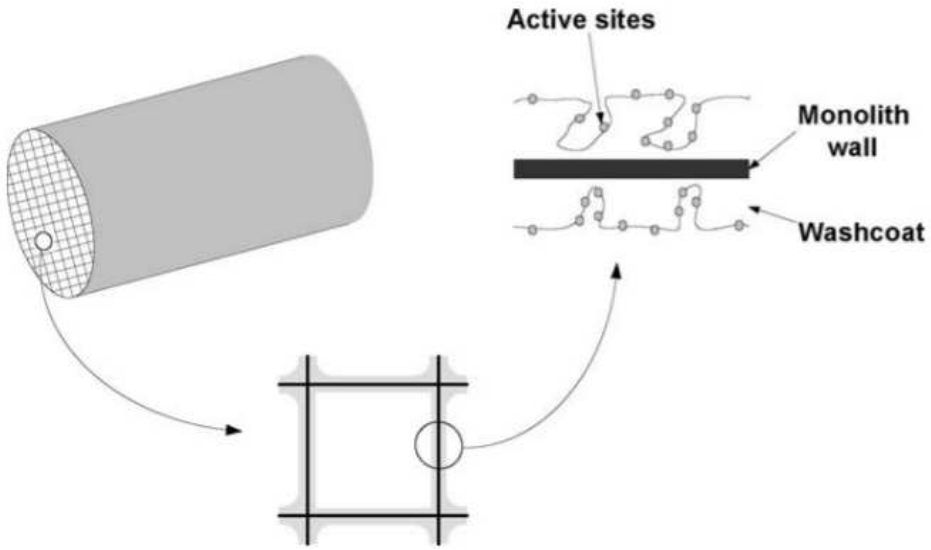

Source: Tomašic and Jovic (2006).

2.1.2 Support

Catalyst supports play a pivotal role in the development and optimization of catalytic processes, including ethanol reforming. The choice of the appropriate support material holds significant importance as it constitutes a major component of the catalyst itself (ZANCHET et al., 2015). It is imperative that the catalyst support material exhibits stability under the specific process conditions. As indicated by Zanchet et al. (2015), Sakata et al. (2006) and Aasberg-Petersen et al. (2004), the choice of support material wields a substantial influence on catalyst selectivity, stability, resistance to coke accumulation, and also impacts the stability of metal particles, preventing undesired sintering. Additionally, the support material should possess the capability to effectively disperse metal particles across its surface, facilitating catalytic activity.

Catalyst supports can be broadly categorized into several types, each with its unique characteristics and advantages. These supports encompass natural materials like charcoal or activated carbon, which offer attributes such as high surface area and cost-effectiveness. However, they may be susceptible to oxidation under certain reaction conditions, as noted by Palm (2018) and Araujo (2006). On the other hand, synthetic supports like alumina (Al_2O_3) and silica (SiO_2) are widely employed. Silica, a synthetic catalyst support, is typically used in the amorphous form, offering considerable advantages due to its controllable pore size, specific volume, and specific surface area. This tunability made it a valuable choice in various catalytic applications. (ERTL; KNÖZINGER; WEITKAMP, 2008).

Alumina, a ceramic material, was a widely used catalyst support and also very active catalysts (ERTL; KNÖZINGER; WEITKAMP, 2008; OGO; SEKINE, 2020). Its

popularity in the industry was attributed to its high surface area and stability, particularly in the context of nickel-based catalysts, as emphasized by Ogo and Sekine (2020). Furthermore, KHEMNARONG (2021) proposed that Al_2O_3 support served to stabilize NiO particles during the reaction, contributing to its effectiveness in catalytic processes.

Over the past two decades, there has been a growing interest in metallic supports, particularly stainless steel, for use in catalytic processes. The malleability and adaptability of stainless steel made it a versatile choice, allowing it to be tailored for various processes and geometrical forms (WANG et al., 2022).

However, it's important to note that metals have distinct characteristics compared to ceramics. They typically possessed a lower specific surface area, inert chemical surfaces, and exhibited significant differences in thermal expansivity compared to oxide coatings or active phase films. These differences could result in challenges related to poor adhesion, dispersion, and incorporation of subsequent synthesis steps. Consequently, metal supports often required pre-treatment to improve these properties before applying coating and impregnation layers (WANG et al., 2022; BANÚS et al., 2010).

Indeed, the choice of a suitable support material is a critical factor in the development of effective catalysts for ethanol reforming. Different support materials offer distinct properties that can significantly influence the performance of the catalyst. Researchers have explored various support types, including ceramics, like alumina, silica, carbon-based materials, and metal-based materials each with its set of advantages and characteristics.

2.1.2.1 Alumina

Alumina (Al_2O_3) is a widely used catalyst support in various catalytic processes, including ethanol reforming. It possesses several key properties that make it an attractive choice as a catalyst support. Porous aluminas are typically produced through a controlled dehydration process, which involves the removal of water from aluminum hydroxide, as depicted by Equation (1), or from aluminum oxide hydrates, as shown in Equation (2), as described by Ertl, Knözinger, and Weitkamp (2008). This controlled dehydration process results in the formation of porous structures with desirable properties for various catalytic applications.

$$Al(OH)_3 \longleftrightarrow Al_2O_3 + 3H_2O \tag{1}$$

$$AlOOH \longleftrightarrow Al_2O_3 + H_2O \tag{2}$$

The chemistry of aluminas is quite complex, with numerous crystallographic modifications or phases, each designated by Greek letters such as alpha (α), gamma (γ), delta (δ), eta (η), theta (θ), kappa (κ), and chi (χ). Among these phases, some of

the most commonly used as catalyst supports are α-Al_2O_3 (alpha-alumina), γ-Al_2O_3 (gamma-alumina), and η-Al_2O_3 (eta-alumina), as highlighted by Ertl, Knözinger, and Weitkamp (2008).

These different phases of alumina can exhibit variations in properties and are selected based on their suitability for specific catalytic applications. Alumina supports are commonly used in pollution control applications, where an alumina washcoat covers a monolithic support (ERTL; KNÖZINGER; WEITKAMP, 2008). Alumina has also been extensively employed as a support material in ethanol reforming catalysts.

Among the different phases of alumina, γ-Al_2O_3 stands out with the highest specific surface area, excellent thermal and mechanical stability. These properties made it particularly suitable for catalytic applications where a large surface area is required to facilitate catalyst deposition and enhance catalytic activity. In contrast, α-Al_2O_3 has the lowest specific surface area, which could be desirable in Partial Oxidation (POX) reactions, where unwanted byproducts can form due to side reactions. Using α-Al_2O_3 with low surface area minimizes these side reactions by reducing the number of exposed surface sites. Additionally, α-Al_2O_3 is renowned for its durability, and a low specific surface area contributes to the long-term stability of the catalyst, crucial for industrial processes requiring continuous and reliable operation over extended periods (ERTL; KNÖZINGER; WEITKAMP, 2008).

Another characteristic of α-Al_2O_3 is its ability to withstand high temperatures without undergoing phase changes because it is already in its highest oxidative state, where no further oxidative reactions are possible. This provides the material with its highest chemical and physical stability (PICONI, 2011).

Surface modifications, such as the addition of promoters or dopants, can further enhance the catalytic properties of α-Al_2O_3 and tailor it to specific ethanol reforming reactions. The choice of preparation methods can influence the surface characteristics of α-Al_2O_3 and, subsequently, the performance of supported catalysts (DAROUGHEGI; MESHKANI; REZAEI, 2020).

Platinum-based catalysts supported on α-Al_2O_3 have been explored to improve selectivity in ethanol reforming. Researchers can tailor these catalysts to achieve desired product distributions, such as higher hydrogen yield or syngas production (REN-YUAM; RONG-AN; LI-WU, 1984; POMPEO et al., 2007). In summary, aluminas demonstrate remarkable versatility and utility in a wide range of applications, from catalysts to support materials.

2.1.3 Active phase

The active phase of a catalyst is pivotal in determining catalytic activity, selectivity, and stability. It plays a critical role in facilitating reactions by providing sites for reactant adsorption and subsequent chemical transformations. The active phase of the catalyst

is a component that is directly involved in the catalytic reaction (HAO et al., 2020).

Autothermal Reforming (ATR) was performed using a broad range of catalysts, including noble metals, non-noble metals, and doped catalysts. Noble metals such as Rh, Pt, Pd, and Ru exhibit high activity and stability with low or no coke formation. However, due to their high cost, noble metals tend to be less economically viable for large-scale industrial use (OGO; SEKINE, 2020; BARUAH et al., 2015). As a result, among non-noble metal catalysts, Co, Ni, and Cu are widely used due to their relatively high catalytic activity and cost-effectiveness for large-scale industrial applications. Each metal has its unique characteristics and affinity, that must be evaluated to obtain the desired results in the reaction (CHIU; HORNG; CHOU, 2013).

In terms of ethanol conversion, selectivity, and stability, Rh is considered the best noble metal catalyst, while Ni stands out as the most efficient non-noble metal catalyst (OGO; SEKINE, 2020; BARUAH et al., 2015; CHIU; HORNG; CHOU, 2013). This was demonstrated in an experiment conducted by Chiu, Horng, and Chou (2013), which compared the performance of various noble and non-noble catalysts and found that Rh and Ni yielded the best results in terms of hydrogen production respectively.

2.1.3.1 Nickel

Nickel is a chemical element with the symbol Ni and atomic number 28. This material is characterized by its hardness, malleability, ductility, slight ferromagnetic properties, and its capacity to conduct both heat and electricity effectively. It is classified as a transition metal and can exist in various chemical forms, including alloys with aluminum or other metals, nickel salts, and nickel supported on metal oxides. Nickel is known for its ability to adopt both high-spin and low-spin electron configurations, allowing it to exhibit a range of stable oxidation states, including nickel(0), nickel(II), nickel(III), and nickel(IV). This versatility makes nickel a valuable element in a variety of chemical and industrial applications (DICCIANNI; LIN; DIAO, 2020).

Nickel alloys and nickel supported on various metal oxides, including alumina, are widely employed as catalysts in the decomposition of ethanol to produce hydrogen. Nickel, as a catalyst, plays a central role in the efficient production of hydrogen from ethanol. It is effective in breaking C-C bonds at relatively low temperatures, decomposing ethanol into hydrogen, and maintaining low concentrations of carbon monoxide (CO) while remaining stable during catalytic operations (LLORCA et al., 2013; OGO; SEKINE, 2020).

A common feature in catalysis is the use of $Ni(NO_3)_2{\cdot}6H_2O$ as a precursor salt of the active catalytic phase in purposely synthesized materials. They are usually selected because of their availability, low-cost, high solubility in water, and decomposition at moderate temperatures. Nevertheless, maintaining all other parameters and changing the Ni salt precursor could result in several different properties and catalytic performances

(MARCEAU et al., 2010; DI GIULIANO et al., 2019).

Ni is considered to be the optimal choice for hydrogen production through catalytic steam-reforming of ethanol. This preference is primarily attributed to its combination of low cost and high activity in ethanol decomposition by breaking the bonds of ethanol (C-C, O-H, and C-H bonds). Furthermore, it demonstrates remarkable activity in hydrogenation and dehydrogenation reactions, making it a versatile and efficient catalyst for this specific application (BSHISH et al., 2011; GATES; RUSSELL; YATES, 1986).

The major problems in utilize Ni-based catalysts are deactivation resulting from sintering and carbon deposition. To minimize these issues, one approach involves incorporating small quantities of different metals into the catalyst composition. This strategic alloying not only mitigates the deactivation problems associated with pure nickel catalysts but also enhances their overall catalytic performance (BAHARUDIN et al., 2022).

2.1.4 Promoters

Promoters are substances added in small quantities to a catalyst that can enhance the catalyst's performance. They can influence the catalyst's effectiveness activity, selectivity, and lifetime by altering its physical structure, such as crystallinity, increasing the number of active sites, or altering surface and pore sizes. Additionally, promoters can serve as electronic modifiers by changing the active sites, influencing the activation energy, and affecting the reaction kinetics of a catalytic reaction. Even in small amounts, promoters have been observed to have a significant impact on the properties of the oxide support (KOEL; KIM, 2008; SCHUMANN et al., 2015).

Over a century ago, Johann Wolfgang Dobereiner, one of the early researchers in catalysis, described the catalytic activity of certain combinations of substances, highlighting the improved efficiency of certain combinations compared to their individual components. In the 1870s, H. Deacon also studied the impact of added substances to his copper catalyst, such as sodium chloride, sodium sulfate, and magnesium sulfate and referring to them as ”accelerating substances”. The field of catalysis has grew rapidly since around 1900. Throughout this development, multicomponent catalysts have been widely employed with significant success, incorporating mixtures of various chemical constituents rather than one single chemical element or compound (MITTASCH; FRANKENBURG, 1950).

While some researchers began experimenting with multicomponent reactions in the early 20th century and attempted to describe the effect of adding multiple components to the catalyst, it was only with Haber's work that the term ”promoter” started to gain prominence. He coined this term based on his experiences from nitride experiments. As a result of these investigations, a highly efficient ammonia catalyst was

developed in the early 1910s, consisting of pure iron with a relatively small amount of aluminum oxide and a minor quantity of potassium oxide (MITTASCH; FRANKENBURG, 1950).

The role of promoters in catalysis, as demonstrated throughout the historical progression of this field, remains pivotal in enhancing catalytic processes. These substances, when added to catalysts, can significantly boost their performance with each promoter exerting a distinct influence on the properties of the materials involved. For instance, from the early 20th century potassium played a crucial role as a promoter in the synthesis of the iron-based ammonia catalyst, without it, the viability of this catalyst's production would not be practical. Alkali and alkaline promoters, such as those used in Ni catalysts, serve to enhance stability and selectivity. Furthermore, the strategic use of noble metals as promoters to boost activity in hydrogenation reactions underscores their capacity to amplify catalytic activity. (KOEL; KIM, 2008).

The foundations laid by pioneering scientists in their early experiments and discoveries have paved the way for the development of highly efficient catalysts. As our comprehension of catalysis advances, promoters continue to play a vital role in optimizing the efficiency and selectivity of diverse chemical reactions, offering promises for continued innovation and improvement in the realm of catalysis. In the context of our trimetallic catalyst, both copper and platinum act as catalytic metals, as well as promoters that amplify the catalytic properties of the others.

2.1.4.1 Copper

Copper is a chemical element with symbol Cu and atomic number 29. It possesses the qualities of being malleable, ductile, and is a highly efficient conductor of both heat and electricity, ranking second only to silver in terms of electrical conductivity. Classified as a transition metal, it is in a solid state at room temperature.

An often cited example of catalyst selectivity driven by its function is the conversion of ethanol. When catalyzed by copper, the reaction proceeds as described in Equation (3). Selectivity in this context is connected to the fact that copper has the ability to adsorb hydrogen and serves as a mild catalyst for hydrogenation and dehydrogenation reactions (SATTERFIELD, 1980).

$$C_2H_5(OH) \longleftrightarrow CH_3CHO + H_2 \tag{3}$$

In the case of single-metal copper-based catalysts, the tendency for copper to aggregate on the support's surface becomes more pronounced at higher temperatures, leading to a decrease in the catalyst's activity. This is the main reason why copper catalysts are often combined with other metals, with nickel being the prevalent choice. When copper was introduced as a promoter in this combination, it efficiently enhanced hydrogen production. It can overcome the inactivity of nickel and improve its perfor-

mance in the WGS reaction for hydrogen generation while preventing the growth of nickel particles. Copper is widely employed as a promoter when used in conjunction with nickel-based catalysts due to its effectiveness in catalyzing hydrogen production. The prominence of copper as a promoter is attributed to its dual functionality, actively participating in the WGS reaction and playing a crucial role in reducing the interaction between nickel species and the catalyst support. Therefore, the deliberate inclusion of copper as a promoter in nickel-based catalysts is essential for optimizing their catalytic efficiency (BSHISH et al., 2011).

Experiments conducted by Mariño et al. (2001) involved varying nickel contents (0, 1, 2.5, and 6 wt%) with two different copper contents (3 and 6 wt%). The findings revealed that gas yield increases as nickel and copper content rises. For the samples with 6 wt% nickel content and 6 wt% copper content, the gas yield was at least 2.6 times higher than that achieved with a 3 wt% nickel and 0 wt% copper content catalyst.

Additionally, Mariño et al. (2003) performed conversion and selectivity tests for hydrogen (H_2) using catalysts with 0 wt% copper and 6 wt% nickel. The results demonstrated that conversions increased from 10% for the 0 wt% copper and 6 wt% nickel sample to 70% for the sample with 6 wt% copper and 0 wt% nickel. Moreover, the sample with 6 wt% of both metals achieved even higher conversions, approaching nearly 85%. These experiments demonstrated the capability of bimetallic Ni-Cu catalysts to enhance ethanol conversions, ultimately leading to increased gas yield and enhanced hydrogen production.

In their study, Youn et al. (2006) investigated the potential of several second metals (Ce, Co, Cu, Mg, and Zn) as promoters for a Ni/γ-Al_2O_3 catalyst in the ATR of ethanol. All tested catalysts achieved complete ethanol conversion at 550 ℃, although the distribution of products varied depending on the second metal used. Among the tested second metals, copper (Cu) stood out as the most efficient promoter for a Ni/γ-Al_2O_3 catalyst in hydrogen production. This is attributed to the ability of Cu species to easily convert carbon monoxide (CO) and water (H_2O) into hydrogen through the WGS reaction. Simultaneously, Cu acts as a barrier, preventing the growth of nickel (Ni) particles, reducing the interaction between Ni species and γ-Al_2O_3, and facilitating the effective reduction of the Ni-Cu/γ-Al_2O_3 catalyst.

Furthermore, Youn et al. (2006) explored different copper quantities in the nickel catalyst and found that larger amounts of copper were not always more efficient. In their study, the sample containing 5 wt% of Cu, which maintained an intermediate state of Cu species between copper aluminate and copper oxide, exhibited superior performance in the ATR of ethanol compared to the sample with 7 wt% Cu. They suggest that this outcome may be due to the suppression of gasification activity over the larger Cu particles in the catalyst.

2.1.4.2 Platinum

Platinum ia a chemical element with symbol Pt and atomic number 78. It possesses malleable and ductile characteristics. It is a noble metal, belonging to the category of transition metals, platinum maintains its solid state at room temperature.

In Davda et al. (2004), the author discusses critical factors for optimizing conversion and hydrogen selectivity, which include C-C bond-breaking activity, effectiveness in the WGS reaction, and the prevention of undesired side reactions, likewise methanation. The author presents information indicating that platinum demonstrates reasonably good C-C bond-breaking activity (though not as high as metals such as Ru, Ni, Ir, and Rh) and appreciable performance in the WGS reaction. Nevertheless, copper exhibits the highest WGS rates among all metals, despite its inactivity in C-C bond breaking. While rhodium, nickel, and iridium exhibit the highest rates of methanation, platinum, iridium, and palladium display lower catalytic activities in methanation. Therefore, it can be inferred that Pt is expected to demonstrate suitable catalytic activity and selectivity for hydrogen production through the reforming of oxygenated hydrocarbons due to its advantageous properties, such as good activity in C-C bond breaking and WGS reactions, combined with low activity in methanation.

In the research conducted by Gutierrez et al. (2011), noble metals were investigated as catalysts in the ATR of ethanol. Mono-metallic catalysts with rhodium and platinum, as well as a bimetallic RhPt catalyst, were prepared, each with a 0.5 wt% total metal loading on a ZrO_2 support. The catalysts were denoted as $Rh_{0.5}$, $Rh_{0.25}Pt_{0.25}$, and $Pt_{0.5}$, with the subscript indicating the theoretical metal loading in wt%. Additionally, a commercial 15% NiO/Al_2O_3 catalyst was tested. The catalysts are referred to as Rh/ZrO_2, $RhPt/ZrO_2$, Pt/ZrO_2, and NiO/Al_2O_3. Among these catalysts, Rh/ZrO_2, $RhPt/ZrO_2$, and NiO/Al_2O_3 achieved complete ethanol conversion, while the Pt/ZrO_2 catalyst fell short of expectations. The Pt-only catalyst also exhibited less efficient hydrogen production. The author's hypothesizes that the catalytic effect of the Pt/ZrO_2 catalyst, and particularly the ZrO_2 support, was limited, and primarily cracking reactions were occurring, as the results resembled those obtained in the non-catalytic experiment. The results for hydrogen production on the Pt/ZrO_2 catalyst demonstrated suboptimal performance, which was comparable to the less expensive NiO/Al_2O_3 catalyst. However, when rhodium was combined with platinum ($RhPt/ZrO_2$), the catalyst achieved favorable results (GUTIERREZ et al., 2011).

2.1.5 Washcoat

Echave, Sanz, and Montes (2014) states that the most employed preparation method for coating monolith substrates is the washcoat technique with slurries. This method involves applying the support onto the bare monolith through washcoat. The

washcoat layer improves various characteristics of the catalyst, including surface area and dispersion of active phases (VITA et al., 2019).

The effectiveness of the washcoat process is strongly influenced by slurry stability and viscosity, which are highly sensitive to factors such as pH level (the acidity or alkalinity of the slurry controls the aggregate size), solid content (higher solid content can lead to increased viscosity and affect the overall stability of the mixture), particle size (smaller particles can lead to smoother and more even coatings), and the inclusion of additives. The addition of certain chemicals or compounds can alter the properties of the slurry, and these additives may be included to enhance stability, adjust viscosity, or improve adhesion during the washcoat process. Ensuring that these parameters are carefully controlled and optimized is essential for achieving consistent and effective washcoat results in various applications (ALMEIDA et al., 2010). To ensure the integrity of the washcoat layer and prevent ruptures or separation from the support material, it is essential to select a washcoat with a thermal expansion coefficient that closely matches that of the support. Additionally, a gradual incremental approach to drying and calcination temperatures should be adopted (TOMAŠIC; JOVIC, 2006; ALMEIDA et al., 2010).

The majority of oxide materials are fabricated from ceramic or metallic alloys, with common materials including cordierite, Al_2O_3, SiO_2, ZrO_2, TiO_2, carbon, zeolites, and others (VITA et al., 2019; TOMAŠIC; JOVIC, 2006).

2.1.6 Impregnation

The impregnation technique is a method employed to load catalytic metals onto a support material. This can be achieved through incipient wetness or dry impregnation, where both the support and the metal are in a solid state, and wet impregnation or soaking, where the metal and support are dissolved in minimally diluted liquid solutions (TUSAR; KAUCIC; LOGAR, 2013; PINNA, 1998).

One known problem in wet impregnation is the entrapment of air within the porous structure of the support when soaked in the liquid solvent. This trapped air is compressed as the fluid penetrates the support due to capillary pressure. The effectiveness of catalytic metal impregnation can be hindered, especially when using low-capillary-strength liquid solutions, as the liquid penetration ceases when the capillary pressure equals the pressure of the entrapped gas. Ultimately, the distribution of the dissolved precursor within the support is usually a function of factors such as diffusivity, pore structure, and metal-surface interactions (adsorption) (LEKHAL; GLASSER; KHINAST, 2001).

The impregnation process typically involves three phases. First, the support comes into contact with the catalytic solution for a sufficient duration to load the desired amount of metal. The next phase involves drying the support at an average temperature

ranging from 50 to 230 ℃ for a period of 12 to 48 h, removing solvents, humidity, and impurities. The final phase activates the catalyst by reducing the precursor and forming the metal oxide, usually through calcination (LEE; ARIS, 1985).

Moreover, during the impregnation process, it is possible to use more than one solute to load the metal into the support, a technique known as ”co-impregnation” or ”simultaneous impregnation”. Impregnation can also be carried out in a successive or sequential manner, with processes bearing these respective names. These methods are employed to increase the amount of metal loaded onto the support and ensure its uniformity (LEE; ARIS, 1985).

2.1.7 Drying

The drying phase constitutes the second step in the catalyst preparation process. During this stage, as the solvent evaporates, the solute precipitates, leading to a state of supersaturation in the solution. As mentioned before, the typical drying temperature is between 50 to 230 ℃, during which humidity and impurities are effectively removed from the catalyst (LEE; ARIS, 1985). Consequently, the catalyst experiences a reduction in weight ranging from 10 to 50%, as observed by Berrebi and Bernusset (1976).

To ensure the integrity of the catalyst and prevent the formation of cracks and defects within the structure as the solvent evaporates, it is vital to have a slow and gradual temperature increment during the drying process. This measured approach to temperature adjustment helps mitigate stress on the catalyst material (TOMAŠIC; JOVIC, 2006; ALMEIDA et al., 2010).

When the drying process occurs too fast, it can result in undesirable effects. Temperature gradients and capillary forces can compel the solvent to migrate to the external surface, leading to a decrease in the concentration of the solution within the inner pores of the catalyst material. Conversely, if drying is prolonged, the solvent on the outer surface will promote the diffusion of the precursor salt even deeper into the pores, resulting in an accumulation of the solution in the interior. These scenarios create concentration gradients within the catalyst material and non-homogeneity catalysts (DELMON et al., 1979; LEE; ARIS, 1985).

Non-uniform distribution of a component within the catalyst may also occur under several circumstances, including excessively rapid drying conditions, weak binding of the compound to the solid carrier, or non-homogeneous pore dimensions within the monolith structure (ERTL; KNÖZINGER; WEITKAMP, 2008).

The pore structure of a catalyst significantly influences the transport processes taking place within the porous medium. Capillary forces cause moisture migration within the pore structure, causing larger pores to dry first while smaller pores remain saturated. Consequently, a more uniform pore structure within the catalytic piece leads to more uniform drying (HOLLEWAND; GLADDEN, 1994).

During the drying process, vapor is removed from the support's saturated surface. Moisture transport within the support is sufficient to keep the surface saturated. Capillary flow transports liquid toward the external surface, while ions dissolved in the liquid phase are carried by liquid convection and diffusion. As drying proceeds, dry patches appear near the surface, and a drying front develops. Vaporization takes place within the solid, with convective vapor flow dominating moisture transport, while convective ion transport becomes negligible in this context (LEKHAL; GLASSER; KHINAST, 2001).

Therefore, it is crucial to optimize the rate of temperature increment during drying, avoiding extremes of too fast or too slow, to prevent these undesirable effects. The rate of drying is also contingent on the properties of the porous solid, the nature of the saturating liquid, and the prevailing ambient conditions (HOLLEWAND; GLADDEN, 1994).

Careful control of all these parameters and a comprehensive understanding of the factors are indispensable to achieve the desired quality and performance in the drying process and the resulting catalyst.

2.1.8 Calcination

Calcination, the third stage of the impregnation process, it's a thermal treatment to remove solvents, resulting in solvent-free materials (ERTL; KNÖZINGER; WEITKAMP, 2008). It occurs at elevated temperatures, converting active phase hydroxides to metal oxides by releasing chemically bonded CO_2 and H_2O, followed by the reduction of metal oxides to pure metal. This reductions are critical in the preparation of catalyst materials, as it helps convert the precursor compounds into their active and catalytically relevant states (PEREGO; VILLA, 1997).

Calcination brings some changes in the catalyst like: texture transformation via sintering, leading to the fusion of tiny crystals or particles into larger ones, structural modification, active phase generation, and establishment of mechanical resistance, essential for its stability and durability during use (PEREGO; VILLA, 1997).

Two examples of structural alterations occurring during calcination are documented in the studies by Perego and Villa (1997) and Le Page (1987). In the research conducted by Perego and Villa (1997), it is exemplified that as the temperature is raised, micropores within alumina collapse, leading to an enlargement in the average pore size. Similarly, Le Page (1987) conducted experiments and revealed that higher temperatures increased the size of platinum crystals.

Furthermore, research by Seo et al. (2010) on mesoporous nickel–alumina catalysts revealed that increasing the calcination temperature led to a decrease in the nickel surface area and nickel dispersion. This exemplifies how calcination can significantly impact the properties of catalyst materials (SEO et al., 2010).

2.2 ETHANOL REFORMING

Ethanol reforming is a valuable process for hydrogen production, and ethanol itself offers several advantages that make it an attractive choice for this purpose. Ethanol is considered environmentally friendly as it can be produced from renewable resources such as biomass, corn, sugarcane (aboudant in Brazil), reducing the carbon footprint associated with hydrogen production. It is often a cost-effective option, particularly when derived from readily available feedstocks, and it's relatively easy to store and transport. Ethanol also possesses a high energy content, making it a potent source of hydrogen when subjected to reforming processes (HARYANTO et al., 2005).

The reactions involved in ethanol reforming typically occur at high temperatures and can be realized through various processes, including Partial Oxidation (POX), Steam Reforming (SR), and Autothermal Reforming (ATR), which is a combination of the first two processes.

Hou et al. (2015) succinctly outlines the key reactions involved in ethanol reforming. These reactions can be summarized as follows:

Ethanol dehydrogenation:

$$C_2H_5OH \longrightarrow H_2 + C_2H_4O \tag{4}$$

Ethanol decomposition:

$$C_2H_5OH \longrightarrow CH_4 + CO + H_2 \tag{5}$$

Acetaldehyde decomposition:

$$C_2H_4O \longrightarrow CH_4 + CO \tag{6}$$

Methane steam reforming:

$$CH_4 + H_2O \longrightarrow CO + 3H_2 \tag{7}$$

Water gas shift:

$$CO + H_2O \longrightarrow H_2 + CO_2 \tag{8}$$

Ethanol dehydration:

$$C_2H_5OH \longrightarrow H_2O + C_2H_4 \tag{9}$$

Acetone formation:

$$2C_2H_4O \longrightarrow C_3H_6O + CO + H_2 \tag{10}$$

Table 1 provides a summary of the ethanol reforming process addressed. In the subsequent sections, a more detailed description of each of these reforming processes will be presented. These qualities position ethanol as a promising contributor to

clean and sustainable hydrogen generation, aligning with the global transition towards more sustainable and environmentally friendly energy sources reducing environmental impact.

Table 1 – Process techniques of ethanol reforming.

Process	**Co-Reactant**	ΔH_{298}
Partial Oxidation (POX)	O_2	-545 kJ/mol
Steam Reforming (SR)	Steam	173 kJ/mol
Autothermal Reforming (ATR)	O_2 and steam	$\approx$ 0 kJ/mol

ATR is an enthalpy neutral reaction for the stoichiometric reagent ratios given in Equation (16).
Source: Developed by the author (2022).

2.2.1 Partial Oxidation

Partial Oxidation (POX) is one of the processes used to convert ethanol into hydrogen. It is a strongly exothermic reaction that occurs when oxygen (or air) is supplied into the reactor, usually at high temperatures and with the presence of a catalyst. This process is characterized by its fast startup and response times. However, it yields the lowest amount of hydrogen compared to other reforming reactions (GHASEMZADEH; JALILNEJAD; SADATI TILEBON, 2019).

However, if a grader concentration of oxygen is provided, complete oxidation will take place, resulting in the formation of higher quantities of water vapor and carbon dioxide than hydrogen (NAHAR; DUPONT, 2014).

The generic equation of POX is represented by Equation (11):

$$C_nH_mO_k + (n - \frac{k}{2})O_2 \longleftrightarrow nCO_2 + \frac{m}{2}H_2,\ \Delta H_{298} < 0\ kJ/mol \tag{11}$$

The POX of ethanol that maximizes hydrogen production is known by Equation (12). Typically, this reaction produces 3 moles of H_2 per mole of ethanol (VITA et al., 2019).

$$C_2H_5OH + 1.5O_2 \longleftrightarrow 2CO_2 + 3H_2,\ \Delta H_{298} = -545\ kJ/mol \tag{12}$$

2.2.2 Steam Reforming

Steam Reforming (SR) is the most recurrent procedure employed to generate hydrogen. This process is endothermic and involves introducing high-temperature water steam into the reactor along with ethanol. To prevent carbon formation, excess steam is supplied along with an appropriate catalyst (NAHAR; DUPONT, 2014; AHMED; KRUMPELT, 2001).

By adding steam to the reaction, hydrogen production is favored, and the concentrations of CO are reduced due to the WGS reaction, as demonstrated in Equation (8) (NAHAR; DUPONT, 2014).

The reaction rate in SR is notably fast, however, hydrogen production is limited by thermodynamic equilibrium. Reactor designs are typically limited by heat transfer rather than by reaction kinetics. As a result, these reactors are designed to facilitate efficient heat exchange and tend to be substantial in size. Conventional steam reformers, which rely on indirect heat transfer (across a separator), may be less suitable for applications demanding rapid startup and dynamic response, such as automotive use (AHMED; KRUMPELT, 2001).

The generic equation of SR is specified by Equation (13):

$$C_nH_mO_k + (n-k)H_2O \longleftrightarrow nCO_2 + (n + \frac{m}{2} - k)H_2,\ \Delta H_{298} > 0\ kJ/mol \tag{13}$$

The SR of ethanol that generates the maximum production of H_2 is given by Equation (14). Usually, the reaction produces 6 moles of H_2 per mole of ethanol.

$$C_2H_5OH + 3H_2O \longleftrightarrow 2CO_2 + 6H_2,\ \Delta H_{298} = 173\ kJ/mol \tag{14}$$

2.2.3 Autothermal Reforming

Autothermal Reforming (ATR), as said before, combines Steam Reforming (SR) and Partial Oxidation (POX) reactions in an almost thermo-neutral process, minimizing the required energy input to maintain the reformer's temperature. To achieve thermal neutrality, 1.78 moles of water vapor and 0.61 moles of oxygen per mole of ethanol must be fed. This results in the production of 4.78 moles of H_2 per mole of ethanol (GRASCHINSKY et al., 2012).

Independent control of the steam-to-carbon and air-to-fuel ratios means that effective heat management can be achieved (RABENSTEIN; HACKER, 2008); (BRETT et al., 2012). In this process, POX provide the heat required and SR enhances the H_2 production yielding a hydrogen-rich gas as illustrated in Figure 3 (RABENSTEIN; HACKER, 2008).

Figure 3 – Autothermal reforming for ethanol.

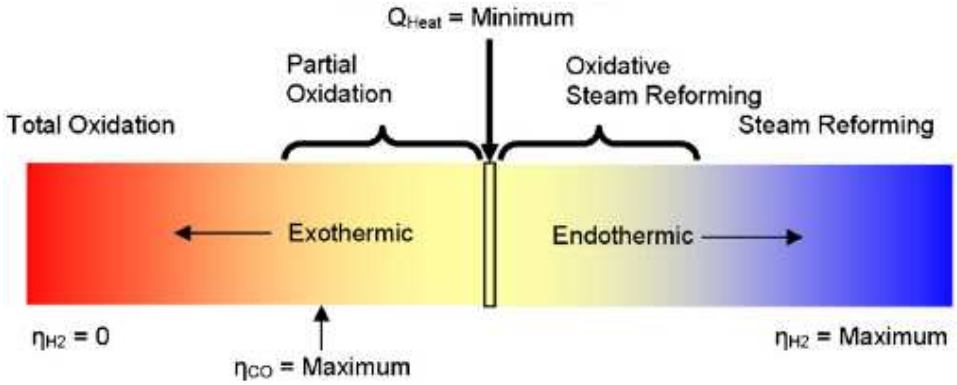

Source: Rabenstein and Hacker (2008).

For ethanol autothermal reforming, water steam, oxygen (or air), and ethanol are injected into the reactor (NIKOLAIDIS; POULLIKKAS, 2017; NAHAR; DUPONT, 2014). The use of a catalyst in ATR enables a smaller reactor size, faster start-up, lower operating temperatures, higher efficiency, and improved hydrogen purity (ASSABUMRUNGRAT; LAOSIRIPOJANA, 2009; NAHAR; DUPONT, 2014).

The generic equation of ATR accordingly with Ahmed and Krumpelt (2001) is Equation (15):

$$C_nH_mO_k + xO_2 + (2n-k-2x)(H_2O)_{(l)} \longleftrightarrow nCO_2 + (2n+\frac{m}{2}-k-2x)H_2,\ \Delta H_{298} \approx 0\ kJ/mol \quad (15)$$

The ATR of ethanol that maximizes hydrogen production is given by Equation (16).

$$C_2H_5OH + 0.61O_2 + 1.78H_2O \longleftrightarrow 2CO_2 + 4.78H_2,\ \Delta H_{298} \approx 0\ kJ/mol \quad (16)$$

2.3 STATE OF THE ART

This section explores the current state of the art regarding ethanol reforming with catalysts employing the washcoat and/or impregnation methods. An overview of the selected works can be seen in Table 2 where the most relevant catalyst fabrication parameters and efficiency indicators are listed for each work. The fabrication parameters consist of the catalytic agent, chosen support, monolith dimensions (when available), reaction parameters. The chosen efficiency indicators selected for comparison were the Ethanol Conversion (%) and Hydrogen Gas Yield (%).

The main articles referenced in the first and second chapters were incorporated in Table 2 that supplies metrics for evaluating the performance of the catalyst to be

developed in this work. Notably, the dimensions of the samples are quite small, differing significantly from catalysts implemented in vehicles. This discrepancy could lead to lower efficiency when scaling up the samples if the catalyst preparation process is not appropriately adapted for larger sizes.

Based on the literature, this work contributes to scientific progress by filling the following knowledge gaps:

- Developing a structured monolithic catalytic of Ni/Al_2O_3 and $Ni\text{-}Cu\text{-}Pt/Al_2O_3$ on samples with dimensions representative of those in industrial applications;
- Adapting the synthesis for structured catalysts with larger physical dimensions.

Table 2 – State of the art (part1).

Reaction	Catalysts /Support	Monolith Dimensions	Reaction Conditions	Ethanol Conversion	Hydrogen Yield	Results	Ref.
POX	Fe Co Ni Pt Pd Ru Rh /Al_2O_3	h=60 mm D=50 mm	Fuel flow rate=22.63 cc/min O_e=1	≥85%	25% 35% 45% 55% 55% 65% 70%	Noble metals could have better H_2 selectivity than non-noble. Between the non-noble metals Ni has the best hydrogen yield.	(CHIU; HORNG; CHOU, 2013)
POX	Ni/Al_2O_3	PPI=26 h=12.7 mm D=15 mm	T=440 ℃ 490 ℃ 540 ℃	15% 35% 40%	50% 40% 35%	Conversion and selectivity are higher in the foams with presence of nickel.	(PALM, 2018)
SR	Ni/Al_2O_3	PPI=26 h=12.7 mm D=15 mm	T=440 ℃ 490 ℃ 540 ℃	15% 12.5% 20%	65% 70% 67.5%	Conversion and selectivity are higher in the foams with presence of nickel.	(PALM, 2018)
SR	10%Ni/Al_2O_3	-	T=450 ℃ 550 ℃ 650 ℃	≥99.7%	57% 67% 66%	The highest hydrogen yield was identified at a temperature of 550 ℃.	(KHEMNARONG, 2021)
SR	1%Re-Ni 3%Re-Ni 5%Re-Ni /Al_2O_3	-	T=650 ℃ 650 ℃ 650 ℃	≥99.7%	65% 72% 67%	Small quantities of Re are capable of suppressing CO formation during the reaction thus, increases the selectivity towards CO_2 and H_2. Promotes long-term stability with up to 60 h without any deactivation observed.	(KHEMNARONG, 2021)
SR	5%Cu-5%Ni /γ-Al_2O_3	-	W_e=3 T=400 ℃ t=360 min	98%	77%	The order of impregnation of the metals modifies the reaction performance.	(MAIA et al., 2007)

Source: Developed by the author (2023).

Table 2 – State of the art (part2).

Reaction	Catalysts /Support	Reaction Conditions	Ethanol Conversion	Hydrogen Yield	Results	Ref.
ATR	20%Ni 20%Ni-3%Cu 20%Ni-3%Co 20%Ni-3%Zn 20%Ni-3%Ce 20%Ni-3%Mg /γ-Al_2O_3	T=550 °C	≥99.9%	45% 55% 46% 38% 39% 35%	The bimetallic Ni-Cu catalyst achieved a greater hydrogen yield, primarily due to the high activity of Cu in the WGS reaction. This efficiency is reflected in its ability to effectively convert CO and H_2O into hydrogen through the WGS reaction.	(YOUN et al., 2006)
ATR	20%Ni 20%Ni-3%Cu 20%Ni-5%Cu 20%Ni-7%Cu /γ-Al_2O_3	T=550 °C	≥99.9%	45% 55% 55% 44%	Among the tested catalysts, the Ni-5%Cu catalyst demonstrates the most favorable catalytic performance with respect to both hydrogen production and the composition of CO in the outlet stream.	(YOUN et al., 2006)
ATR	15%NiO/Al_2O_3 0.5%Rh/ZrO_2 0.25%Rh-0.25%Pt/ZrO_2 0.5%Pt/ZrO_2 -/ZrO_2	T=700 °C t=300 min	≥99.9% ≥99.9% ≥99.9% 60% 60%	33% 40% 35% 15% 14%	The highest ethanol conversion and selectivity for hydrogen were achieved with the Rh-Pt/ZrO_2 bimetallic catalyst.	(GUTIERREZ et al., 2011)
ATR	10%Ni/YSZ	T=300 °C 350 °C 400 °C	≥99%	44.1% 49.8% 50.0%	10%Ni/YSZ catalysts lead to almost complete conversion of ethanol and good selectivity at relatively low temperatures. An increase in the reaction temperature causes a decrease in Ni particle size with favored the yield to H_2.	(NIETO-MÁRQUEZ et al., 2013)
ATR	10%Ni/YSZ 15%Ni/YSZ 20%Ni/YSZ	T=400 °C	≥99%	50.0% 46.1% 40.5%	The addition of higher nickel loadings to the catalyst led to a reduction in its selectivity for H_2.	(NIETO-MÁRQUEZ et al., 2013)

Source: Developed by the author (2023).

3 MATERIAL AND METHODS

This section presents a general overview of the synthesis routes employed in catalyst preparation. Figure 4 illustrates this overview of the work through a graphical abstract, beginning with alumina foams coated with alumina, subsequently impregnated in Ni, Cu, and Pt solutions, and finally undergoing the autothermal ethanol reforming process. Additionally, it provides a detailed description of each step involved in the process, along with an explanation of the characterization methods used. The monoliths synthesized and characterized in this work, were identified according to the nomenclature in Table 3.

Figure 4 – Graphical abstract.

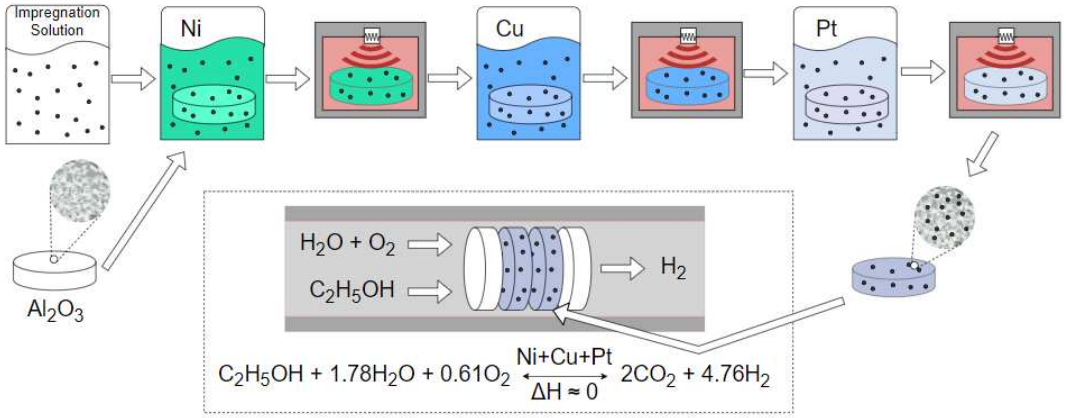

Source: Developed by the author (2023).

Table 3 – Nomenclature and specifications of the analyzed monoliths.

Nomenclature	**Procedure**
Al_2O_3	Monolith with washcoat
Ni/Al_2O_3	Washcoat and Ni impregnation
$Ni\text{-}Cu/Al_2O_3$	Washcoat, Ni and Cu impregnation
$Ni\text{-}Cu\text{-}Pt/Al_2O_3$	Washcoat, Ni, Cu and Pt impregnation

Source: Developed by the author (2023).

3.1 PROCESSING OF CATALYTIC MONOLITH

The methodology for producing the monolith was adapted from Palm (2018), Agrafiotis and Tsetsekou (2000) and Silva Júnior et al. (2023). Commercial foams composed of α-Al_2O_3, supplied by GoodFellow were employed as monolithic substrates. The foam specifications provided by the company are: porosity of 40 PPI, a thickness of 12.7 mm, and a diameter of 80 mm. Nevertheless, slight size variations were expected

due to their production process. Visual representations of the monolith are presented in Figure 5 and 6. Table 4 shows the equipment used for the monolith synthesis.

Table 4 – Description of the equipment used for the monolith synthesis.

Equipment	**Brand/Model**	**Location**
Magnetic stirrer	SPLabor SP160	LAC/UFSC
Analytical balance	Shimadzu ATX224	LAC/UFSC
Precision balance	BEL engineering LG3202i	LAC/UFSC
pH meter	Tecnal TEC-5	LAC/UFSC
Exhaustion hoods	Sppencer Equipments, SPLabor	LAC/UFSC
Distiller	Cristofoli	LAC/UFSC
Vacuum pump	Ionlab, VAC29	LAC/UFSC
Vacuum desiccator	Phlab	LAC/UFSC

Source: Developed by the author (2023).

Figure 5 – Commercial foam of α-Al_2O_3. Top view, with diameter measurement.

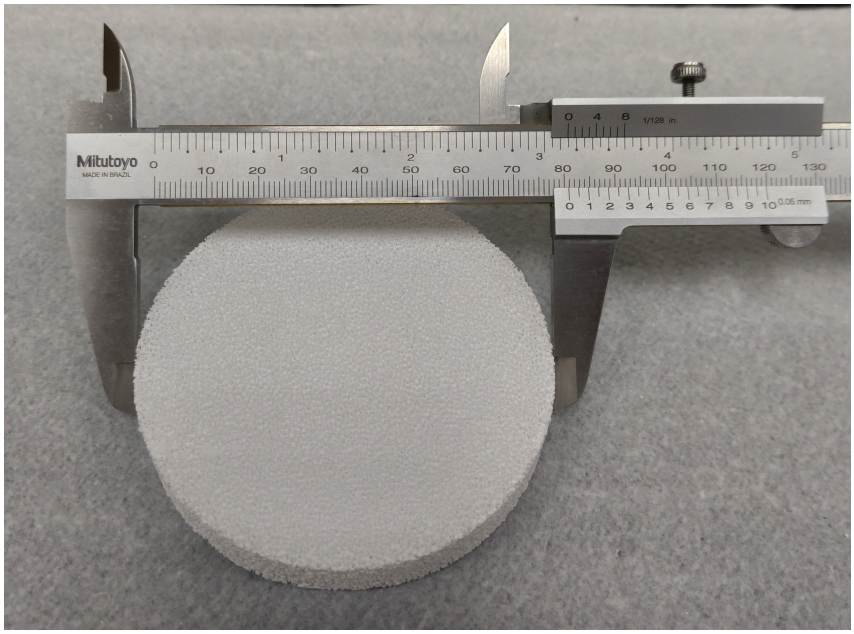

Source: Developed by the author (2023).

Figure 6 – Commercial foam of α-Al_2O_3. Profile view, with thickness measurement.

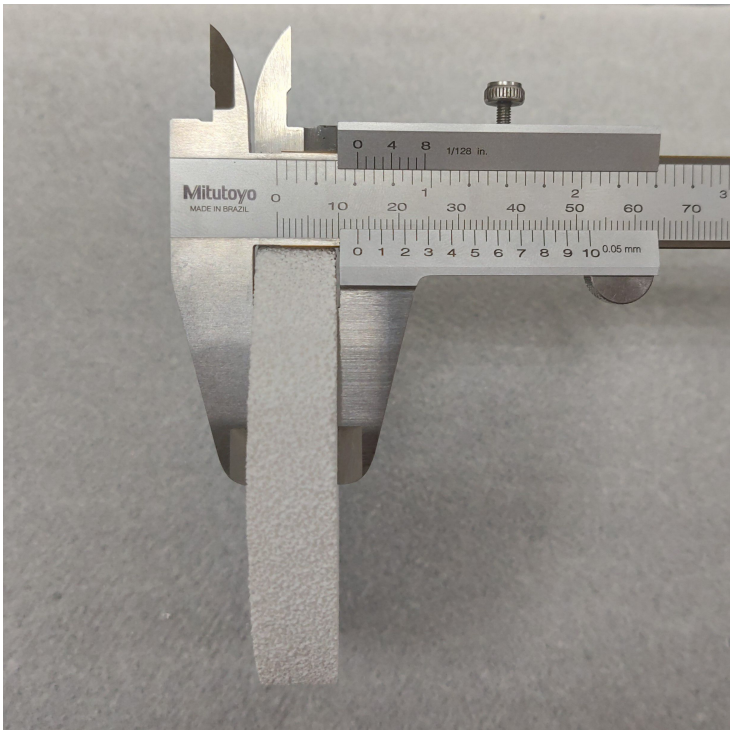

Source: Developed by the author (2023).

3.1.1 Washcoat

Figure 7 illustrates the process of washcoating. It started with preparing a slurry by mixing 40% alpha alumina powder with particle size ranging from 0.5 to 2 µm (CT 3000 LS SG supplied by Almatis) with 58% distilled water for one hour, utilizing a magnetic stirrer. Subsequently, 1% sodium silicate (PA supplied by Dinamica) and 1% nitric acid (65% purity, supplied by Dinamica) were added to the mixture, and stirred for an additional two hours. This resulted in a slurry with a 40% alumina mass concentration.

The pH of the slurry was carefully controlled within the range of 4 to 4.5, using solutions of sodium hydroxide (NaOH) and 0.1 M hydrochloric acid (HCl) as it had a significant impact on viscosity and, consequently, the thickness of the washcoat. Before the washcoat process, the monoliths were dried at 110 ℃ for one hour and weighed using an analytical balance. The monoliths were immersed in the slurry for one minute, the excess was removed by dripping for one min and the monolith was placed in contact with absorbent papers for subsequent drying, which lasted one and a half hours at 110 ℃, followed by a two-hour calcination at 600 ℃.

The washcoat mass content (C(%)) was calculated using the difference in monolith masses before (m_1) and after (m_2) the washcoat process, as shown in Equation

(17).

$$C(\%) = \frac{m_2 - m_1}{m_2} * 100 \quad (17)$$

Figure 7 – Fluxogram of alumina washcoat process.

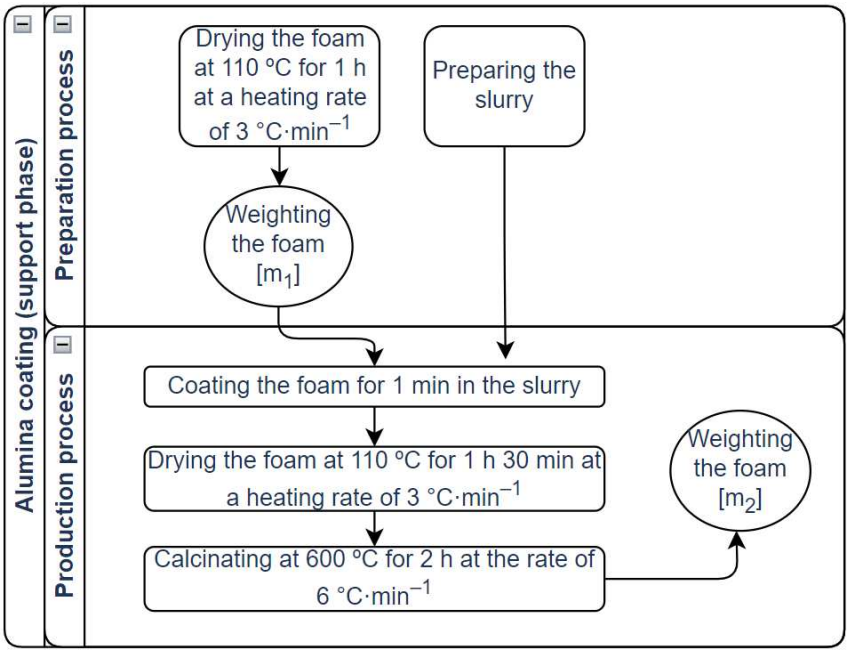

Source: Adapted from Palm (2018).

3.1.2 Impregnation

In the impregnation step, nickel, the active phase, copper, and platinum, the promoters, were sequentially impregnated into the alumina foam in the trimetallic monolith. In order to mitigate the entrapment of air due to capillary pressure, the impregnation step was carried out in a vacuum desiccator connected to a vacuum pump operating at 600 mmHg. For the nickel monolith, only the first impregnation stage was carried out. The nickel precursor was prepared using hexahydrate nickel nitrate ($Ni(NO_3)_2{\cdot}6H_2O$) (supplied by NEON) at a concentration of 2 M in an aqueous solution. The copper precursor was prepared with copper(II) nitrate trihydrate ($Cu(NO_3)_2{\cdot}3H_2O$) (supplied by NEON) at a concentration of 0.01 M in an aqueous solution. The platinum precursor was prepared using hexachloroplatinic (IV) acid hexahydrate ($H_2PtCl_6){\cdot}6H_2O$) (supplied by Sigma-Aldrich) at a concentration of 0.016 M in an aqueous solution. Nitrate was used as a competing ion and added to the platinum solution to achieve a $[NO_3^-]$:$[H_2PtCl_6]$ ratio of 20:1. To determine the appropriate mass quantities of each precursor compound, a simple adjustment was made proportionally to the mass ratios between the precursors and their corresponding elements. Molarity of the solutions were calculated

based in Equation (18) in order to obtain 10% by mass of Ni, 1% by mass of Cu and 0.5% by mass of Pt on the support.

$$Molarity = \frac{precursor\ mass}{volume * molar\ mass} \tag{18}$$

To calculate the addition in mass content for the nickel phase ($M_{Ni}(\%)$) the difference in monolith masses before (m_2) and after (m_3) impregnation was used as demonstrated by Equation (19).

$$M_{Ni}(\%) = \frac{m_3 - m_2}{m_3} * 100 \tag{19}$$

To calculate the addition in mass content for the copper ($M_{Cu}(\%)$) and platinum ($M_{Pt}(\%)$) phase the difference in monolith masses before (m_3) and after (m_4) copper impregnation and before (m_4) and after (m_5) platinum impregnation was used as shown in Equations (20) and (21).

$$M_{Cu}(\%) = \frac{m_4 - m_3}{m_4} * 100 \tag{20}$$

$$M_{Pt}(\%) = \frac{m_5 - m_4}{m_5} * 100 \tag{21}$$

Figure 8 – Fluxogram of the impregnation process.

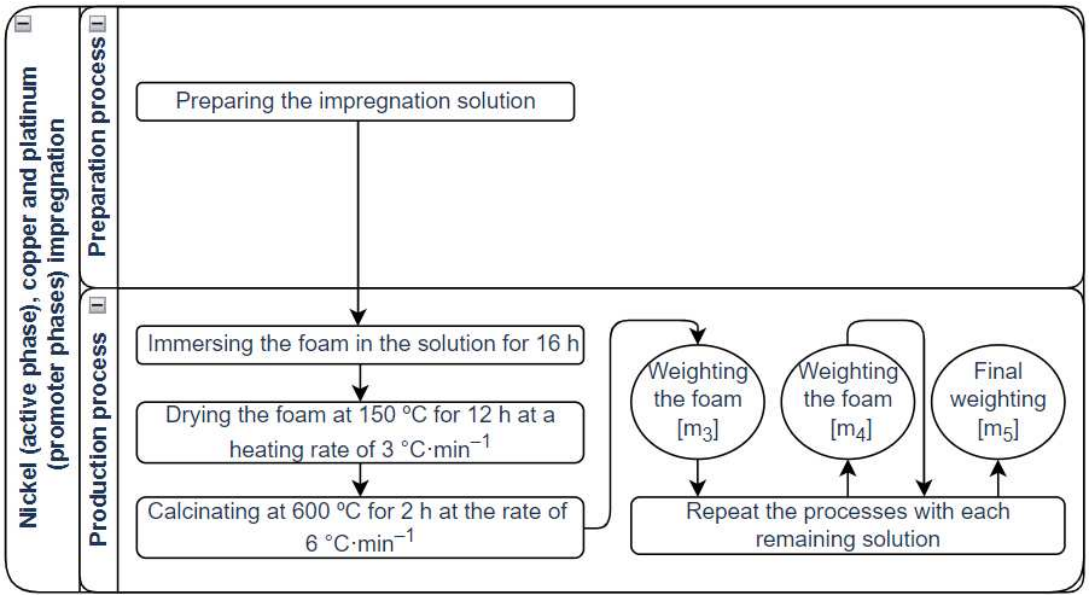

Source: Developed by the author (2023).

3.2 CATALYST CHARACTERIZATION

Characterizations of the catalysts are performed to determine their physical-chemical properties and ethanol conversion characteristics. The evaluations include X-Ray Diffraction (XRD), Scanning Electron Microscopy (SEM), X-Ray Photoelectron Spectroscopy (XPS) and Temperature Programmed Reduction (TPR). The equipment used for these analyses is described in Table 5.

Table 5 – Description of the equipment used for the monolith characterization.

Characterization	**Equipment brand/model**	**Location**
XRD	XRD-6000 SHIMADZU	CCT/ UDESC
SEM	JEOLJSM-6390LV	LCME/ UFSC
SEM	TESCAN MIRA3	LPP/ ITA
XPS	PHOIBOS 150 MCD	LFA/ UFMG
TPR	ChemBET Quantachrome	LAC/ UFSC

Source: Developed by the author (2023).

3.2.1 X-Ray Diffraction

X-Ray Diffraction (XRD) was initially discovered by Max Von Laue in 1912 when he announced it during a meeting of the German Physical Society at the University of Berlin (BORISOV; PODBEREZSKAYA, 2012). Laue was awarded the Nobel prize in 1914 for the discovery of XRD by crystals but later he stopped working on his research. It was William H. Bragg and his son W. L. Bragg who further studied and applied Laue's principles to determine the structure of various crystalline substances. Which resulted in a Nobel prize in 1915 for "their services in the analysis of crystal structure by means of X-rays", shared between them (THOMAS, 2012; MASCARENHAS, 2020).

The working principle of a θ–2θ diffractometer is illustrated in Figure 9. In this setup, a monochromatic (yellow) X-ray source is collimated using slits (S(%)) before and after reaching the sample. The sample is mounted on a support with a goniometer that can rotate the sample support through an angle θ, while the detector moves around the measurement circle at an angle 2θ, maintaining the geometry that satisfies Bragg's Law. Each type of crystalline plane in the sample is recorded as an X-ray peak by the detector. When there is no diffraction, only the scattered background radiation is recorded. The diffraction pattern is presented graphically, showing the intensity of the diffracted lines as a function of the diffraction angle. Larger peak sizes indicate a greater quantity of the same crystalline plane. Since each material has a unique arrangement and number of atoms in its unit cell, they will exhibit distinct diffraction patterns. Thus, the diffraction pattern consists of a series of superimposed patterns, one for each phase of the sample, and phases can be identified by comparing the patterns to cataloged ones (JAN; GAWĘDA; WAŚKOWSKA, 2021).

Figure 9 – Diagrammatic representation of the working of a θ–2θ powder diffractometer.

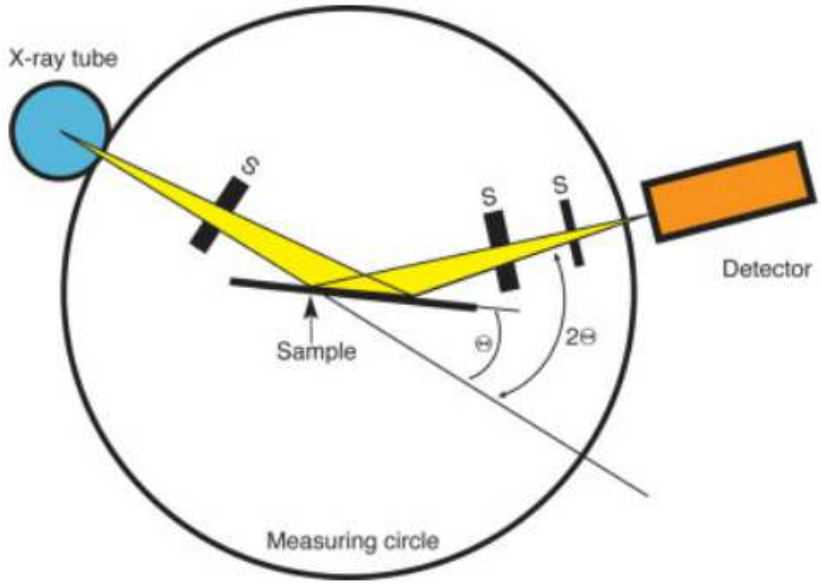

Source: Jan, Gawęda, and Waśkowska (2021).

XRD analyses were conducted using the XRD-6000 SHIMADZU diffractometer, available at the State University of Santa Catarina (UDESC). Copper tubes were utilized in the tests (Cu-Kα), providing a wavelength λ = 1.5420 Å. The scanning range for 2θ was set between 10° and 80°, and the scan speed was maintained at 3 °/min. XRD was employed to identify the various crystalline phases present in the samples and to estimate particle sizes. The obtained results were compared with the patterns of crystallographic planes thougth Profex 5.2.1. The particle diameter (dp) was determined with the Scherrer equation (Equation (22)).

$$dp = \frac{k\lambda}{(\beta cos\theta)} \tag{22}$$

Where k is the Scherrer constant that depends on the particle shape, typically assumes a value of 0.9, which was precisely the value employed in this study, λ is the X-ray wavelength, θ is the diffraction angle, and β is the Full Width at Half Maximum (FWHM).

3.2.2 Scanning Electron Microscopy

Scanning Electron Microscopy (SEM) is an analysis technique that employs an electron microscope to examine the exposed surface of a sample. SEM has evolved, with numerous modifications and improvements made by Professor Charles Oatley and his team, eventually leading to its modern form (MCMULLAN, 1996).

SEM uses a type of electron microscopy to emit beams of electrons that rapidly oscillate back and forth over the sample's surface, capturing high-resolution images

even when highly magnified. Variations in the sample's surface affect the pattern in which electrons are scattered. Depressions or fissures in the surface appear dark, while protuberances and bumps appear bright. This results in a three-dimensional image that provides information about the sample's surface topography and composition. Only surface structures can be examined with SEM (EMBRAPA, 2002).

Some SEM instruments are equipped with an Energy Dispersive Spectroscopy (EDS) system that can determine the chemical composition of the surface. This system emits high-energy electromagnetic radiation (X-rays) and ejects 'core' electrons (electrons not in the outermost shell), creating vacancies that higher-energy electrons can fill. When these electrons return to their original positions, they release energy with a specific wavelength, unique to each element on the periodic table. This principle is known as Moseley's Law, which correlates the emitted light's frequency with the atomic number of the element and this wavelength-based information allows the identification of elements through EDS (GASTON; PROTTER, 2022).

In this study, SEM was used to analyze the surface topography, morphology, and any irregularities in the samples. It was also employed to observe the distribution of particles within the washcoat and impregnation layers. EDS, was utilized to determine the chemical composition of the samples.

Insulating samples tend to accumulate an electrical charge from the primary electron beam, which can introduce artifacts in the images. To mitigate this, samples are typically coated with a conductive layer, often gold or carbon, which is applied in a vacuum. Depending on the specimen's dimensions, various types of adhesives may be used.

For this study, the catalysts were secured using carbon conductive glue and adhesive tapes, and a sputtering process with gold was performed to prevent charge accumulation. The SEM images were acquired using a Scanning Electron Microscope Field Emission JEOLJSM-6390LV at the Central Laboratory of Electron Microscopy (LCME) at UFSC and using a TESCAN MIRA3 at Department of Physics, Plasma and Processes Laboratory (LPP) at Aeronautics Institute of Technology (ITA) and dp were determined using ImageJ software.

3.2.3 X-Ray Photoelectron Spectroscopy

X-Ray Photoelectron Spectroscopy (XPS) analyses are grounded on the photoelectric effect, which was discovered by Heinrich Rudolf Hertz, a German physicist, in 1887 (BAER; THEVUTHASAN, 2010). In XPS, spectra are obtained by irradiating a material with an X-ray beam and measuring the number of electrons and their kinetic energy released from the sample upon irradiation (RIBEIRO et al., 2018).

Radiation induces the emission of photoelectrons from atomic layers of the elements in the sample. These electrons carry energy characteristics specific to the

element and molecular orbitals from which they originate. By counting the electrons detected at specific energy levels, a spectrum of peaks corresponding to the surface elements is generated. Running a survey spectrum of the samples reveals the elemental content present in the specimen (NASROLLAHZADEH et al., 2019). The elements present on the surface of the sample are characterized by determining the binding energies of the photoelectron peaks. The energy levels in the photoemission process are quantized, resulting in a peak kinetic energy distribution corresponding to the discrete electron shells of the photoionized atom (RIBEIRO et al., 2018). Typically, an XPS instrument consists of an Ultra-High Vacuum (UHV) chamber, an X-ray source, an ion gun, a sample handler, a spectrometer, an electron detector, and a computer for data acquisition and processing (NASROLLAHZADEH et al., 2019).

The main peak in an XPS spectrum represents the energy of electrons emitted directly from the inner energy levels of the atom when struck by an X-ray photon. However, due to more complex interactions like inelastic electron scattering, there is a probability that some electrons are emitted with slightly different energies, resulting in the so-called satellite peaks. Satellite peaks refer to additional intensity peaks that appear around the main peak of the analyzed element. These satellite peaks are associated with more complex interaction processes between incident X-ray photons and electrons in the sample (MOULDER, 1992). Information about the chemical composition of the sample was obtained through the integrated area of the peak, which is proportional to the number of atoms in the detected volume. XPS also determines oxidation states of elements present in a sample (NASROLLAHZADEH et al., 2019).

For each analyzed sample, spectra were collected from three distinct points to assess the local homogeneity of the elements. The measurements were conducted using a hemispherical energy analyzer, PHOIBOS 150 Multi Channeltron Detector (MCD), available at UFMG. X-rays were generated using the aluminum Kα line (1486.6 eV) with monochromatic radiation, model XR-50, and FOCUS 500 monochromator. A survey of all points was obtained with a pass energy of 200 eV, 10 scans, a dwell time of 10 ms, and a step size of 1.0 eV. High-resolution spectra of orbitals were obtained with a step size of 20 eV, 10 scans, a dwell time of 100 ms, and a step size of 0.025 eV. The orbitals analyzed were Ni2p, Cu2p, and Pt4d. The spectra were analyzed using the XPS PEAK41 software available in Scudiero (2006) and corrected using the method described in Greczynski and Hultman (2018). Background subtraction was performed using the Shirley (1972) method. The chemical composition was calculated using the method described in Ramade, Delatorre, and Duarte (2023) utilizing the Atomic Sensitivity Factors (ASF) presented in Wagner et al. (1979) and Wagner et al. (1982). This factor takes into account the efficiency of electron ejection from different orbitals.

3.2.4 Temperature Programmed Reduction

Temperature Programmed Reduction (TPR) is a technique used to reduce metal oxides, it was improved by scientist John Ward Jenkins. (GOLUNSKI, 2008). During TPR, a gas mixture containing hydrogen permeates the samples under analysis while the temperature is linearly increased with time. A Thermal Conductivity Detector (TCD) measures changes in the thermal conductivity of the gas stream. In the equipment, the TCD signal is converted into the concentration of active gas.

The area under the TPR curve is used to qualitatively compare the concentration of an element present in the samples. However, sample conditions such as sample weight, time, temperature, and heating rate must remain consistent across tests (HUANG; XUE; SCHWARZ, 1988; MICROMERITICS, 2022).

Figure 10 provides an example of a TPR profile. The maximum temperature value indicates the maximum rate of reduction (MICROMERITICS, 2022).

Figure 10 – Temperature-programmed reduction profile for a metal oxide.

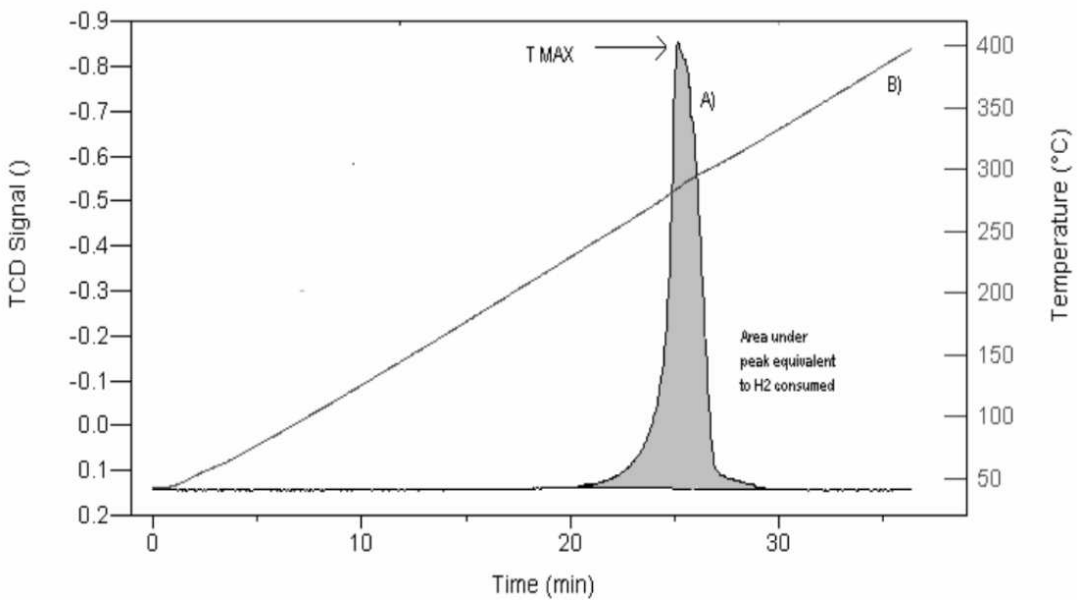

Source: Micromeritics (2022).

All samples go through a degassing process before being submitted to any analysis to eliminate volatile compounds and unwanted impurities. The process involves heating a U-shaped tube containing the samples up to 300 ℃ while a stream of N_2 gas (99.9% purity) flows through the sample for three hours. After that, the sample can be disconnected from the degassing station and connected to the analysis station without risk of contamination from ambient air. The monolith was cut and separated into smaller pieces for analysis. Samples were collected from its most external layer and from the core of the monolith.

TPR analyses were conducted to determine the ideal working temperature window of the catalyst and to qualitatively compare the difference in concentration of the different metal phases in the external and internal regions of the monolith.

TPR was carried out using QuantaChrome's ChemBET Pulsar from UFSC with the following conditions:

- Flow of 5% H_2 mixture with 95% N_2;
- Heating rate of 10 °C/min from 10 °C to 800 °C;
- 100 mg of sample material.

3.3 CATALYTIC TESTS FOR ETHANOL AUTOTHERMAL REFORMING

This section outlines the equipment, procedures, and operational details for obtaining ethanol conversion efficiency results, including the selectivity of hydrogen and other gaseous products during the autothermal reforming of ethanol. The test bench was divided into two separate streams: one for the flow of nitrogen, ethanol, and water, and another for air (composed of oxygen and nitrogen), both of which were directed into the reactor.

3.3.1 Test bench

Figure 11 illustrates the experimental setup developed by Vidal (2023) and used in this work, starting from the gases inlet until the outlet of the reformed gases, going directed toward the chromatograph for analysis. The reactor assembly incorporates 310 stainless steel due to its good weldability, resistance to corrosion and high temperatures, and low thermal conductivity.

Figure 11 – Schematic representation of the experimental bench.

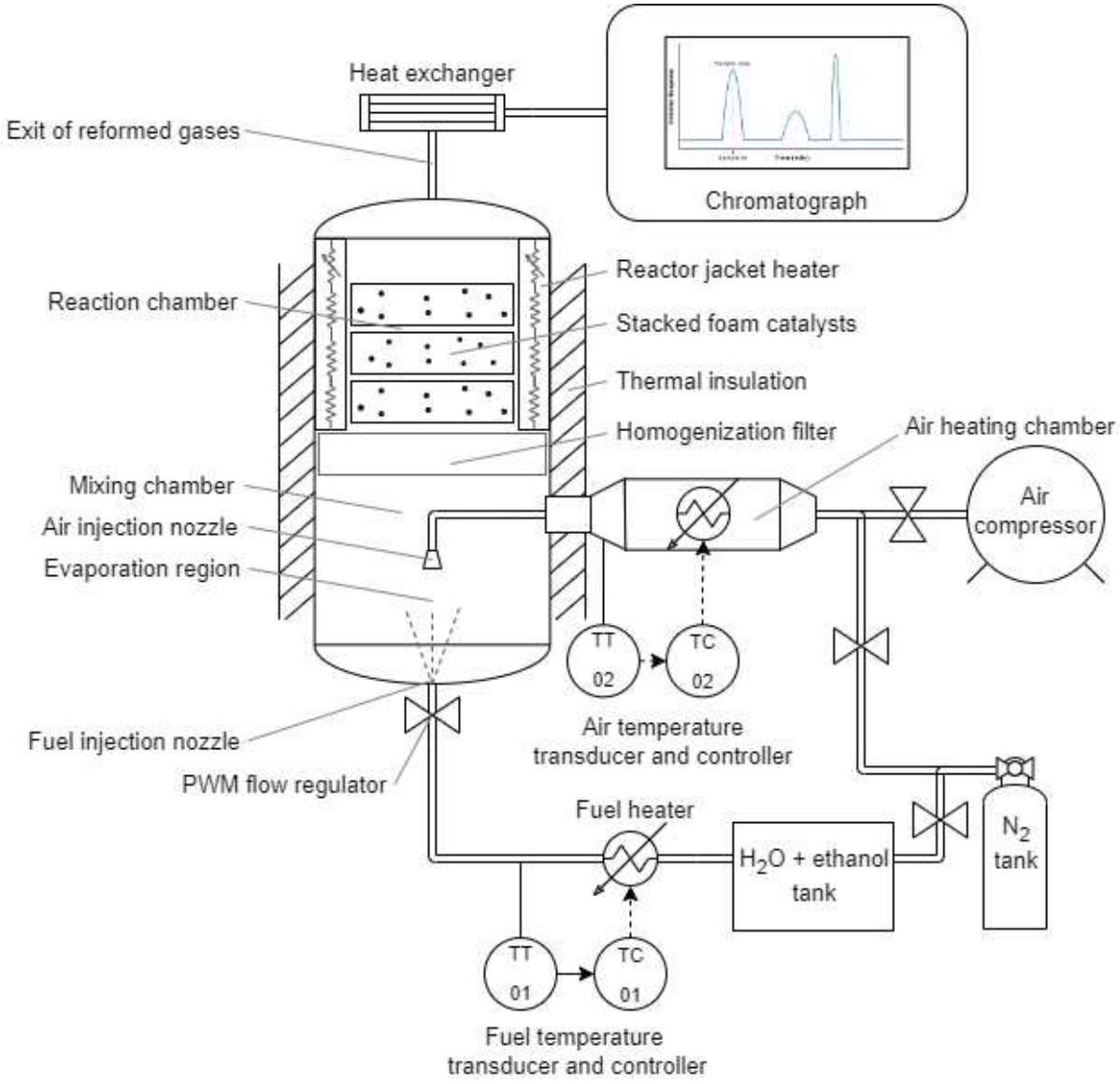

Source: Adapted from Vidal (2023).

3.3.1.1 Bench operation procedure

Figure 12, illustrates the experimental configuration of the bench operation procedure used in this study. Throughout the experimental procedure, the reactor operated at atmospheric pressure. The heating process began with pressurized air flowing at a rate of 12 Liters Per Minute (LPM), the oven temperature controller was set to 700 ℃ and the mixing chamber was set to 320 ℃.

The mixture chamber was responsible for heating the evaporation region. When the reactor reached the predefined temperatures, the catalyst activation step was initiated. Air heating and pressurized airflow were interrupted, and a 10 LPM N_2 flow was introduced for 5 min to purge the system of any residual air. Following this period, a gas

mixture comprised of 5% H_2 in 95% N_2 was introduced at a rate of 0.8 LPM for 30 min. Throughout this duration, the reactor was maintained at 700 ℃.

After 30 min, the air heating with N_2 flow was resumed until the mixing chamber reached a minimum of 320 ℃. Then, the oven temperature was set to the temperature test and the system was ready to start the reforming process. The test flow rates were adjusted to N_2 17.47 LPM and pressurized air 1.63 LPM. After 10 min of stable temperature, the test started with the fuel introduction through an electronic PWM system and the activation of the injector nozzle, facilitating the vaporization of the reactants in this region.

Following vaporization, the heated gases pass through the homogenization filter and proceed towards the reaction chamber. Within this zone, the gases pass through the catalysts, initiating the reforming process. The reaction chamber is heated using electrical resistance. After 3 min of the reforming process, the fuel nozzle and N_2 were deactivated, and the pressurized airflow was increased. At the end of the 3 min, a 2 mL sample of the reformed gases was sent to the GC using a sampling loop passing through a water-cooled heat exchanger. The heat exchanger, characterized by a three-necked round-bottom glass flask enclosed in a plastic box containing water and ice, cooled the reformed gases as they passed through the flask, bringing them to ambient temperature for subsequent analysis on the GC. After each test, the monolith underwent a regeneration stage at 700 ℃ with a pressurized airflow of 12 LPM for 30 min.

Figure 12 – Heating step reactor to 700 ℃.

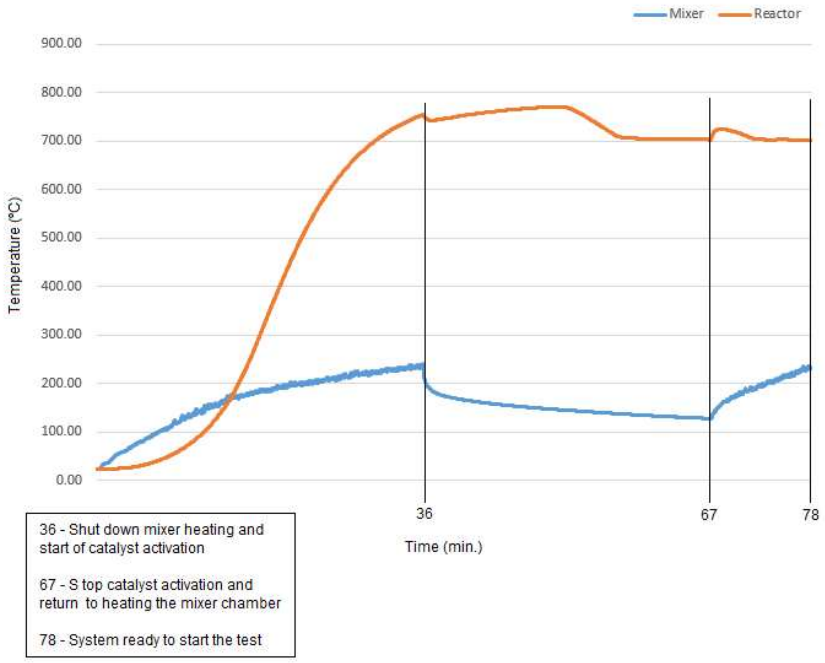

Source: Vidal (2023).

3.3.2 Weight Hour Space Velocity

In the context of catalytic testing for ethanol autothermal reforming, Weight Hour Space Velocity (WHSV) plays a crucial role in assessing the efficiency of the catalytic process. WHSV, defined as the mass flow rate of the feed per hour divided by the weight of the catalyst utilized, as described by the Equation (23), provides insights into the reaction kinetics and the catalytic system's performance.

$$WHSV = \frac{\dot{m}_{total}}{\sum m_{i,cat}} \tag{23}$$

Typically, the weight of the catalyst charged into the reactor remains constant, and any variation in the flow of liquid per hour results in a change in WHSV. However, due to the experimental constraints related to the limited flow rates in our study, the approach taken involved altering the mass of the catalyst inside the reactor. In these experiments, the unalterable nature of the liquid flow necessitated a creative adjustment, leading to the manipulation of the catalyst mass as a practical alternative. Specifically, the catalyst mass was varied by employing two or three monoliths in the reactor. This modification, involving the alteration of the catalyst mass using two or three monoliths, was implemented to investigate the impact of WHSV variations on the catalytic process within the confines of our experimental limitations. The influence of WHSV on reaction rates and selectivity was explored, contributing to a comprehensive understanding of the catalytic behavior under varying conditions.

For the calculation of WHSV, the flow rates of nitrogen and pressurized air were fixed at 17.47 LPM and 1.63 LPM, respectively. It was defined that the mass of one catalyst sample is equivalent to 55 g. Then, the volumetric flow rates of nitrogen and oxygen were calculated, followed by the calculation of the total volumetric flow rate. Knowing the mass flow rate of oxygen and the stoichiometric molar ratios, the mass flow rate of the fuel was calculated. By summing the mass flow rates of the fuel with those of nitrogen and oxygen, the total mass flow rate in g/min was obtained. The values utilized for these calculations are outlined in Table 6. With a total mass flow rate of 24.75 g/min, multiplying by 60 to convert the result to hours, dividing it by the mass of 2 catalysts (110 g) provides a WHSV of 13.5 h^{-1}, and dividing by the mass of 3 catalysts (165 g) provides a WHSV of 9 h^{-1}.

Table 6 – Constants.

Constants	Value	Unit
Volume of N_2/Air	0.79	dimensionless
Volume of O_2/Air	0.21	dimensionless
Density of N_2	0.001146	g/cm^3
Density of O_2	0.001309	g/cm^3
Molar weight O_2	31.9988	g/mol
Molar weight C_2H_5OH	46.0684	g/mol
Molar weight H_2O	18.0153	g/mol

Source: Developed by the author (2024).

3.3.3 Gas chromatography

The concentration of products in the ethanol autothermal reforming system was determined using gas chromatography analysis with a Perkin Elmer Clarus® 580 Gas Chromatograph (GC) equipped with a TCD which detects H_2, O_2 and N_2, and the Flame Ionization Detector (FID), which detects carbonic species.

Samples were introduced into the chromatograph column, Rt-U-BOND and Elite GC GS-Molesieve, 30 m long and with an internal diameter of 0.53 mm (manufactured by Restek). The GC collects a 2 ml fraction of the reformed gases and generates a graphical report with values in µV across time (min), area in µV·s, and concentration in µmol/mol for each chemical species. These concentration values from the report were used to calculate the molar fraction of each component.

3.3.3.1 Catalyst Monolith Performance

Ni/Al_2O_3 and Ni-Cu-Pt/Al_2O_3 catalysts were tested for the ATR of ethanol. The temperatures and WHSV values utilized can be found in the Table 7. Selectivity is commonly defined as the percentage of the reactant consumed in a reaction that results in the formation of the desired product. It usually depends on both the degree of conversion and the composition of reaction products. On the other hand, ”yield” is a term often used in engineering and industrial contexts, that describes the amount of product formed per unit of feedstock (reactant) consumed during the entire operation of a reactor or process (SATTERFIELD, 1980).

The calculation for ethanol conversion was illustrated in Equation (24), where F_{inlet} and F_{outlet} were the fuel molar concentrations (μmol/mol) at the reactor's inlet and outlet, respectively. The gas selectivity of the products was determined by the ratio of moles of the desired product to the total moles of the reformed gases, excluding C_2H_5OH, O_2, N_2, and H_2O, as depicted in Equation (25), where P_{outlet} was the product molar concentration at the system outlet and RG_{outlet} was the molar concentration of the reformed gases reactor's outlet. Table 7 presents the parameters used in the

performed tests.

$$X(\%) = \frac{(F_{\text{inlet}} - F_{\text{outlet}})}{F_{\text{inlet}}} * 100 \tag{24}$$

$$S(\%) = \frac{P_{\text{outlet}}}{RG_{\text{outlet}}} * 100 \tag{25}$$

Table 7 – Parameters of performed tests.

Nomenclature	**Temperatures (°C)**	**WHSV (h^{-1})**
Ni/Al_2O_3	400, 500, 600, 700	13.5
$Ni\text{-}Cu\text{-}Pt/Al_2O_3$	400, 450, 500, 550, 600, 650, 700	13.5
$Ni\text{-}Cu\text{-}Pt/Al_2O_3$	400, 450, 500, 550, 600, 650, 700	9

Source: Developed by the author (2022).

4 RESULTS AND DISCUSSION

This chapter presents the synthesis results, including the washcoat and each impregnation mass content. Subsequently, it discusses the initial findings of the characterization techniques and the ethanol autothermal reforming process. Additionally, all the samples were sent for analysis after the calcination step. Finally, a comparison of the ethanol autothermal reforming results was made at each selected temperature for the various catalysts.

Conducting reforming tests required a considerable amount of time, particularly when conducted across various temperatures to comprehensively assess catalyst performance. In this specific case, technical difficulties with the reactor and chromatograph significantly increased the time required for conducting tests at all planned temperatures. Consequently, due to time limitations and practical constraints associated with equipment availability and operation, it was impracticable to execute the reforming tests on the Ni-Cu/Al_2O_3 monolith. Furthermore, due to restrictions on the number of samples that could be sent to the laboratories each time, only some characterizations could be performed in Ni-Cu/Al_2O_3 monolith.

The monoliths developed in this study and those subjected to characterization were designated based on the nomenclature outlined in Table 3. Additionally, Table 7 provides an overview of the parameters employed in the performed tests.

4.1 WASHCOAT MASS CONTENT

The washcoat mass content (C(%)) was determined using Equation (17), and the results are presented in Table 8.

Table 8 – Washcoat mass content.

Sample	**m_1 (g)**	**m_2 (g)**	**C(%)**
1	40.92	50.40	18.80
2	39.18	48.16	18.64
3	41.73	52.79	20.95
4	42.10	50.86	17.22
5	42.80	52.03	17.74
6	41.04	50.80	19.21
7	40.89	51.32	20.32
Average	-	-	19.0
Standard deviation	-	-	1.3

Source: Developed by the author (2023).

4.2 IMPREGNATION MASS CONTENT

The results for nickel impregnation mass content (M_{Ni}(%)) are presented in Table 9, calculated using Equation (19). Table 9 further displays the outcomes of copper impregnation mass content (M_{Cu}(%)) as determined by Equation (20). Similarly, Table 9 exhibits the results for platinum impregnation mass content (M_{Pt}(%)), calculated using Equation (21).

In the study on competitive adsorption by Silva Júnior et al. (2023), it was well-established that nitric acid (HNO_3), utilized in the impregnation process, was recognized for its highly corrosive nature. Their findings align with the expectation that HNO_3 induces minimal to no mass gain. It is more common to expect a certain degree of mass loss when materials are exposed to HNO_3. This corrosive action arises from the compound's ability to break down substances through oxidation and other chemical reactions, potentially leading to the dissolution or decomposition of materials and ultimately causing a reduction in their mass.

Table 9 – Impregnation's mass content.

Sample	**m_2 (g)**	**m_3 (g)**	**m_4 (g)**	**m_5 (g)**	**M_{Ni}(%)**	**M_{Cu}(%)**	**M_{Pt}(%)**
1	50.40	55.89	56.16	56.12	9.83	0.48	-0.08
2	48.16	53.37	53.65	53.63	9.76	0.53	-0.04
3	52.79	58.46	58.77	58.55	9.70	0.53	-0.38
4	50.86	56.37	56.67	56.50	9.77	0.53	-0.30
5	52.03	57.27	57.56	57.50	9.15	0.50	-0.10
6	50.80	56.21	56.52	56.47	9.62	0.55	-0.09
7	51.32	56.70	57.01	56.94	9.49	0.54	-0.12
Average	-	-	-	-	9.62	0.52	-0.16
Standard deviation	-	-	-	-	0.24	0.02	0.13

Source: Developed by the author (2023).

4.3 CATALYST CHARACTERIZATION

In this section, the obtained characterization results for X-Ray Diffraction (XRD), Scanning Electron Microscopy (SEM), Energy Dispersive Spectroscopy (EDS), X-Ray Photoelectron Spectroscopy (XPS) and Temperature Programmed Reduction (TPR) were presented.

4.3.1 X-Ray Diffraction

The XRD patterns of the samples are shown in Figure 13. Each peak corresponds to a crystalline plane, measured in arbitrary units. The most intense alumina peak occurs at a 2θ of 57.5° with a dp of 50 nm.

Cubic-NiO was identified in the samples containing nickel, with peaks observed at 2θ values of 37.1°, 43.1°, 62.6°, 75.1°, and 79.1°, which can be related to (hkl) planes of (1 1 1), (2 0 0), (2 2 0), (3 1 1), and (2 2 2), respectively. The most intense cubic-NiO peak occurred at 2θ of 43.1°, corresponding to a dp of 36 nm. The formation of cubic-NiO provides excellent thermal stability, enabling it to withstand high-temperature operating conditions. Its strong mechanical resistance contributes to the durability of the catalyst, ensuring sustained performance over extended periods (CARDENAS; SERBENA, 2021).

Copper peaks were absent in Ni-Cu-Pt/Al_2O_3 internal samples, while in external samples, Cu exhibited a maximum Relative Intensity (RI) of 1.16% at 2θ of 43.1°. Platinum peaks in the Int and Ext samples showed a maximum RI of 0.32% at 2θ of 28.0° and 0.84% at 2θ of 34.9°, respectively. However, these peaks were not distinguishable in the XRD image due to limitations in the technique's visualization capabilities. Additionally, background noise made it challenging to detect peaks with low intensities.

Figure 13 – XRD spectra of (a) Al_2O_3, (b) Ni/Al_2O_3 Int, (c) Ni/Al_2O_3 Ext, (d) Ni-Cu-Pt/Al_2O_3 Int, and (e) Ni-Cu-Pt/Al_2O_3 Ext samples.

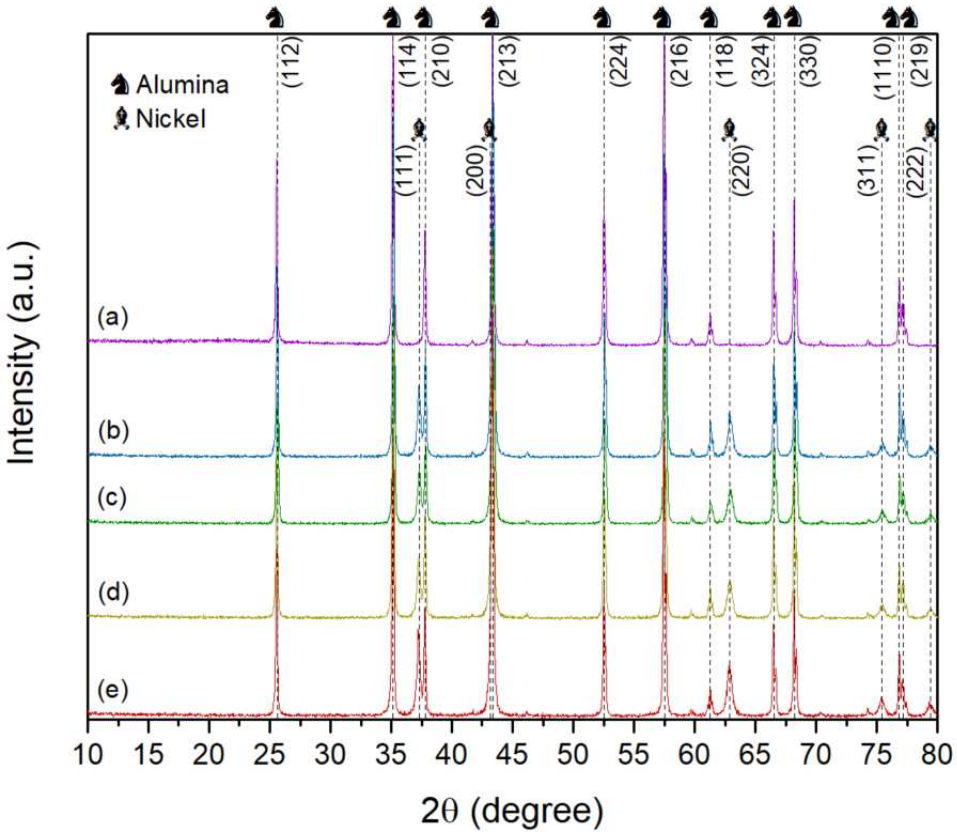

Source: Developed by the author (2023).

4.3.2 Scanning Electron Microscopy

This section provided the SEM images obtained during the research. They reveal all the layers in the trimetallic catalyst precursor, providing insights into the surface morphology and topography.

Figure 14 and Figure 15 focused on the washcoat stage, which exclusively features alumina. They provided a comprehensive examination of the sample's surface. Figure 14 underscores a well washcoated surface. Notably, the SEM images reveal consistent washcoat quality, with only sporadic areas exhibiting substrate exposure, potentially induced by the substrate geometry, hindering the attachment of the washcoating layer. These isolated areas lacking washcoat are minimal in extent and do not significantly impact the overall uniformity of the washcoat across the entirety of the monolith. Critically, the absence of pore blockage is evident, indicating the successful application of the alumina washcoat.

The exposed region in Figure 15 correlates with the necessity to reduce the sample thickness from its initial dimension of 80 mm to the analysis scale of 5 mm. To achieve this reduction, a sample breakage was implemented. As a result of this process, portions of the specimen that were inaccessible during the washcoat application became exposed, revealing the underlying surface in the SEM images. With this it is feasible to visually identify the distinction between the whascoat layer and the alumina foam. This exposed part would not have been visible if it had not been necessary to break the sample for analysis, consequently, this did not occur in the catalysts.

Figure 14 – SEM of Al_2O_3 monoliths at (a) x22, (b) x100, (c) x1,000, and (d) x5,000 magnifications.

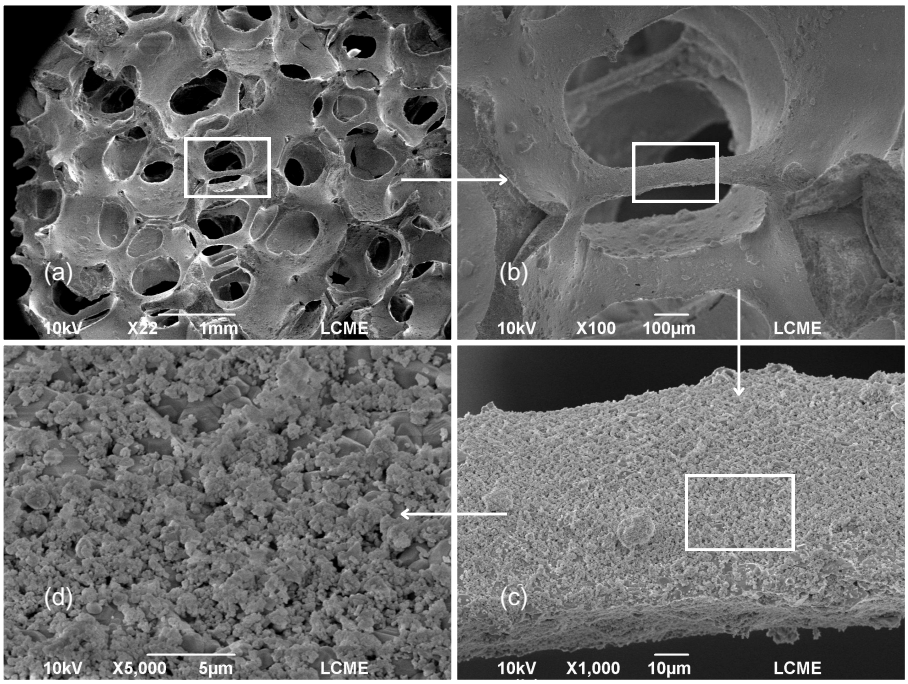

Source: Developed by the author (2023).

Figure 15 – SEM of Al_2O_3 monoliths area uncovered by washcoat at (a) x22, (b) x100, (c) x1,000, and (d) x5,000 magnifications.

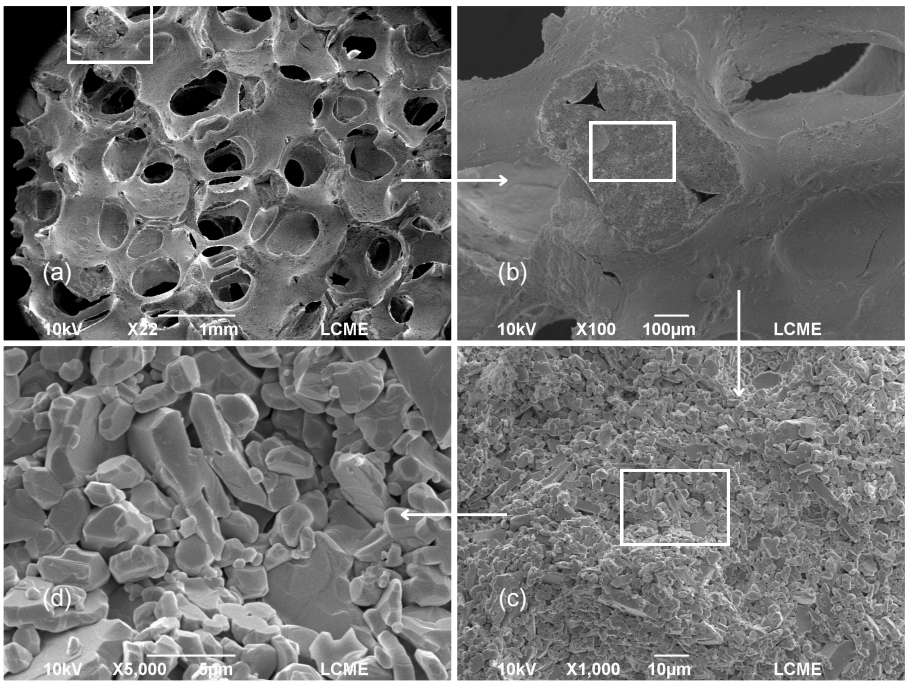

Source: Developed by the author (2023).

Transitioning to the monolith stage up to the first impregnation, Figure 16 portrays a monolith with a successful and evenly distributed nickel impregnation, showcasing the efficacy of the applied methodology. While Figure 17 reveals the aspect of the monolith breakage observations with exposed sections made in Figure 15. The fracture in Figure 17 similarly exposes regions lacking nickel impregnation with a distinction that some nickel particles have migrated to the exposed broken surface.

Figure 16 – SEM of Ni/Al_2O_3 monoliths at (a) x22, (b) x100, (c) x5,000, and (d) x10,000 magnifications.

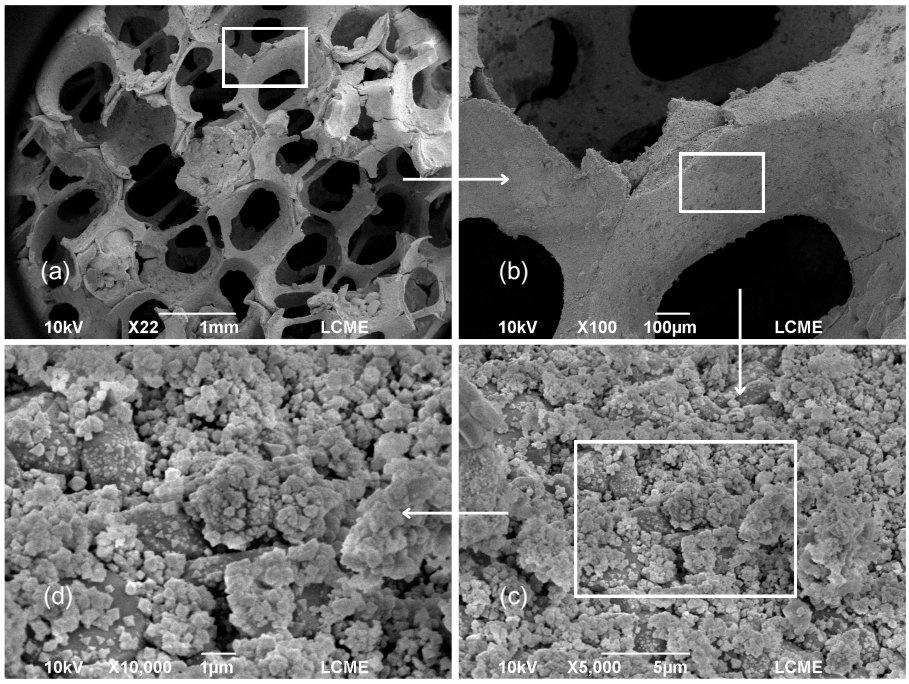

Source: Developed by the author (2023).

Figure 17 – SEM of Ni/Al_2O_3 monoliths uncovered area at (a) x22, (b) x100, (c) x5,000, and (d) x10,000 magnifications.

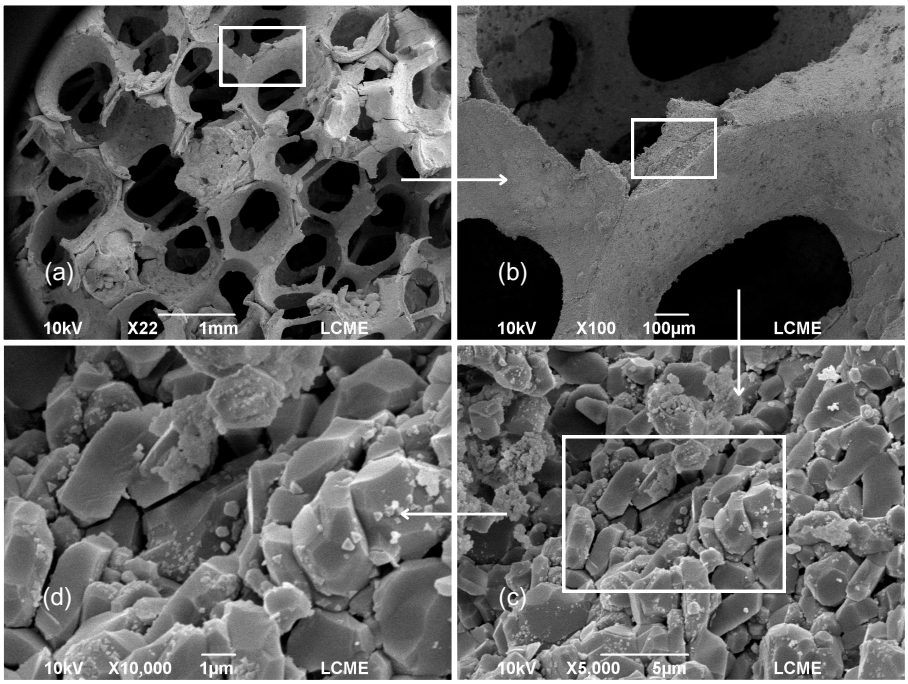

Source: Developed by the author (2023).

Figure 18 and 19 provided a visual examination that, despite the washcoat layer and sequential impregnations of nickel, copper, and platinum, the monolith shows no apparent clogging of the pores. Furthermore, visually the quantity of macromolecules increased with each successive impregnation layer. Particles with approximate sizes of 125 nm were observable.

Figure 18 – SEM of Ni-Cu/Al_2O_3 monoliths at (a) x100, (b) x5,000, (c) x10,000, and (d) x15,000 magnifications.

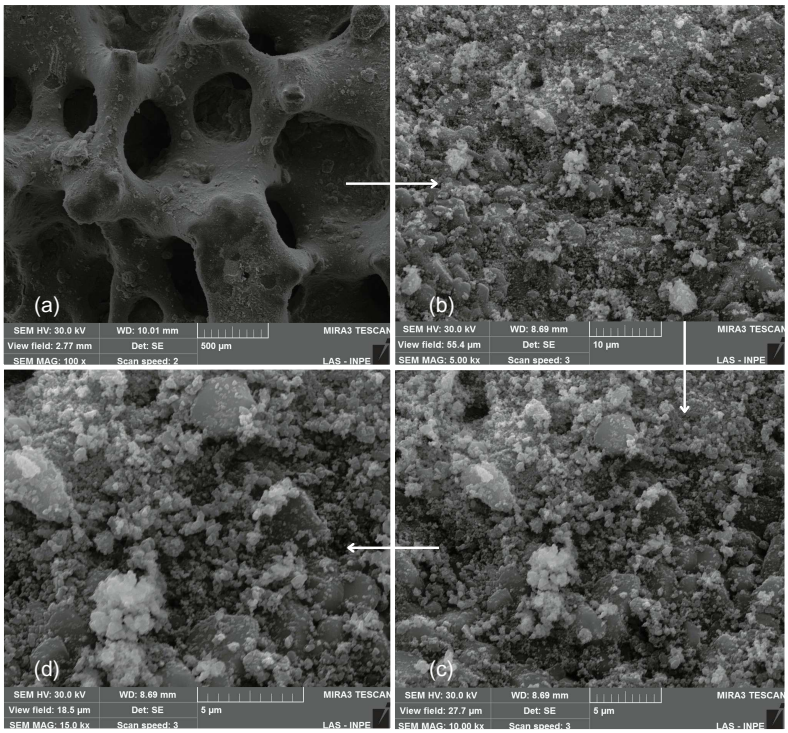

Source: Developed by the author (2023).

Figure 19 – SEM of Ni-Cu-Pt/Al_2O_3 monoliths at (a) x22, (b) x100, (c) x5,000, and (d) x10,000 magnifications.

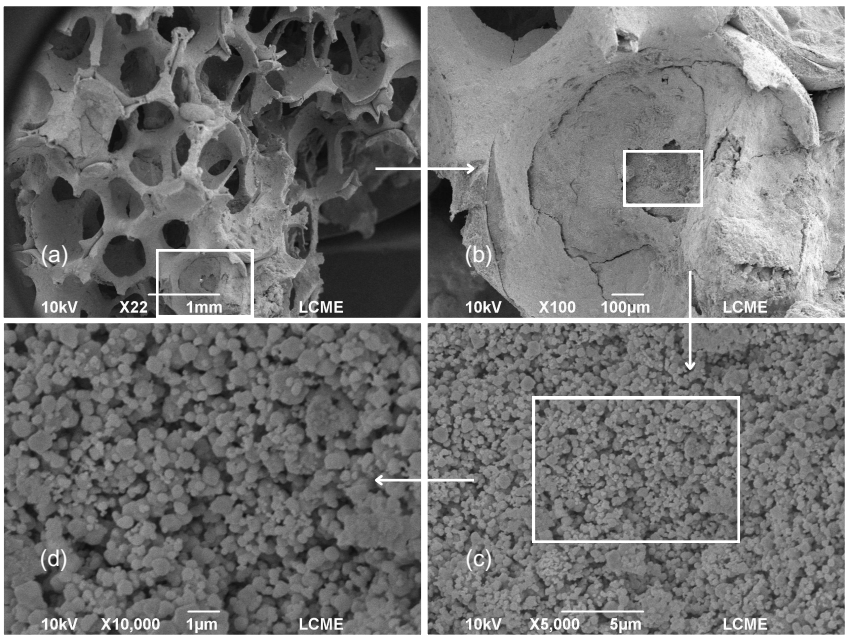

Source: Developed by the author (2023).

During the SEM analyses, the structure depicted in Figure 20 was encountered. At that moment, the unshaped structure was something new, it was merely observed as a distinctive structure compared to all those previously visualized SEM images. Subsequent research revealed that it corresponded to a *flower-like* structure.

Nik Zaiman and Shaari (2023) and Bhosale et al. (2020) conducted a review on this *flower-like* structure. According to their findings, this type of structure have a much larger surface area than spherical particles, because it was possible to load more metal particles onto the surface of the several petals, it could enhance the efficiency of surface-based interactions. Another advantage, according to the authors, was the ability to modify the size and shape of the *flower-like* structure to manipulate structural stability and the efficiency of surface activity. Yet, the combination of surface chemistry and morphology could result in functional and specific surface properties. In these reviews, various *flower-like* structures were demonstrated; however, none of them matched the structure found in this dissertation. All this prompts further investigation into its potential catalytic behavior. This finding is a milestone in unraveling the characteristics of the trimetallic catalyst, setting the stage for future studies and applications in catalytic processes. Further experimental studies are needed to elucidate the synthesis process of this structure and assess its repeatability.

Figure 20 – SEM of Ni-Cu-Pt/Al_2O_3 monolith *flower-like* structure at (a) x500, (b) x2,000, (c) x1,000, and (d) x4,000 magnifications.

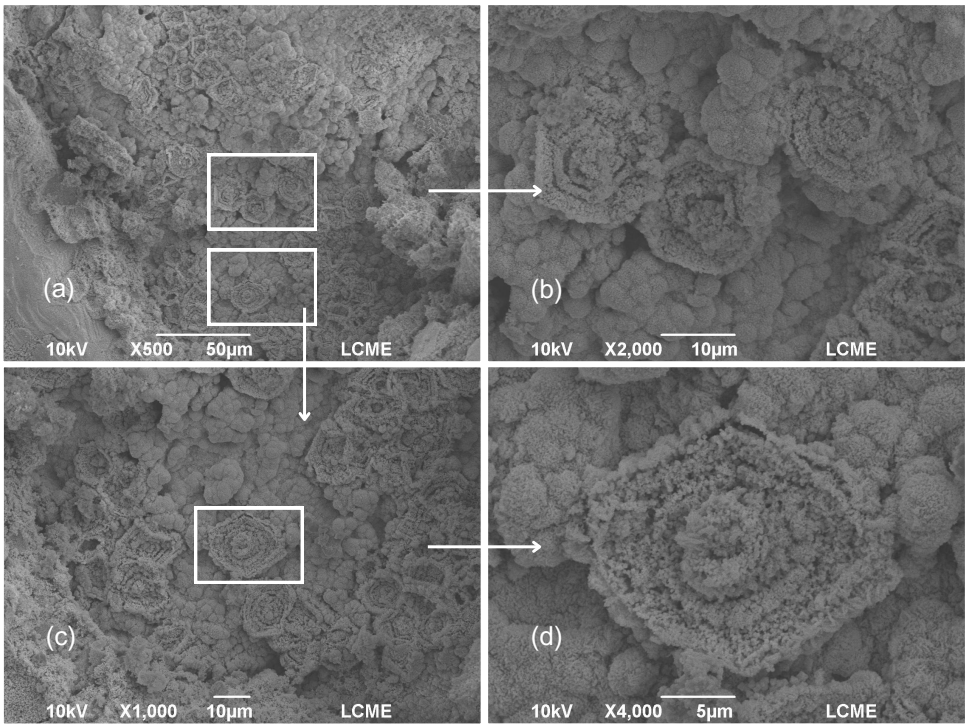

Source: Developed by the author (2023).

In Figure 21a the EDS analysis of the washcoated sample, confirms the predominant presence of alumina, validating the purity of the substrate. Moving to Figure 21b the EDS of the Ni/Al_2O_3 sample, alumina and nickel is observed. In Figure 21c the Ni-Cu/Al_2O_3 EDS results reveal the presence of alumina, nickel, and copper in relatively lower concentrations, as anticipated due to the low copper additions in the material. However, in Figure 21d the EDS analysis of the Ni-Cu-Pt/Al_2O_3 sample identifies only alumina and nickel.

One reason why the EDS did not capture the presence of platinum in the sample may be attributed to the use of a single-point EDS analysis instead of elemental mapping. Single-point EDS involves analyzing a specific spot on the sample, providing a localized elemental profile. While this approach offers high precision, it has its limitations. In our case, the absence of copper and platinum in the EDS analysis of the Ni-Cu-Pt/Al_2O_3 sample can be attributed to the specific point chosen for analysis. Since copper and platinum were added in low quantities, there may be spots in the sample where they do not appear. In contrast, elemental mapping visualizes the distribution of constituent elements in the specimen two-dimensionally displaying the characteristic X-ray intensities or concentrations of the elements in an area, offering a more comprehensive view.

In the images obtained from the EDS, it has a unidentifiable peak at 0 keV, Newbury (2009) explain that probabily is caused by the inherent noise in the electronic components of the detector when the photon energy is reduced leading to the appearance of noise peaks.

Figure 21 – EDS images of the samples.

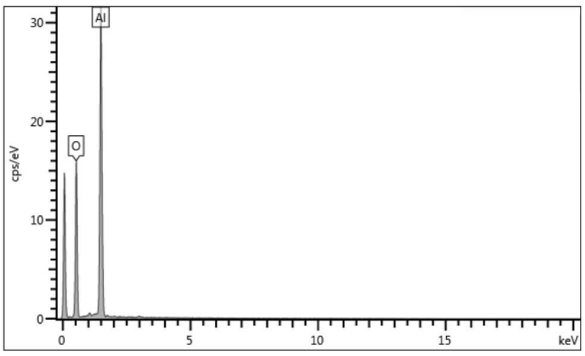

(a) EDS image of Al_2O_3 sample.

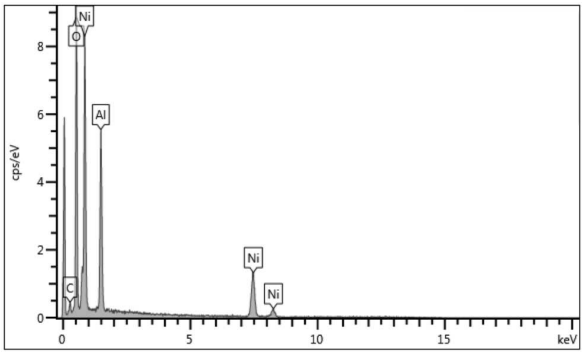

(b) EDS image of Ni/Al_2O_3 sample.

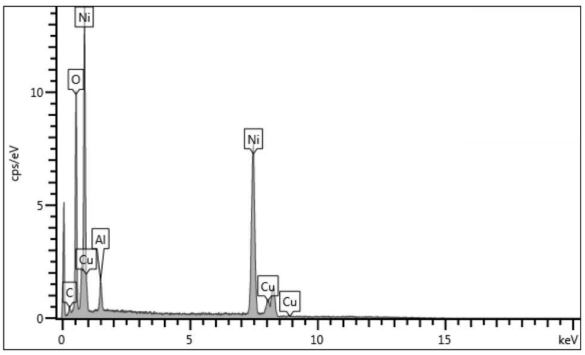

(c) EDS image of $Ni\text{-}Cu/Al_2O_3$ sample.

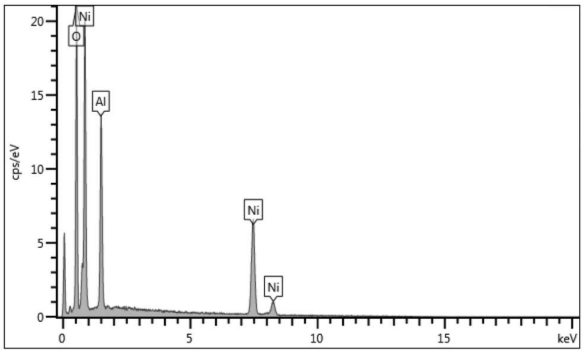

(d) EDS image of $Ni\text{-}Cu\text{-}Pt/Al_2O_3$ sample.

Source: Developed by the author (2023).

4.3.3 X-Ray Photoelectron Spectroscopy

XPS showed the chemical compositions of the sample. The atomic percentage of each orbital was presented in Table 10. This provided a quantitative insight into the elemental distribution and electronic states of the sample. It was crucial to emphasize that the atomic percentage differd from the mass percentage and is specifically applicable to the surface composition material.

Examining Table 10 provided a comprehensive understanding of surface chemistry. Al_2O_3 sample exhibited a high percentage of oxygen (O1s), indicating a surface predominantly composed of aluminum oxides. In contrast, As Ni, Cu, and Pt are introduced into the Al_2O_3 matrix, there was a noticeable decrease in oxygen percentages compared to alumina, and an increase in percentages of orbitals related to these metals. This implied the incorporation and interactions of these metals on the surface.

It is noteworthy that all samples had a considerable percentage of carbon (C1s). The significant presence of carbon adsorbed or incorporated on the surface of the sample suggests the presence of adventitious carbon. This phenomenon is common in surface analysis techniques such as XPS due to the technique's sensitivity to atmospheric contaminants and sample handling. Adventitious carbon refers to carbon that is not intrinsic to the sample's composition but is instead deposited on the surface

during sample preparation or exposure to the experimental environment. This carbon can originate from organic residues in the laboratory environment, vacuum pump oils, sample handling, or other surface contaminants (GREY; NIE; BIESINGER, 2024).

The presence of copper and platinum were identified in samples containing these metals. It confirmed the presence of these two metals in the Ni-Cu-Pt/Al_2O_3 final catalyst, even if their presence might not have been evident in other characterization techniques. This insight underscores the importance of employing multiple analytical methods to obtain a comprehensive understanding of the composition and characteristics of the materials under investigation.

Table 10 – XPS atomic percentage on the surface.

Samples	**Orbital**					
	O1s	**C1s**	**Al2p**	**Ni2p**	**Cu2p**	**Pt4d**
Al_2O_3	41.1%	28.8%	30.1%	-	-	-
Ni/Al_2O_3	26.6%	20.9%	39.7%	12.8%	-	-
Ni-Cu/Al_2O_3	24.7%	18.5%	46.4%	8.3%	2.1%	-
Ni-Cu-Pt/Al_2O_3	10.9%	33.5%	44.1%	8.8%	1.1%	1.6%

The ASFs used for calculation purposes were: C=0.205; O=0.63; Al=0.11; Ni=5.4; Cu=4.3; Pt=1.92 (WAGNER et al., 1979, 1982).
Source: Developed by the author (2023).

The XPS results illustrated in Figure 22 revealed that the incorporation of metals induced electronic states near to zero Fermi energy indicating a transition towards a more metallic character in the catalyst. Specifically, the sample devoid of any added metal displayed a Fermi energy at 2.6 eV, a considerable distance from the zero Fermi energy. This observation was indicative of an insulating surface, highlighting the influence of metal insertion on the overall electronic behavior of the catalyst. Despite the absence of metals in metallic form in the orbital regions, the sample was partially metalized, as surface metalization is identified when the Fermi level is near zero. This phenomenon was crucial in the context of catalysis, as it implied improved electron transfer properties and enhanced catalytic activity.

Figure 22 – Fermi energy (FE) of (a) Al_2O_3, (b) Ni/Al_2O_3, (c) $Ni\text{-}Cu/Al_2O_3$, and (d) $Ni\text{-}Cu\text{-}Pt/Al_2O_3$ samples.

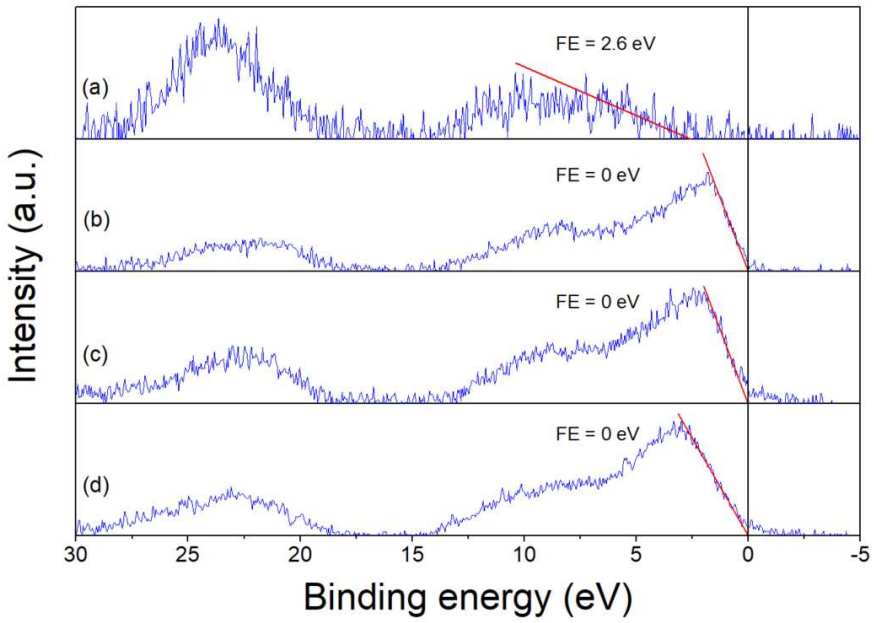

Source: Developed by the author (2023).

In Figures 23 and 24, the spectrum Ni2p and Cu2p of the $Ni\text{-}Cu/Al_2O_3$ sample were evident, and all samples exhibited similarity. The consistency in the spectra suggests that the electronic characteristics of the nickel and copper component remained relatively unaffected by the presence of each other's metals. The Ni2p spectrum was decomposed into twelve partial peaks, with six in each spin-orbit region. The peaks in the $2p_{3/2}$ region were associated with the compounds NiO, $Ni(OH)_2$, and NiOOH. The first two oxides corresponded to the Ni^{2+} oxidation state, with peaks located at 856.8 eV and 858.9 eV. The third oxide corresponded to the Ni^{3+} oxidation state (high oxidation) with peak located at 854.9 eV. The same compounds are also represented in the $2p_{1/2}$ region by the last three peaks located at 872.3 eV, 873.9 eV and 875.9 eV. The others represented satellites located at 861.4 eV, 863.2 eV and 865.4 eV in the $2p_{3/2}$ region and located at 878.5 eV, 881.0 eV and 883.5 eV in the $2p_{1/2}$ region (MELLO DOS SANTOS et al., 2022).

In Figure 24 the Cu2p spectrum was decomposed into six partial peaks, with two in each spin-orbit region, and the two in the meadle peaks been the satellites ones. The $2p_{3/2}$ region with peaks located at 933.9 eV and 936.0 eV are associated with Cu^{1+} and Cu^{2+} states respectively, both related to CuO. The Cu^{1+} state was more catalytic (less oxidized state). The same compound was also represented in the $2p_{1/2}$ region by the peaks 953.6 eV (Cu^{1+}) and 955.7 eV (Cu^{2+}). The satellite peaks were located at 941.3 eV and 944.3 eV (SUN et al., 2019).

Figure 23 – Ni2p orbital spectrum.

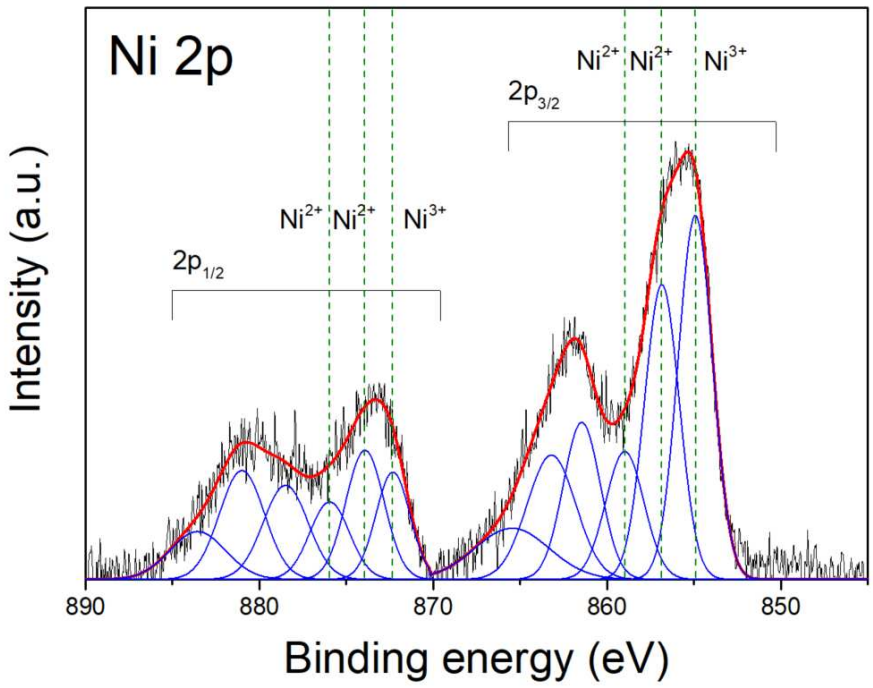

Source: Developed by the author (2023).

Figure 24 – Cu2p orbital spectrum.

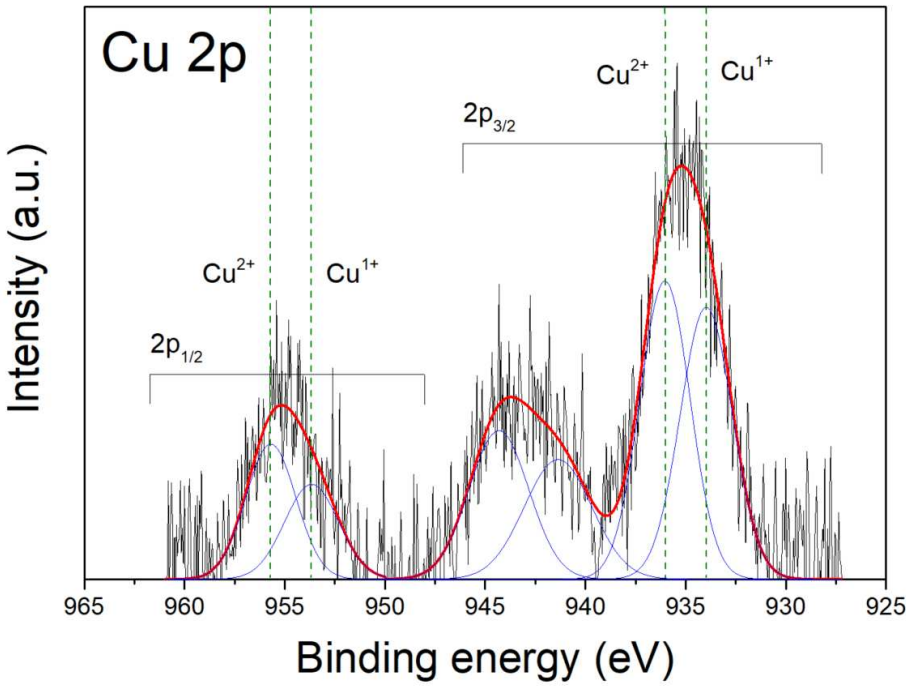

Source: Developed by the author (2023).

In Figure 25 the Pt4d spectrum was decomposed into four partial peaks, with two in each spin-orbit region. The peaks in the $4p_{5/2}$ region located at 316.9 eV and 319.7 eV were associated with the compounds PtO and PtO_2 respectively. The first oxide corresponded to the Pt^{2+} (more catalytic state, carrying less oxidation) while the second compound corresponded to the Pt^{4+} oxidation state. The same compounds were also represented in the $4d_{3/2}$ region by the peaks 333.6 eV and 337.4 eV. Notably, no satellite peaks were found in the platinum sample (YANG; CHEN, Z.; GONG, 2023).

Figure 25 – Pt4d orbital spectrum.

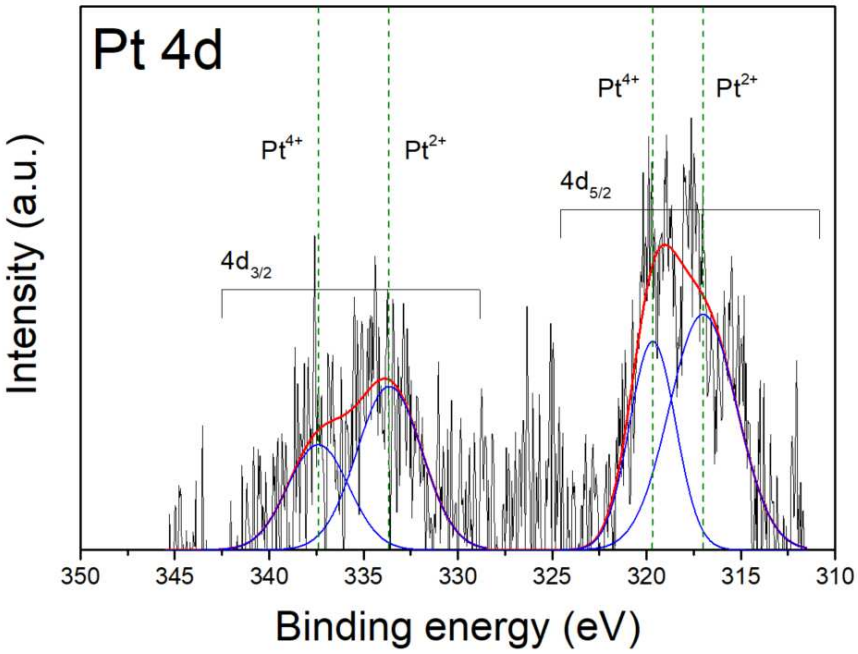

Source: Developed by the author (2023).

The uniformity observed in spectras across different samples underscored a consistent electronic structure, despite variations in the overall catalyst composition.

4.3.4 Temperature Programmed Reduction

The peaks of the TPR analyses indicate the temperature at which the reduction of metal oxide occurs. With the increase in temperature, the reduction rate exhibits exponential growth, reaching its maximum before gradually decreasing towards the end of the process when the entire oxide has been fully reduced. The same mass was used for all TPR analyses. TPR results shown in Figure 26 the homogeneity of Ni and Ni-Cu-Pt/Al_2O_3 samples, indicated by similar peak heights in the Int and Ext regions of the monoliths.

Figure 26 – TPR of (a) Ni/Al_2O_3 Int, (b) Ni/Al_2O_3 Ext, (c) Ni-Cu-Pt/Al_2O_3 Int, and (d) Ni-Cu-Pt/Al_2O_3 Ext samples.

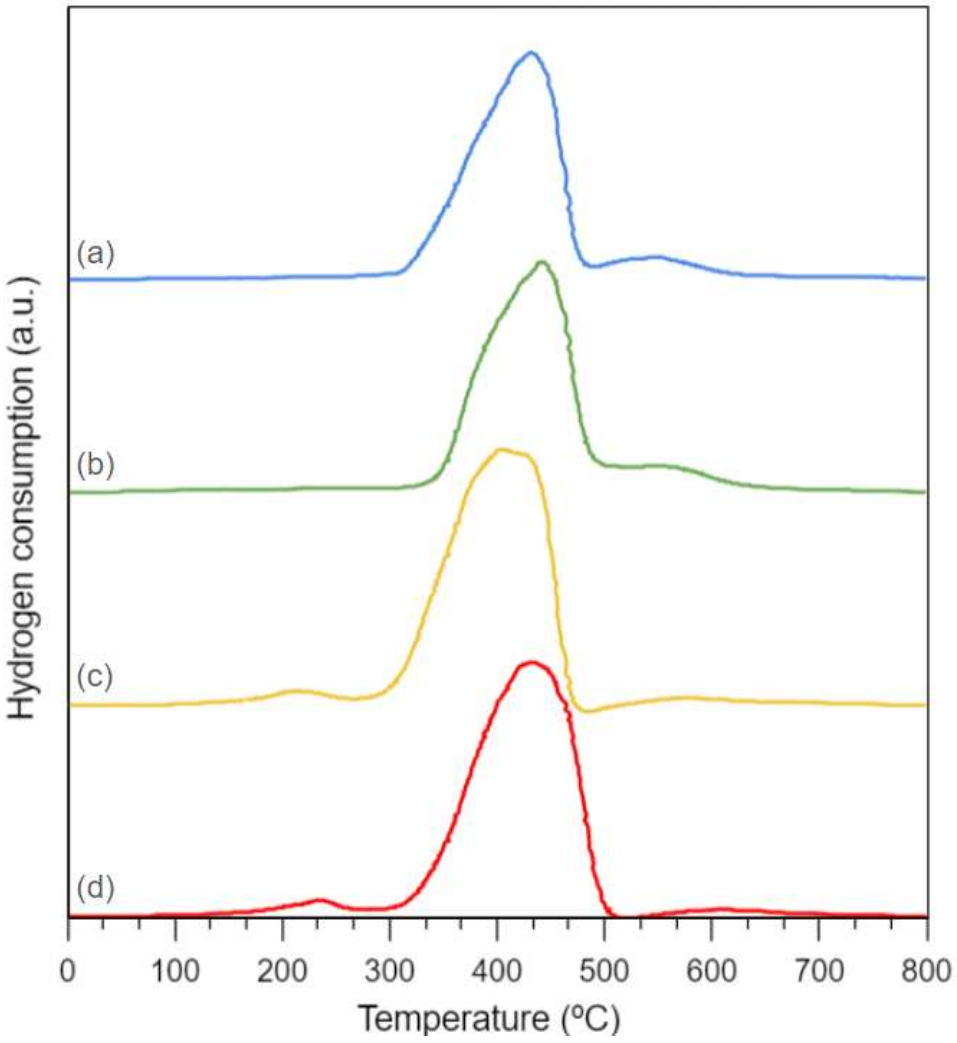

Source: Developed by the author (2023).

The results also reveal that for both Ni Int and Ni Ext samples exhibited two distinct peaks. The first peak was observed in the temperature range of 300 to 500 ℃, suggesting the reduction of nickel oxide and indicating a high thermal activity of the catalyst in this range. The second peak emerged between 500 and 600 ℃, also attributed to the reduction of nickel oxide. The fact that this peak was smaller suggested that a relatively small portion of NiO species interacted strongly with the support. These findings align with observations made by Dasari et al. (2011), who presented an image illustrating that the reduction peaks of the Ni catalyst showed a larger peak at 433 ℃ and a smaller one at 568 ℃, consistent with our results. Additionally, Jehng and C.-M. Chen (2001) contributed to this understanding, stating that TPR studies of Ni/Al_2O_3 catalysts with nickel loading below approximately 15% indicated the formation of surface nickel species on the Al_2O_3 surface, displaying a reduction peak at 560 to 590 ℃. This

observation aligned well with the results, considering that the metal loading in the samples with nickel was approximatly 10% Ni.

In the investigation of the trimetallic Ni-Cu-Pt/Al_2O_3 catalyst for ethanol reforming, TPR analysis revealed distinctive peaks at three temperatures ranges: 150 to 250 ℃, 300 to 500 ℃, and a minor range at 500 to 650 ℃. Notably, Ni-Cu-Pt/Al_2O_3 samples exhibited higher peaks than the Ni samples in the 300 to 500 ℃ range indicating the reduction of nickel oxide but also pointing towards the reduction of copper. According to Mozer (2005), the 1%Cu/Al_2O_3 catalyst displayed H_2 consumption peaks at 480 and 640 ℃. The low-temperature peak was assigned to the reduction of isolated Cu^{2+} to Cu^{1+} and CuO to Cu^0, while the high-temperature peak was attributed to the reduction of Cu^{1+} ions to Cu^0 (TORRE-ABREU et al., 1997).

Mozer (2005) also reported a characteristic peak at around 250 ℃, indicative of the reduction profile of [PtO_xCl_y]s, suggesting the presence of platinum species. Furthermore, the Pt-Cu/Al_2O_3 catalyst, as Mozer (2005), exhibited a H_2 consumption peak at 280 ℃, corresponding to the reduction of PtO_xCl_y species. The H_2 consumption in the range of 300 to 500 ℃ was associated with the reduction of CuO, which was not interacting with platinum.

Interestingly, Ni-Cu-Pt/Al_2O_3 Int and Ni-Cu-Pt/Al_2O_3 Ext catalysts displayed the Pt peak at approximately 200 ℃ and 230 ℃, respectively. These variations in peak temperatures suggest the influence of catalyst composition on the reduction process. According to Schmal (2011), the peak displacement towards lower temperatures in the Ni-Cu-Pt/Al_2O_3 Int sample, can be attributed to weaker interaction between the catalyst and other materias. This phenomenon could be justified because of the reduced concentration of the impregnated metals in the inner regions of the foam.

4.4 CATALYTIC TESTS FOR ETHANOL AUTOTHERMAL REFORMING

In this section, the results of the catalytic tests for ethanol autothermal reforming were presented and analyzed. The emphasis was placed on elucidating the performance of the selected catalysts under various experimental conditions, including variations in temperature and WHSV. Each set of conditions was examined to identify optimal operating parameters, and assess the catalysts efficiency in promoting the desired reforming reactions. This section aimed to offer a comprehensive and insightful exploration of the experimental results, setting the stage for a thorough analysis and interpretation of the catalytic performance.

4.4.1 Gas chromatography

The results of the gas chromatography analyses were detailed in the subsequent sections. These sections presented and discussed the chromatography data

obtained from the samples providing the separation and identification of the individual components in the reformed gases thus serving as a fundamental tool for the comprehensive characterization of the samples under investigation. The gas chromatography results were analyzed to provide insights into the composition and characteristics of the analyzed substances. The subsequent chapters aimed to offer a thorough exploration and interpretation of the gas chromatography findings, contributing to a more comprehensive understanding of the studied catalysts.

4.4.1.1 Conversion and Selectivity

In this study, we investigated the performance of two catalysts: a nickel catalyst and a trimetallic catalyst in the ethanol reforming process. The trimetallic catalyst was tested at two different WHSV values. Experiments were conducted over a range of temperatures. The results of the reforming tests are presented in Tables 11, 12 and 13, along with Figures 27, 28 and 29, illustrating the output percentage results of each gas captured by the chromatograph. Additionally, Figure 30 shows the outcomes of ethanol conversion on the studied catalysts. The sampled values represent the averages of tests conducted at the specified temperatures and the results are discussed below.

Table 11 – Catalytic performance of Ni/Al_2O_3 catalyst at WHSV of 13.5 h^{-1}.

T (°C)	$\mathbf{X}_{C_2H_5OH}$ **(%)**	$\mathbf{S}_{C_3H_6O}$ **(%)**	$\mathbf{S}_{C_2H_4O}$ **(%)**	$\mathbf{S}_{C_2H_4}$ **(%)**	$\mathbf{S}_{CH_4}$ **(%)**	$\mathbf{S}_{CO_2}$ **(%)**	$\mathbf{S}_{CO}$ **(%)**	$\mathbf{S}_{H_2}$ **(%)**
400	1.12	0.12	94.13	0.05	0.00	1.53	0.00	4.18
500	74.54	0.02	40.96	0.02	0.00	0.18	3.49	39.33
600	84.73	0.09	41.08	0.45	0.00	0.07	10.670	47.64
700	97.44	0.05	24.91	1.69	0.00	0.14	23.93	49.27

Source: Developed by the author (2023).

Figure 27 – Composition of the products reactions of Ni/Al_2O_3 catalyst at WHSV of 13.5 h^{-1}.

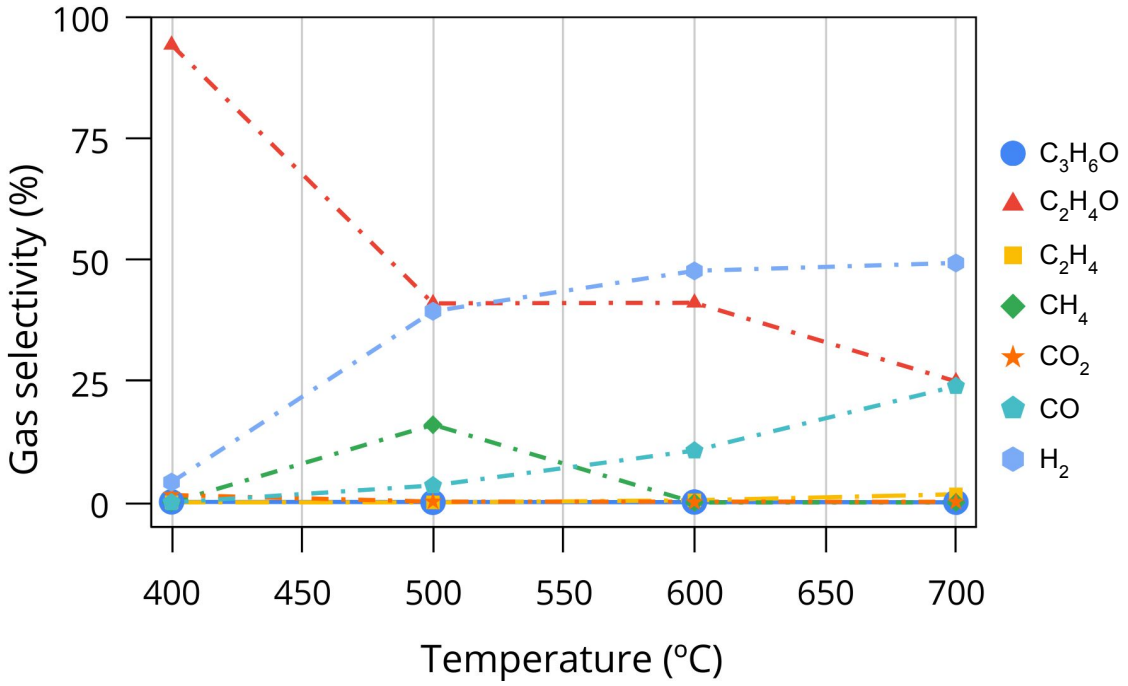

Source: Developed by the author (2023).

Table 12 – Catalytic performance of $Ni\text{-}Cu\text{-}Pt/Al_2O_3$ catalyst at WHSV of 13.5 h^{-1}.

T (°C)	$X_{C_2H_5OH}$ (%)	$S_{C_3H_6O}$ (%)	$S_{C_2H_4O}$ (%)	$S_{C_2H_4}$ (%)	S_{CH_4} (%)	S_{CO_2} (%)	S_{CO} (%)	S_{H_2} (%)
400	2.86	0.05	95.80	0.01	0.00	0.75	1.74	1.64
450	55.21	0.04	89.50	0.02	0.00	2.29	2.56	5.59
500	66.38	0.01	71.83	0.02	0.00	2.52	3.72	21.89
550	73.91	0.01	69.73	0.05	0.00	1.54	5.73	22.95
600	82.50	0.05	69.16	0.10	0.00	0.93	5.37	24.40
650	87.70	0.02	67.92	0.00	0.00	0.95	6.83	24.27
700	89.58	0.04	60.57	0.30	0.00	1.14	9.94	28.02

Source: Developed by the author (2023).

Figure 28 – Composition of the products reactions of Ni-Cu-Pt/Al_2O_3 catalyst at WHSV of 13.5 h^{-1}.

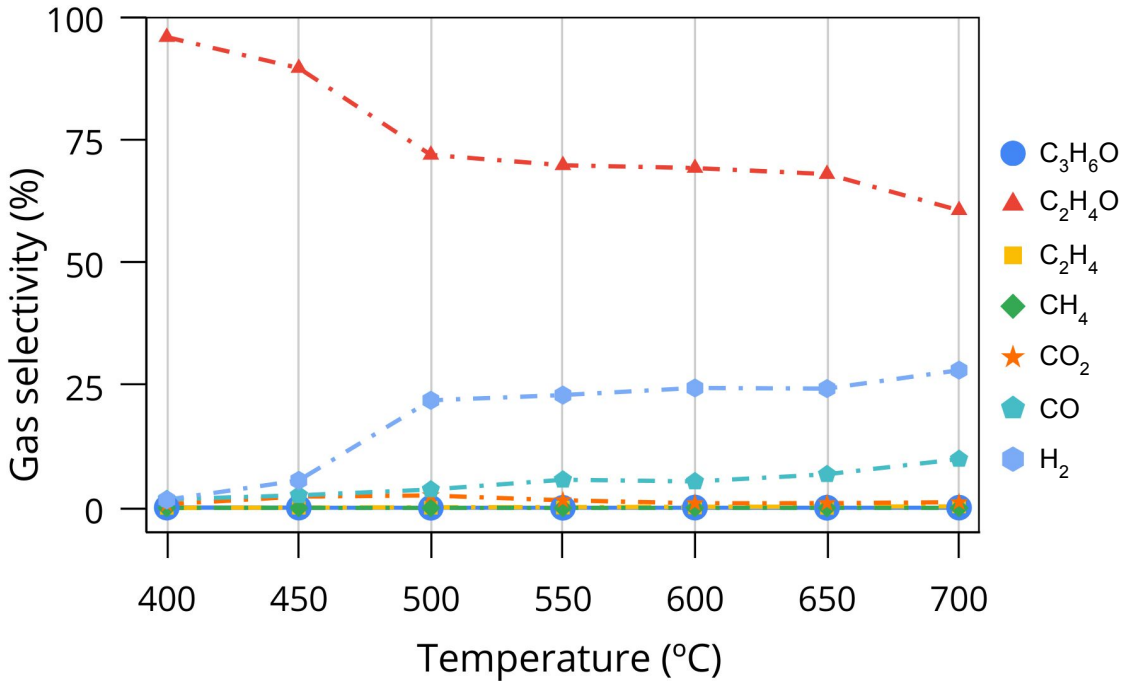

Source: Developed by the author (2023).

Table 13 – Catalytic performance of Ni-Cu-Pt/Al_2O_3 catalyst at WHSV of 9 h^{-1}.

T (°C)	$X_{C_2H_5OH}$ (%)	$S_{C_3H_6O}$ (%)	$S_{C_2H_4O}$ (%)	$S_{C_2H_4}$ (%)	S_{CH_4} (%)	S_{CO_2} (%)	S_{CO} (%)	S_{H_2} (%)
400	29.12	0.07	98.69	0.02	0.00	0.43	0.00	0.79
450	56.60	0.02	65.88	0.02	13.25	4.78	3.04	13.01
500	67.77	0.01	61.13	0.02	0.00	4.53	4.77	29.54
550	77.31	0.17	67.03	0.10	0.00	1.02	6.78	24.91
600	81.74	0.02	67.83	0.09	0.00	1.05	6.24	24.78
650	82.50	0.06	62.37	0.14	0.00	1.08	8.89	27.45
700	85.52	0.00	45.75	0.39	0.00	1.53	15.35	36.98

Source: Developed by the author (2023).

Figure 29 – Composition of the products reactions of Ni-Cu-Pt/Al_2O_3 catalyst at WHSV of 9 h^{-1}.

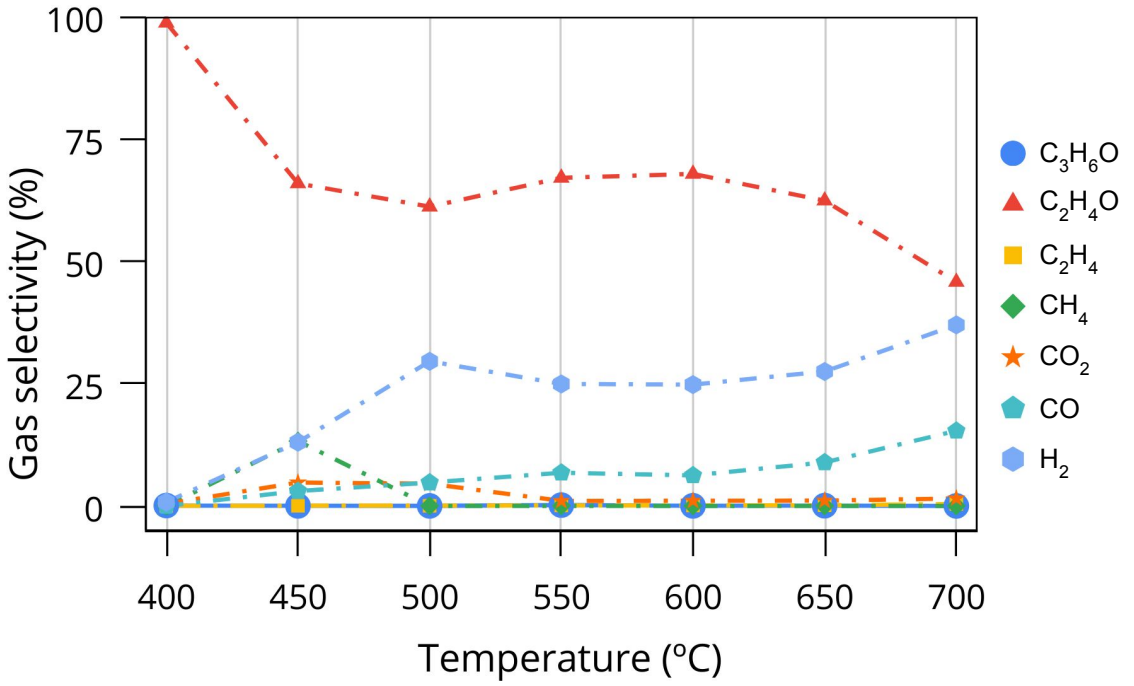

Source: Developed by the author (2023).

Figure 30 – Ethanol conversion of tested samples.

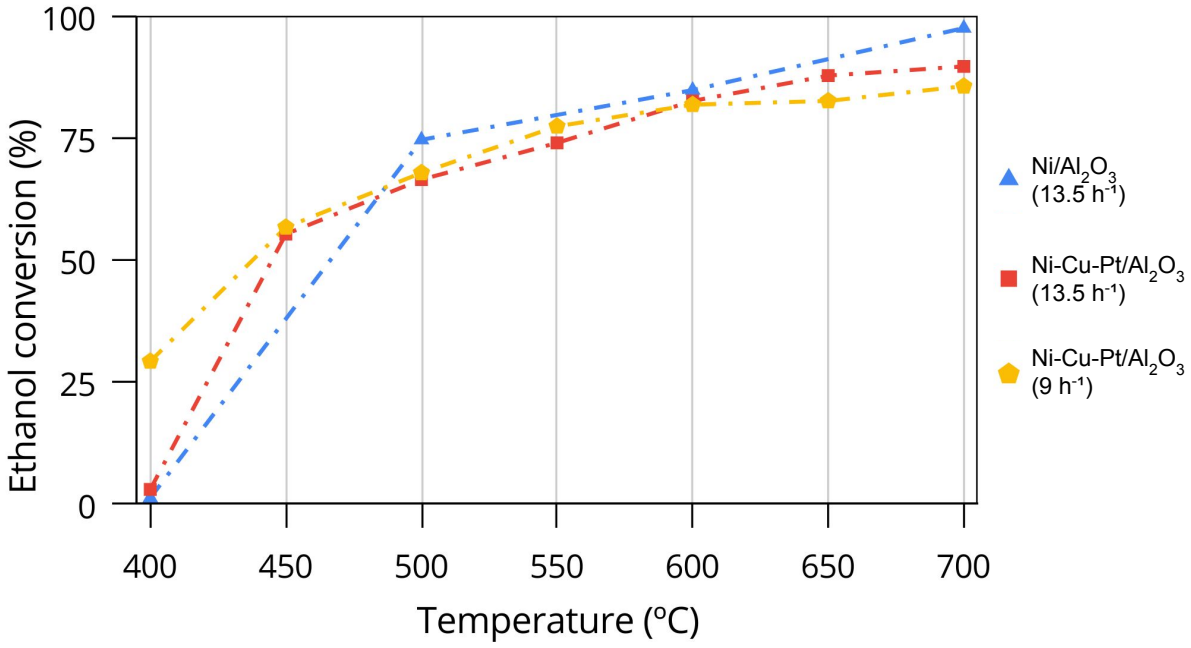

Source: Developed by the author (2023).

From these results, the trimetallic catalysts demonstrated a significant reduction in activation temperature compared to the monometallic nickel catalyst. Furthermore, it was observed that trimetallic catalyst with a WHSV of 9 h^{-1} was what reduced the activation temperature the most. However, despite achieving higher conversion rates, the trimetallic catalyst showed lower selectivity for ethanol compared to the nickel catalyst. As the temperature increased, the nickel catalyst consistently outperformed the trimetallic catalyst in terms of ethanol conversion. This suggests that, at elevated temperatures, the nickel catalyst becomes more effective in promoting the reforming reaction. Regarding hydrogen selectivity, the trimetallic catalyst with a lower WHSV demonstrated better selectivity as the temperature increased compared to the trimetallic catalyst with a higher WHSV. Nevertheless, both trimetallic catalyst samples exhibited lower hydrogen selectivity than the nickel catalyst.

Both catalysts demonstrated very low CO_2 emissions regardless of the temperature, with a trend indicating that emissions decreased with rising temperature. Interestingly, with the increase in temperature, CO emissions increased, with the trimetallic catalyst emitting less CO than the nickel catalyst.

Contrary to expectations, the nickel catalyst when supplemented with copper and platinum did not demonstrate an improved ability to break the C-C bonds and increase selectivity for hydrogen. This failure to enhance catalytic activity in C-C bond breaking could be attributed to the insufficient quantities of copper and platinum incorporated into the nickel catalyst. The low concentrations of these metals may not have been adequate to significantly impact the reaction mechanisms involved in C-C bond cleavage during ATR. Consequently, the catalytic activity of the trimetallic catalyst might have been compromised, resulting in observed difficulties in breaking the C-C bonds. Additionally, successive impregnations could potentially reduce catalyst efficiency. With each consecutive impregnation increases the risk of material accumulation, consequently reducing the accessible surface area for catalytic activity. Moreover, uneven distribution of components may occur, resulting in inconsistent catalytic activity.

Although the chromatogram indicated methane emissions in a few results, it is believed to be a chromatographic error, as methane emissions were observed in only two of the numerous test results. Acetaldehyde was the most detected compound by the chromatograph, with concentrations decreasing significantly with increasing temperature. For the nickel sample, there was an almost 75% reduction, nearly 40% for the trimetallic catalyst with higher WHSV, and approximately 55% for the trimetallic catalyst with lower WHSV.

5 CONCLUSION

In this dissertation, the synthesis and characterization of an 80mm diameter monolith of Ni/Al_2O_3 and Ni-Cu-Pt/Al_2O_3 were conducted for the autothermal reforming of ethanol into hydrogen. The monolith underwent various characterizations and reforming reactions tests.

In conclusion, the extensive exploration of trimetallic catalysts for ethanol reforming has yielded valuable insights into their composition, morphology, and thermal behavior. The C(%), averaging 18.98% with a standard deviation of 1.32%, the M_{Ni}(%), averaging 9.62%, with a standard deviation of 0.24% and M_{Cu}(%), averaging 0.52%, with a standard deviation of 0.02% demonstrates a successful washcoat and impregnation process with uniform distribution. Due to nitric acid corrosive nature minimal to no mass gain was justified in platinum impregnation.

XRD patterns unveiled the presence of cubic-NiO in nickel-containing samples. The low concentrations of copper and platinum used in the samples syntesis caused their peaks to be very small or undetectable on XRD. SEM images offered a comprehensive examination, confirming successful washcoat application and impregnation processes. The observation of a distinctive *flower-like* structure marked a significant milestone, prompting further investigation into its catalytic behavior. The disparity in scale between SEM and XRD could happen because SEM offered a macroscopic view, gaving insight into the potential agglomeration of crystallites, while XRD provided an atomic-scale perspective, potentially revealing smaller crystallite sizes than SEM. EDS analysis confirmed concentrations of alumina, nickel and copper with none platinum identification. Limitations of single-point EDS analysis were acknowledged, emphasizing the potential of elemental mapping for a comprehensive understanding. XPS analysis revealed significant insights into the composition and electronic structures of both Al_2O_3 and Ni-Cu-Pt/Al_2O_3 samples. The detection of carbon (C1s) in both samples suggested the adsorption or incorporation of carbon-based compounds on the surface. Moreover, the successful incorporation of Ni, Cu, and Pt into the Al_2O_3 matrix was evidenced by a shift in elemental percentages, highlighting the introduction of metallic atoms onto the catalyst's surface. Consistent electronic structures were observed across different samples. The decomposition of Ni2p, Cu2p, and Pt4d spectra provided information about the oxidation states of these metals on the catalyst's surface. Notably, XPS successfully identified copper and platinum in the Ni-Cu-Pt/Al_2O_3 catalyst, even when not apparent in other characterization techniques. TPR analyses highlighted the homogeneity of Ni and Ni-Cu-Pt samples, with distinctive peaks in the Ni-Cu-Pt catalyst indicating the present of copper and platinum.

The reform tests successfully demonstrated the efficacy of the trimetallic catalyst in lowering the temperature required for ethanol reforming. However, it was ob-

served a reduction of almost 20 ℃ in the activation temperature when compared to the monometallic nickel catalyst. Although the conversion of ethanol took place at low temperatures, the selectivity was still better on the nickel catalyst, even though it did not convert as much. The reform tests indicated that the nickel catalyst tested at 700 ℃ temperature achieved a near complete conversion, and almost 50% selectivity to hydrogen. It could be identified that the evaporation region is an important part of the auto thermal reformer even as temperature control and preheating. To obtain more accurate results more numbers of conversion tests with the monolith at each temperature must be performed.

In summary, synthesis, characterization, and reforming tests provide a foundation for future studies and applications. Unique findings, such as the *flower-like* structure in the trimetallic catalysts, open avenues for further exploration and catalyst design optimization.

6 RECOMMENDATIONS FOR FUTURE WORK

- Replace α-Al_2O_3 with γ-Al_2O_3 for improved catalysis;

For future catalyst development, utilizing γ-Al_2O_3 as a catalyst support material is recommended over α-Al_2O_3. Exploring γ-Al_2O_3 as a catalyst support promises enhanced catalysis. However, γ-Al_2O_3 has intrinsic acidity, which can promote ethanol dehydration into ethylene and carbon deposition on the catalyst. To mitigate this issue and enhance catalyst performance, an effective approach is the addition of alkali metals to neutralize the inherent acidity of γ-Al_2O_3. Studies conducted by Mariño et al. (2001) and Vizcaíno et al. (2008) have demonstrated the efficacy of incorporating potassium (K) and magnesium (Mg) into γ-Al_2O_3 to neutralize acidic sites. Their research has shown a substantial reduction in coke formation as a result of modifying γ-Al_2O_3 with alkali metals, ultimately leading to improved overall catalyst performance.

- Use analytical techniques for coke deposit analysis;

To study the generation of coke deposits, Temperature Programmed Oxidation (TPO), Thermogravimetric Analysis (TGA) and Differential Scanning Calorimetry (DSC) are valuable techniques for characterizing the quantity and nature of coke deposits that accumulate during catalytic reactions. This is essential for optimizing the long-term performance of the catalyst.

- Conduct long-term reactions for properties assessment;

Performing long-term reactions on a catalyst serves to evaluate catalytic stability, identification of poisoning effects, track degradation, and validation of real-world effectiveness. Long-term tests help determine if a catalyst maintains its activity over time, ensuring its reliability in industrial applications where long-term stability is crucial.

- Zeta potential analysis for dispersion stability;

For future studies, it is recommended to conduct an analysis of zeta potential to refine analysis techniques and explore the influence of component addition sequences. Specifically, a systematic exploration of alumina dispersion could involve starting with water and acid until reaching a pH of 4, followed by the addition of alumina while controlling the pH. This approach, whether excluding or including sodium silicate, could provide a more stable dispersion of the alumina slurry.

- SEM characterization for investigation of *flower-like* format.

During SEM analyses of the Ni-Cu-Pt catalyst sample, a distinctive morphology emerged. researchers has explored similar morphology referred to as *flower-like* structure. Despite the literature searches, no specific article detailing the synthesis of an identical *flower-like* structure was uncovered. This disparity underscores the need for a meticulous exploration of the catalyst's synthesis conditions and the role of each component. Future investigations should focus on elucidating the factors influencing

the formation of this distinct morphology to unlock new avenues for optimizing ethanol reforming catalysts and advancing the field towards more efficient and sustainable processes.

REFERENCES

AASBERG-PETERSEN, K.; CHRISTENSEN, T.S.; DYBKJR, I.; SEHESTED, J.; ØSTBERG, Martin; COERTZEN, R.M.; KEYSER, M.J.; STEYNBERG, A.P. Chapter 4 Synthesis gas production for FT synthesis. **Studies in Surface Science and Catalysis**, v. 152, p. 258–405, Dec. 2004.

AGENCY, International Energy. **World Energy Outlook 2022**. [S.l.: s.n.], 2022. Available from: https://www.iea.org/reports/world-energy-outlook-2022. Visited on: 29 Aug. 2022.

AGRAFIOTIS, C.; TSETSEKOU, A. The effect of powder characteristics on washcoat quality. Part I: Alumina washcoats. **Journal of The European Ceramic Society - J EUR CERAM SOC**, v. 20, p. 815–824, June 2000.

AHMED, S.; KRUMPELT, M. Hydrogen from Hydrocarbon Fuels for Fuel Cells. **International Journal of Hydrogen Energy**, v. 26, p. 291–301, Apr. 2001.

ALMEIDA, L.; ECHAVE, F. J.; SANZ, O.; CENTENO, M.; ODRIOZOLA, J.; MONTES, M. Washcoating of metallic monoliths and microchannel reactors. **Studies in Surface Science and Catalysis**, v. 175, p. 25–33, Dec. 2010.

ARAUJO, P. H. L. Potencial de utilização de carvão ativado como suporte catalítico na decomposição de óxido nitroso (N_2O), 2006.

ASSABUMRUNGRAT, S.; LAOSIRIPOJANA, N. FUELS – HYDROGEN PRODUCTION | Autothermal Reforming. In: [s.l.: s.n.], 2009. P. 238–248. ISBN 978-0-444-52745-5.

BAER, D.; THEVUTHASAN, S. Characterization of Thin Films and Coatings. **Handbook of Deposition Technologies for Films and Coatings**, Dec. 2010.

BAHARUDIN, L.; RAHMAT, N.; OTHMAN, N.; SHAH, N.; SYED-HASSAN, S. S. A. Formation, control, and elimination of carbon on Ni-based catalyst during CO2 and CH4 conversion via dry reforming process: A review. **Journal of CO2 Utilization**, v. 61, p. 102050, July 2022.

BANÚS, E.; MILT, V.; MIRÓ, E.; ULLA, M. Co,Ba,K/ZrO_2 coated onto metallic foam (AISI 314) as a structured catalyst for soot combustion: Coating preparation and characterization. **Applied Catalysis A: General**, v. 379, p. 95–104, May 2010.

BARUAH, R.; DIXIT, M.; BASARKAR, P.; PARIKH, D.; BHARGAV, A. Advances in ethanol autothermal reforming. **Renewable and Sustainable Energy Reviews**, v. 51, p. 1345–1353, Aug. 2015.

BERREBI, G.; BERNUSSET, Ph. Making Industrial Catalysts. **Studies in Surface Science and Catalysis**, v. 1, p. 13–38, 1976.

BHOSALE, S. V.; AL KOBAISI, M.; JADHAV, R. W.; JONES, L. A. Flower-Like Superstructures: Structural Features, Applications and Future Perspectives. **The Chemical Record**, Nov. 2020.

BORISOV, S.; PODBEREZSKAYA, N. X-ray diffraction analysis: A brief history and achievements of the first century. **Journal of Structural Chemistry**, v. 53, Dec. 2012.

BRETT, D.J.L.; AGANTE, E.; BRANDON, N.P.; BRIGHTMAN, E.; BROWN, R.J.C.; MANAGE, M.; STAFFELL, I. The role of the fuel in the operation, performance and degradation of fuel cells. In: [s.l.: s.n.], 2012. P. 249–278. ISBN 978-0-85709-059-1.

BSHISH, A.; YAAKOB, Z.; BINITHA, N.; RAMAKRISHNAN, R.; EBSHISH, A. Steam-reforming of ethanol for hydrogen production. **Chemical Papers**, v. 65, p. 251–266, June 2011.

CARDENAS, A. A. B.; SERBENA, J. P. M. Synthesis and Characterization of NiO for Applications in Photoelectronics Devices. **Ciência e Engenharia de Materiais Conceitos, Fundamentos e Aplicação**, v. 1, p. 374–381, Sept. 2021.

CHIU, W. C.; HORNG, R. F.; CHOU, H. M. Hydrogen production from an ethanol reformer with energy saving approaches over various catalysts. **International Journal of Hydrogen Energy**, v. 38, p. 2760–2769, Feb. 2013.

DAROUGHEGI, R.; MESHKANI, F.; REZAEI, M. Characterization and evaluation of mesoporous high surface area promoted Ni- Al_2O_3 catalysts in CO_2 methanation. **Journal of the Energy Institute**, v. 93, n. 2, p. 482–495, 2020. ISSN 1743-9671.

DASARI, H.; YOON, C.; HAN, J.; YOON, S.; NAM, S. W.; LIM, T.-H. Catalytic Steam Reforming of Propane over Ni/LaAlO3 Catalysts: Influence of Preparation Methods and OSC on Activity and Stability. **Catalysis Letters**, v. 142, Feb. 2011.

DAVDA, R.R.; SHABAKER, J.W.; HUBER, G.; CORTRIGHT, R.D.; DUMESIC, J.A. Review of catalytic issues and process conditions for renewable hydrogen and alkanes by aqueous-phase reforming of oxygenated hydrocarbons over supported metal catalysts. **Applied Catalysis B: Environmental**, v. 56, p. 171–186, Nov. 2004.

DELMON, B.; GRANGE, P.; JACOBS, P.; PONCELET, G. **Preparation of Catalysts II, Proceedings of the Second International Symposium**. [S.l.: s.n.], 1979. P. 751.

DI GIULIANO, A.; GALLUCCI, K.; FOSCOLO, P.U.; COURSON, C. Effect of Ni precursor salts on Ni-mayenite catalysts for steam methane reforming and on Ni-CaO-mayenite materials for sorption enhanced steam methane reforming. **International Journal of Hydrogen Energy**, v. 44, Feb. 2019.

DICCIANNI, J.; LIN, Q.; DIAO, T. Mechanisms of Nickel-Catalyzed Coupling Reactions and Applications in Alkene Functionalization. **Accounts of Chemical Research**, v. 53, Apr. 2020.

ECHAVE, F. J.; SANZ, O.; MONTES, M. Washcoating of microchannel reactors with PdZnO catalyst for methanol steam reforming. **Applied Catalysis A: General**, v. 474, p. 159–167, Mar. 2014.

EMBRAPA. **Processamento de Amostras para Microscopia Eletrônica de Varredura**. [S.l.: s.n.], 2002. Available from: `https://ainfo.cnptia.embrapa.br/digital/bitstream/item/32390/1/documento-93.pdf`. Visited on: 22 Oct. 2022.

ENCYCLOPAEDIA BRITANNICA, The Editors of. **Industrial Revolution**. [S.l.: s.n.], 2021. Available from: `https://www.britannica.com/event/Industrial-Revolution`. Visited on: 15 Sept. 2021.

ERTL, G.; KNÖZINGER, H.; WEITKAMP, J. **Handbook of Heterogeneous Catalysis**. [S.l.: s.n.], Apr. 2008. P. 1–2497.

GASTON, B.; PROTTER, C. **Energy-Dispersive X-ray Spectroscopy (EDS)**. [S.l.: s.n.], 2022. Available from: `https://chem.libretexts.org/Courses/Franklin_and_Marshall_College/Introduction_to_Materials_Characterization__CHM_412_Collaborative_Text/Spectroscopy/Energy-Dispersive_X-ray_Spectroscopy_(EDS)#`. Visited on: 22 Oct. 2022.

GATES, S.M.; RUSSELL, J.N.; YATES, J.T. Bond activation sequence observed in the chemisorption and surface reaction of ethanol on Ni(111). **Surface Science**, v. 171, n. 1, p. 111–134, 1986. ISSN 0039-6028.

GHASEMZADEH, K.; JALILNEJAD, E.; SADATI TILEBON, S. M. Hydrogen Production Technologies From Ethanol. In: [s.l.: s.n.], Jan. 2019. P. 307–340. ISBN 9780128114582.

GOLUNSKI, S. E. John Ward Jenkins. **Platinum Metals Review**, v. 52, p. 249–250, Oct. 2008.

GRASCHINSKY, C.; GIUNTA, P.; AMADEO, N.; LABORDE, M. Thermodynamic analysis of hydrogen production by autothermal reforming of ethanol. **International Journal of Hydrogen Energy**, v. 37, p. 10118–10124, July 2012.

GRECZYNSKI, G.; HULTMAN, L. Reliable determination of chemical state in x-ray photoelectron spectroscopy based on sample-work-function referencing to adventitious carbon: Resolving the myth of apparent constant binding energy of the C 1s peak. **Applied Surface Science**, v. 451, p. 99–103, Sept. 2018.

GREY, L.; NIE, H-Y; BIESINGER, M. Defining the Nature of Adventitious Carbon and Improving Its Merit as a Charge Correction Reference for XPS. **Applied Surface Science**, v. 653, p. 159319, Apr. 2024.

GUTIERREZ, A.; KARINEN, R.; AIRAKSINEN, S.; KAILA, R.; KRAUSE, A. Autothermal reforming of ethanol on noble metal catalysts. **Fuel and Energy Abstracts**, v. 36, p. 8967–8977, July 2011.

HAO, P. et al. Surrounded catalysts prepared by ion-exchange inverse loading. **Science Advances**, v. 6, eaay7031, May 2020.

HARYANTO, A.; FERNANDO, S.; MURALI, N.; ADHIKARI, S. Current Status of Hydrogen Production Techniques by Steam Reforming of Ethanol: A Review. **Energy & Fuels - ENERG FUEL**, v. 19, July 2005.

HOLLEWAND, M.P.; GLADDEN, L.F. Probing the structure of porous pellets: An NMR study of drying. **Magnetic Resonance Imaging**, v. 12, p. 291–2947, 1994.

HOU, T.; ZHANG, S.; CHEN, Y.; WANG, D.; CAI, W. Hydrogen production from ethanol reforming: Catalysts and reaction mechanism. **Renewable and Sustainable Energy Reviews**, v. 44, Apr. 2015.

HUANG, Y. J.; XUE, J.J.; SCHWARZ, A. Analysis of temperature-programmed reduction profiles from metal-supported catalysts. **Journal of Catalysis**, v. 111, p. 59–66, May 1988.

JAN, G.; GAWĘDA, A.; WAŚKOWSKA, A. Encyclopedia of Geology, 2 nd Edition, (2021), Regional Geology Chapter Titles including Carpathians, p. 524, 525, 526, 527, 528, Feb. 2021.

JEHNG, J.-M.; CHEN, C.-M. Amination of Polyethylene Glycol to Polyetheramine over the Supported Nickel Catalysts. **Catalysis Letters**, v. 77, p. 147–154, Nov. 2001.

KHEMNARONG, P. HYDROGEN PRODUCTION VIA ETHANOL STEAM REFORMING OVER ALUMINA SUPPORTED RHENIUM-NICKEL CATALYST, 2021.

KOEL, B.; KIM, J. Promoters and Poisons. **Handbook of Heterogeneous Catalysis**, p. 1593–1624, Mar. 2008.

LE PAGE, J. F. **Applied Heterogeneous Catalysis: Design, Manufacture, and Use of Solid Catalysts**. [S.l.: s.n.], 1987. P. 531.

LEE, S.-Y.; ARIS, R. The Distribution of Active Ingredients in Supported Catalysts Prepared by Impregnation. **Catalysis Reviews-science and Engineering**, v. 27, p. 207–340, June 1985.

LEKHAL, A.; GLASSER, B.; KHINAST, J. Impact of Drying on the Catalyst Profile in Supported Impregnation Catalysts. **Chemical Engineering Science**, v. 56, p. 4473–4487, Aug. 2001.

LLORCA, J.; CORBERÁN, V. C.; DIVINS, N. J.; FRAILE, R. O.; TABOADA, E. Chapter 7. Hydrogen from Bioethanol. In: [s.l.: s.n.], June 2013. P. 135–169. ISBN 978-0-444-56352-1.

MAIA, T.; BELLIDO, J.; ASSAF, E.; ASSAF, J. Produção de hidrogênio a partir da reforma a vapor de etanol utilizando catalisadores Cu/Ni/gama-Al_2O_3. **Quimica Nova - QUIM NOVA**, v. 30, Apr. 2007.

MANFE, M.M.; KULKARNI, K.; KULKARNI, A.D. Industrial application of monolith catalysts/reactors. **International Journal of Advanced Engineering Research and Studies**, v. 1, p. 1–3, Jan. 2011.

MARCEAU, E.; CHE, M.; CEJKA, J.; ZUKAL, A. Nickel(II) Nitrate vs. Acetate: influence of the Precursor on the Structure and Reducibility of Ni/MCM-41 and Ni/Al-MCM-41 Catalysts. **ChemCatChem**, v. 2, p. 413–422, Mar. 2010.

MARIÑO, F.; BARONETTI, G.; JOBBAGY, M.; LABORDE, M. Cu-Ni-K/γ-Al_2O_3 supported catalysts for ethanol steam reforming: Formation of hydrotalcite-type compounds as a result of metal–support interaction. **Applied Catalysis A: General**, v. 238, n. 1, p. 41–54, 2003. ISSN 0926-860X.

MARIÑO, F.; BOVERI, M.; BARONETTI, G.; LABORDE, M. Hydrogen production from steam reforming of bioethanol using Cu/Ni/K/γ-Al_2O_3 catalysts. Effect of Ni. **International Journal of Hydrogen Energy**, v. 26, p. 665–668, July 2001.

MASCARENHAS, Y. Crystallography before the Discovery of X-Ray Diffraction. **Revista Brasileira de Ensino de Física**, v. 42, Jan. 2020.

MCMULLAN, D. Charles Oatley (1904–96). **Nature**, v. 380, p. 670, Apr. 1996.

MELLO DOS SANTOS, A.; SAGÁS, J.; PEREIRA, A.L.J.; ORIGO, F.D.; CATAPAN, R. C.; DUARTE, D.A. Ni/Al_2O_3 spherical catalysts produced by magnetron sputtering. **Vacuum**, v. 200, p. 111042, Mar. 2022.

MICROMERITICS. **Temperature-Programmed Reduction Using the AutoChem**. [S.l.: s.n.], 2022. Available from: `https://www.micromeritics.com/Repository/Files/appnote120.pdf`. Visited on: 14 Nov. 2022.

MITTASCH, A.; FRANKENBURG, W. Early Studies of Multicomponent Catalysts. In: FRANKENBURG, W.G.; KOMAREWSKY, V.I.; RIDEAL, E.K. (Eds.). [S.l.]: Academic Press, 1950. v. 2. (Advances in Catalysis). P. 81–104.

MOHALLEM, N.; VIANA, M.; SILVA, R. Automotive Catalysts: Performance, Characterization and Development. In: [s.l.: s.n.], Jan. 2011. ISBN 978-953-307-999-8.

MOULDER, J. F. Handbook of X-ray photoelectron spectroscopy: a reference book of standard spectra for identification and interpretation of XPS Data, p. 254, 1992.

MOZER, T. S. **Estudo da adição do promotor Cu aos catalisadores Pt/Al_2O_3 e Pt/Nb_2O_5 para a oxidação seletiva de CO**. 2005. S. 96. Mestrado em Química – Universidade Federal Fluminense, Niterói.

NAHAR, G.; DUPONT, V. Hydrogen production from simple alkanes and oxygenated hydrocarbons over ceria–zirconia supported catalysts: Review. **Renewable and Sustainable Energy Reviews**, v. 32, p. 777–796, Apr. 2014.

NASROLLAHZADEH, M.; ATAROD, M.; SAJJADI, M.; SAJADI, S. M.; ISSAABADI, Z. Plant-Mediated Green Synthesis of Nanostructures: Mechanisms, Characterization, and Applications. In: [s.l.: s.n.], Jan. 2019. P. 199–322. ISBN 9780128135860.

NATIONS, United. **United Nations Conference on the Human Environment, 5-16 June 1972, Stockholm**. [S.l.: s.n.], 2021. Available from: `https://www.un.org/en/conferences/environment/stockholm1972`. Visited on: 15 Sept. 2021.

NEWBURY, D. Mistakes Encountered During Automatic Peak Identification of Minor and Trace Constituents in Electron-Excited Energy Dispersive X-Ray Microanalysis. **Scanning**, v. 31, p. 91–101, May 2009.

NIETO-MÁRQUEZ, A.; SÁNCHEZ, D.; MIRANDA-DAHDAL, A.; DORADO, F.; LUCAS-CONSUEGRA, A.; VALVERDE, J. Autothermal reforming and water–gas shift double bed reactor for H2 production from ethanol. **Chemical Engineering and Processing: Process Intensification**, v. 74, p. 14–18, Dec. 2013.

NIK ZAIMAN, N. F. H.; SHAARI, N. Review on flower-like structure nickel based catalyst in fuel cell application. **Journal of Industrial and Engineering Chemistry**, v. 119, p. 1–76, 2023. ISSN 1226-086X.

NIKOLAIDIS, P.; POULLIKKAS, A. A comparative overview of hydrogen production processes. **Renewable and Sustainable Energy Reviews**, v. 67, p. 597–611, Jan. 2017.

OGO, S.; SEKINE, Y. Recent progress in ethanol steam reforming using non-noble transition metal catalysts: A review. **Fuel Processing Technology**, v. 199, p. 106238, Mar. 2020.

OURWORLDINDATA.ORG. **Per capita CO_2 emissions**. [S.l.: s.n.], 2022. Available from: https://ourworldindata.org/grapher/co-emissions-per-capita?tab=chart&country=BRA~OWID_WRL. Visited on: 22 Mar. 2024.

PALM, M. O. **PRODUÇÃO E CARACTERIZAÇÃO DE MONOLITOS CATALÍTICOS PARA REAÇÃO DE REFORMA A VAPOR E OXIDAÇÃO PARCIAL DE ETANOL**. 2018. S. 105. Mestrado em Engenharia e Ciências Mecânicas – Universidade Federal de Santa Catarina, Joinville.

PEREGO, C.; VILLA, P. Catalyst preparation methods. **Catalysis Today**, v. 34, p. 281–305, Feb. 1997.

PICONI, C. Comprehensive Biomaterials. In: [s.l.: s.n.], 2011. P. 73–94. ISBN 978-0-08-055294-1.

PINNA, F. Supported metal catalysts preparation. **Catalysis Today**, v. 41, p. 129–137, May 1998.

POMPEO, F.; NICHIO, N. N.; SOUZA, M. M.V.M.; CESAR, D. V.; FERRETTI, O. A.; SCHMAL, M. Study of Ni and Pt catalysts supported on α-Al_2O_3 and ZrO_2 applied in methane reforming with CO_2. **Applied Catalysis A: General**, v. 316, n. 2, p. 175–183, 2007. ISSN 0926-860X.

POTT, C. M.; ESTRELA, C. C. Histórico ambiental: Desastres ambientais e o despertar de um novo pensamento. **Estudos Avançados**, v. 31, p. 271–283, May 2017.

RABENSTEIN, G.; HACKER, V. Hydrogen for Fuel Cells From Ethanol by Steam-Reforming, Partial-Oxidation and Combined Auto-Thermal Reforming: A Thermodynamic Analysis. **Journal of Power Sources**, v. 185, p. 1293–1304, Dec. 2008.

RAMADE, A.; DELATORRE, R.; DUARTE, D. A. Effect of the Oxidation of Al Substrates on Properties of TiO2 Films Deposited by Spin Coating. **Brazilian Journal of Physics**, v. 54, Dec. 2023.

RASKÓ, J.; HANCZ, A.; ERDŐHELYI, A. Surface species and gas phase products in steam reforming of ethanol on TiO_2 and Rh/TiO_2. **Applied Catalysis A: General**, v. 269, p. 13–25, Aug. 2004.

REN-YUAM, T.; RONG-AN, W.; LI-WU, L. Evidence of strong metal-support interaction in alumina-supported platinum catalysts. **Applied Catalysis**, v. 10, n. 2, p. 163–172, 1984. ISSN 0166-9834.

RIBEIRO, E.; FRANCISCO, M.; GUSHIKEM, Y.; GONÇALVES, J. Princípios básicos de XAS e XPS. **Revista Chemkeys**, p. 1–23, Sept. 2018.

RODRIGUES, C. P.; SCHMAL, M. Nickel–alumina washcoating on monoliths for the partial oxidation of ethanol to hydrogen production. **International Journal of Hydrogen Energy**, v. 36, p. 10709–10718, Aug. 2011.

SAKATA, Y.; TAMAURA, Y.; IMAMURA, H.; WATANABE, M. Preparation of a New Type of $CaSiO_3$ with High Surface Area and Property as a Catalyst Support. **Studies in Surface Science and Catalysis**, v. 162, p. 331–338, Dec. 2006.

SATTERFIELD, C. N. **Heterogeneous Catalysis in Industrial Practice**. [S.l.: s.n.], 1980. P. 554.

SCHMAL, M. **Catálise Heterogênea**. [S.l.]: 1ª Edição. Rio de Janeiro: Synergia, 2011. P. 358. ISBN 978-8561325534.

SCHUMANN, J.; EICHELBAUM, M.; LUNKENBEIN, T.; THOMAS, N.; ÁLVAREZ GALVÁN, M. C.; SCHLÖGL, R.; BEHRENS, M. Promoting Strong Metal Support Interaction: Doping ZnO for Enhanced Activity of Cu/ZnO:M (M = Al, Ga, Mg) Catalysts. **ACS Catalysis**, v. 5, n. 6, p. 3260–3270, 2015.

SCIENCE, Office of. **DOE Explains Catalysts**. [S.l.: s.n.]. Available from: `https://www.energy.gov/science/doe-explainscatalysts`. Visited on: 30 Aug. 2022.

SCUDIERO, L. **Physical Chemistry laboratory and Materials Science & Engineering**. [S.l.: s.n.], 2006. Available from: `https://public.wsu.edu/~pchemlab/index.html`. Visited on: 4 July 2022.

SEO, J.; YOUN, M.; CHUNG, J. S.; SONG, I. Effect of calcination temperature of mesoporous nickel–alumina catalysts on their catalytic performance in hydrogen production by steam reforming of liquefied natural gas (LNG). **Journal of Industrial and Engineering Chemistry**, v. 16, p. 795–799, Sept. 2010.

SHIRLEY, D. A. High-Resolution X-Ray Photoemission Spectrum of the Valence Bands of Gold. **Phys. Rev. B**, American Physical Society, v. 5, p. 4709–4714, 12 June 1972.

SILVA JÚNIOR, M. E.; PALM, M. O.; DUARTE, D. A.; CATAPAN, R. C. Catalytic Pt/Al_2O_3 Monolithic Foam for Ethanol Reforming Fabricated by the Competitive Impregnation Method. **ACS Omega**, v. 8, Feb. 2023.

SINGHAL, S.C.; KENDALL, K. **High-temperature Solid Oxide Fuel Cells: Fundamentals, Design and Applications**. [S.l.: s.n.], Jan. 2003. P. 1–405.

SOARES, L.; BRITO, C.; MAIA, C.; SODRE, J. OVERVIEW OF THE ETHANOL STEAM REFORMING FOR HYDROGEN PRODUCTION. In.

SUN, H.; ZELEKEW, O. A.; CHEN, X.; GUO, Y.; KUO, D.-H.; LU, Q.; LIN, J. A noble bimetal oxysulfide Cu V OS catalyst for highly efficient catalytic reduction of 4-nitrophenol and organic dyes. **RSC Advances**, v. 9, p. 31828–31839, Oct. 2019.

THOMAS, J. M. The birth of X-ray crystallography. **Nature**, v. 491, p. 186–187, Nov. 2012.

TOMAŠIC, V.; JOVIC, F. State-of-the-art in the monolithic catalysts/reactors. **Applied Catalysis A: General**, v. 311, p. 112–121, Sept. 2006.

TORRE-ABREU, C.; RIBEIRO, M. F.; HENRIQUES, C.; DELAHAY, G. NO TPD and H2-TPR studies for characterisation of CuMOR catalysts The role of Si/Al ratio, copper content and cocation. **Applied Catalysis B: Environmental**, v. 14, p. 261–272, Dec. 1997.

TRANSPORTATION, The international council of clean. **A new life-cycle assessment of the greenhouse gas emissions of combustion engine and electric passenger cars in major markets**. [S.l.: s.n.], 2021. Available from: `https://theicct.org/wp-content/uploads/2022/01/Global-LCA-passenger-cars-FS-EN-jul2021.pdf`. Visited on: 29 Aug. 2022.

TUSAR, N.; KAUCIC, V.; LOGAR, N. Z. Functionalized Porous Silicates as Catalysts for Water and Air Purification. **New and Future Developments in Catalysis: Hybrid Materials, Composites, and Organocatalysts**, p. 365–383, July 2013.

VASSEUR, E. United Nations Conference on the Human EnvironmentStockholm, 5–16 June 1972. **Water Research - WATER RES**, v. 7, p. 1227–1233, Aug. 1973.

VIDAL, J. **Projeto, desenvolvimento e validação de um reator para reforma auto térmica de etanol**. 2023. S. 122. Mestrado em Engenharia e Ciências Mecânicas – Universidade Federal de Santa Catarina, Joinville.

VITA, A.; PINO, L.; ITALIANO, C.; PALELLA, A. Steam Reforming, Partial Oxidation, and Autothermal Reforming of Ethanol for Hydrogen Production in Conventional Reactors, p. 159–191, Jan. 2019.

VIZCAÍNO, A.; ARENA, P.; BARONETTI, G.; CARRERO, A.; CALLES, J.; LABORDE, M.A.; AMADEO, N. Ethanol steam reforming on Ni/Al_2O_3 catalysts: Effect of Mg addition. **International Journal of Hydrogen Energy**, v. 33, p. 3489–3492, July 2008.

WAGNER, C. D.; DAVIS, L. E.; ZELLER, M. V.; TAYLOR, J. A.; RAYMOND, R. H.; GALE, L. H. Empirical atomic sensitivity factors for quantitative analysis by electron spectroscopy for chemical analysis, Surface and Interface Analysis, p. 211–225, 1982.

WAGNER, C. D.; RIGGS, W. M.; DAVIS, L. E.; MOULDER, J. F.; MUILENBERG, G. E. Handbook of X-ray photoelectron spectroscopy: a reference book of standard spectra for use in X-ray photoelectron spectroscopy. **Perkin-Elmer Corporation, Eden Prairie**, p. 190, 1979.

WANG, W.; ZHAO, S.; TANG, X.; CHEN, C.; YI, H. Stainless steel catalyst for air pollution control: structure, properties, and activity. **Environmental Science and Pollution Research**, v. 29, p. 1–33, Aug. 2022.

YAMAMOTO, O. Solid Oxide Fuel Cells: Fundamental Aspects and Prospects. **Electrochimica Acta**, v. 45, p. 2423–2435, May 2000.

YANG, X.; CHEN, Z.; GONG, H. Coking of Pt/γ-Al_2O_3 catalyst in landfill gas deoxygen and its effects on catalytic performance. **Chinese Journal of Chemical Engineering**, v. 57, p. 224–232, 2023. ISSN 1004-9541.

YOUN, M. H.; SEO, J. G.; KIM, P.; KIM, J. J.; LEE, H.-I.; SONG, I. K. Hydrogen production by auto-thermal reforming of ethanol over Ni/γ-Al_2O_3 catalysts: Effect of second metal addition. **Journal of Power Sources**, v. 162, n. 2, p. 1270–1274, 2006. Special issue including selected papers from the International Power Sources Symposium 2005 together with regular papers. ISSN 0378-7753.

ZANCHET, D.; SANTOS, J.; DAMYANOVA, S.; GALLO, J. M.; BUENO, J.M.C. Toward Understanding Metal-Catalyzed Ethanol Reforming. **ACS Catalysis**, v. 5, p. 150415131002003, Apr. 2015.

APPENDIX A – INJECTOR NOZZLE

The injector nozzle is a vital component in fuel injection systems used in engines. Its precisely and controllably spray fuel directly into the engine, ensuring efficient combustion, with direct impacts on engine performance, fuel economy, and pollutant emission reduction. In this study, the injector nozzle was from a MHX Honda Biz 125 motorcycle with 6 holes, used to spray the water/ethanol mixture into the reactor.

The calibration of the injector nozzle flow rate was conducted using the gravimetric analysis. This method employs a scale to measure the mass of the fluid released by the nozzle in a specific period. The water/ethanol mixture tank was pressurized at 3 bar. The molar ratio of the water/ethanol mixture used was 3:1. The calibration involved setting the operating frequency at 16 Hz and varying the Duty Cycle, representing the proportion in which the injector nozzle remains open for fuel release, ranging from 0% to 100%. The injector nozzle was positioned over a beaker placed on the precision balance, which was zeroed before starting the calibration.

Three tests were conducted for each Duty Cycle value, and the average values were used. The amount of mixture discharged was weighed after 1 min of operation. The data obtained from the tests and the average values for each duty cycle were calculated, as shown in Table A.1. A linear regression analysis in Python was conducted to create the linear function: y(x) = 0.418x - 0.544, which describes the mass flow rate as a function of the duty cycle, as shown in Figure A.1.

Figure A.1 – Injector nozzle calibration.

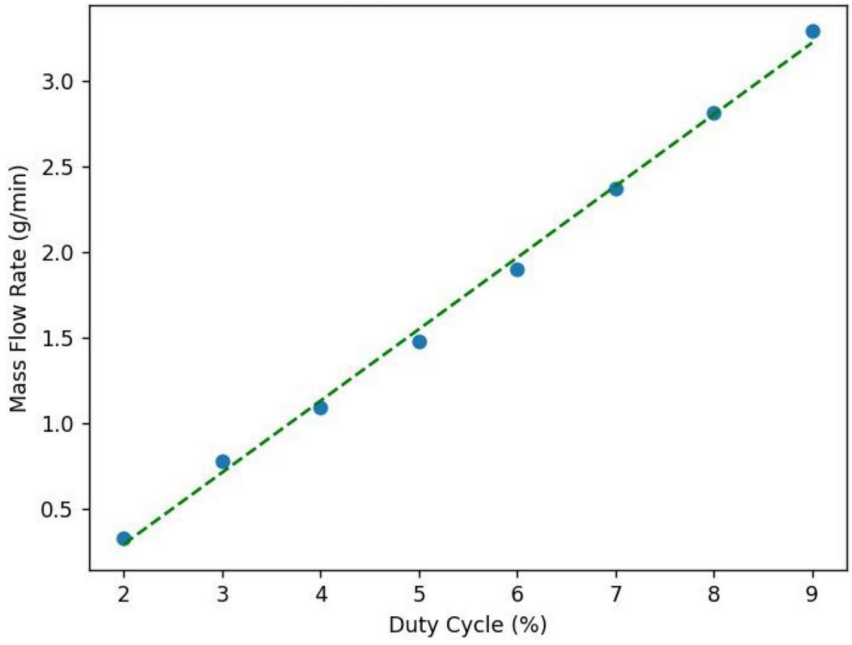

Source: Developed by the author (2023).

Table A.1 – Experimentally measured values.

Duty Cycle (%)	**Mass Flow Rate (g/min)**	**Average (g/min)**
	0.33	
2	0.33	0.33
	0.32	
	0.77	
3	0.78	0.78
	0.78	
	1.07	
4	1.10	1.09
	1.09	
	1.47	
5	1.49	1.48
	1.48	
	1.90	
6	1.88	1.89
	1.90	
	2.37	
7	2.38	2.37
	2.36	
	2.81	
8	2.82	2.81
	2.81	
	3.29	
9	3.30	3.29
	3.27	

Source: Developed by the author (2023).